EVALUATION OF THE PERFORMANCE OF BRIDGE STEEL PEDESTALS UNDER LOW SEISMIC LOADS

A Dissertation
Presented to
The Academic Faculty

by

Monique C. Hite

In Partial Fulfillment
of the Requirements for the Degree
Doctor of Philosophy in the
School of Civil and Environmental Engineering

Georgia Institute of Technology
May 2007

EVALUATION OF THE PERFORMANCE OF BRIDGE STEEL PEDESTALS UNDER LOW SEISMIC LOADS

Approved by:

Dr. Reginald DesRoches, Co-advisor
School of Civil and Environmental Engineering
Georgia Institute of Technology

Dr. Roberto T. Leon, Co-advisor
School of Civil and Environmental Engineering
Georgia Institute of Technology

Dr. Laurence Jacobs
School of Civil and Environmental Engineering
Georgia Institute of Technology

Dr. Lawrence Kahn
School of Civil and Environmental Engineering
Georgia Institute of Technology

Dr. Glenn Rix
School of Civil and Environmental Engineering
Georgia Institute of Technology

Dr. Leland T. Long
Earth and Atmospheric Sciences
Georgia Institute of Technology

Date Approved: March 29, 2007

I dedicate this work to the late Frances L. Simms, my maternal grandmother who embodied the principles of hard work, determination, perseverance, fortitude, patience, wisdom and love for which she demonstrated and shared with others so graciously. She was one of my cherished role models and, moreover, an inspiration for life.

ACKNOWLEDGMENTS

I would like to thank my parents, Mary and Monroe C. Hite, Jr., my brother, Monroe III, and sister-in-law, Kertrina, my nephew and godson, Monroe C. Hite, IV, friends, paternal grandmother, Mabel L. Hite, extended family in Virginia, and the Black Graduate Student Association (BGSA) for all of their support and words of encouragement throughout this journey. Special thanks and heartfelt love to my boyfriend, Kristopher P. Head, who has always believed in me and challenges me to be the best in all that I do - CARPE DIEM!

I would also like to thank the following who have been extremely supportive throughout my doctoral studies at the Georgia Institute of Technology: Dr. Reginald DesRoches, Dr. Roberto T. Leon, Dr. Laurence Jacobs, my committee, my office mates in Mason 325, all of my colleagues in the Mason Building with whom I have interacted, Mrs. Lillie Brantley, and Mr. Roosevelt King. Dr. DesRoches and Dr. Leon have been instrumental as not just my co-advisors but also mentors. I appreciate their continuous support and for shaping me into the researcher that I am today.

During my doctoral research experience, I spent a lot of time in the Structures Laboratory to conduct the large-scale testing for which I received much guidance from the laboratory coordinator at the time, Mr. Mahmoud Azari. Special thanks to the undergraduates that helped with the experimental setup and testing: Kennan Crane, Reese Williams, Brian Hill, Matthew Smith, and Jason Crouse. Last but not least, I thank God for whom all this was made possible. I am thankful for my many blessings, especially the ones throughout my dissertation journey and my future (Jeremiah 29:11).

TABLE OF CONTENTS

LIST OF TABLES

LIST OF FIGURES

LIST OF SYMBOLS AND ABBREVIATIONS

°	deg, degrees (temperature measurement)
"	inches (length measurement)
'	feet (length measurement)
Δ	displacement (absolute or relative)
K_{eff}	effective (secant) stiffness from hysteretic relations
E_D	energy dissipation (absorption)
ζ_{eq}	equivalent viscous damping
μ_Δ	displacement ductility ratio
θ	angle of rotation
ω_n	natural frequency of vibration
T_n	natural period of vibration
GDOT	Georgia Department of Transportation
MTS	MTS (actuator manufacturer)
3DOF	three-degree-of-freedom
NTHA	nonlinear time history analysis/analyses
SHA	seismic hazard analysis/analyses
UHRS	uniform hazard response spectrum/spectra

SUMMARY

Full-scale, quasi-static, reversed cyclic tests of a two-girder 40' bridge specimen rehabilitated with steel pedestals are conducted to characterize the behavior, assess the deformation and strength capacity, and experimentally evaluate any vulnerabilities of 19" and 33½" steel pedestals used by the Georgia Department of Transportation (GDOT). The six tests show varying deformation (1.75" to 3.5") and strength capacity (25.8 kips to 96.4 kips) of the pedestals for two loading directions (strong- and weak-axis) and two configurations for the placement of the anchor bolts. Tests from this study reveal the pedestals to be elastic, flexible components, where peak displacements reached were limited by a deformation mode rather than permanent deformation or instability of the pedestals themselves. The three modes of deformation observed are prying-action, bolts yielding, and concrete breakout. Prying-action of the anchor bolts embedded in the reinforced concrete bent cap is the predominant mode as the anchor bolts pullout from the concrete with increased cycling due to sliding (anchor bolts subjected to shear loading) and rocking of the pedestals (anchor bolts subjected to tensile loads). The force-displacement relationships capture the hysteretic behavior of the pedestals and indicate rigid body kinematics (sliding and rocking) of the system. From all six hysteresis loops, 7-17% of energy is dissipated through equivalent viscous damping of the pedestals, which is a necessary characteristic for the seismic performance of connection elements during an earthquake. The displacement ductility ratio, μ, ranges from 2.8 to 13 for all six tests, where ductility ratios from 4 to 6 may be expected in extreme seismic events. From the force-displacement hysteretic relationships, other response parameters such as

the effective stiffness and equivalent viscous damping of the pedestals are computed and compared. The force-displacement hysteretic relationships, in turn, are used to calibrate an analytical bridge model to determine the displacement demands.

A GDOT candidate bridge with steel pedestals is idealized as a 3DOF system to determine the bridge displacement demands using two approaches:

(1) by calculating the peak displacement from accelerations generated by uniform hazard spectra based on USGS (2002) maps for the range of structural periods from all six tests represented by the 3DOF system, and

(2) by calculating the peak displacements from response spectra generated from a suite of site-specific synthetic ground motions developed by Fernandez and Rix (2006).

For this simple 3DOF model of a candidate bridge in Georgia, the inelastic behavior defined for the pedestals shows satisfactory performance for low seismic loads where the deformation and strength capacity are adequate as long as a mode of deformation leading to a mechanism of failure does not occur. Best practices, design guidelines, and inspection and maintenance advice are recommended to GDOT based on this study.

CHAPTER 1

INTRODUCTION

1.1 Problem Description

A number of bridges are damaged every year by accidental collisions from over-height vehicles, resulting in significant direct and indirect costs to redesign, repair and reroute traffic (Mang and Bucak 1993; Fu, Burhouse et al. 2004; Qiao, Yang et al. 2004; El-Tawil, Severino et al. 2005). With the trucking industry's push for larger trucks to transport goods throughout the country, these vehicles will exceed the vertical clearance height of many bridges in the transportation network. To address the need to limit collisions from over-height trucks, many states have developed programs to screen bridges for insufficient vertical clearance and raise them to reduce the likelihood of impact from over-height vehicles.

The Georgia Department of Transportation (GDOT) has begun to address the issue of limited vertical clearance heights by elevating bridges with steel pedestals. In Georgia, more than 50 bridges over major arterials have been retrofitted in this manner. These pedestals, in the form of very short steel columns, act as height boosters that transfer loads from the bridge deck to the columns and substructure. The process to install the pedestals is cost-effective and uses well-understood technologies to jack the bridges and install the steel pedestals.

In practice, these pedestals are not detailed to provide end fixity, so they add considerable flexibility to the superstructure supports. Although steel pedestals increase the vertical clearance height of bridges thereby reducing the likelihood of impact damage,

they make the bridges more susceptible to instability and damage from lateral loads such as those produced by small and moderate earthquakes (Ye, Hu et al. 2001; DesRoches, Pfeifer et al. 2003). Given existing structural deficiencies of many bridges, there is concern as to how the steel pedestals will behave and affect the bridge response when subjected to low-to-moderate level seismic loads. Therefore, research is needed to provide a better understanding of the seismic performance of steel pedestals in Georgia and other states that are considering the use of steel pedestals as a cost-effective and safe means to elevate bridges.

1.2 Research Objectives and Plan of Study

The objective of this research is to evaluate the performance of steel pedestals under low-to-moderate seismic loads by:

1. experimentally testing short and moderately slender steel pedestals typically used to elevate bridges in Georgia to assess the changes in stiffness and resistance from the addition of these elements
2. utilizing the experimental results to evaluate analytically the displacement demands of the steel pedestals in a one-dimensional, three-degree-of-freedom (3DOF) bridge model developed in OpenSees subjected to synthetic ground motions expected in the CSUS
3. synthesizing the experimental and analytical results into design recommendations to the Georgia Department of Transportation (GDOT) on the best practices for steel pedestals.

To accomplish these objectives, a coupled experimental and analytical investigation is undertaken as shown in the research plan (Figure 1.1). Full-scale quasi-static reversed cyclic tests are performed on a two-girder 40' bridge specimen with steel pedestals installed based on typical field procedures by GDOT. A major testing goal is to determine any vulnerability of the steel pedestals related to connection detailing, strength deterioration, deformation capacity, and structural instability due to horizontal inertial loads. The stiffness characteristics of the steel pedestals obtained from the experimental force-displacement hysteretic relationships are utilized in a simplified analytical 2D OpenSees model to determine the displacement demands using synthetic ground motions for nonlinear time history analyses. As a result, the findings and recommendations for the evaluation of the performance and best practices of steel pedestals subjected to low-to-moderate seismic loads are presented. The broader impact of this study will be the development of a methodology that can be used in the analysis of steel pedestals for other states besides Georgia and for other unstable supports such as high type rocker bearings.

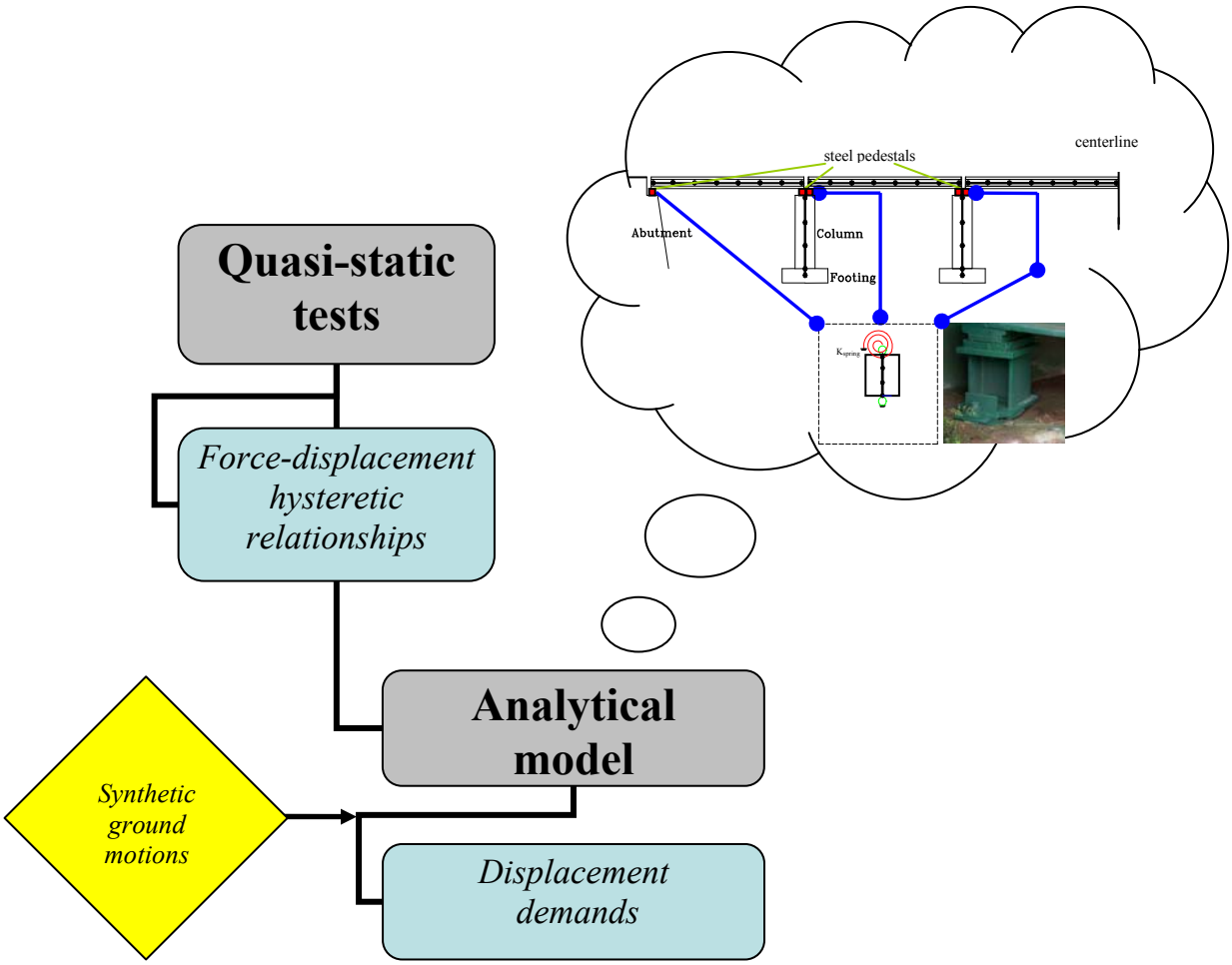

Figure 1.1: Research Approach

1.3 Dissertation Outline

This dissertation is organized into seven chapters with the following contents:

Chapter 2 motivates a need for elevating bridges to reduce the likelihood of damage from over-height vehicles. Elevation procedures adopted by GDOT and other states in the Central and Southeastern United States (CSUS) are discussed. An overview of the seismic performance of bridges and bridge bearings is provided, where steel pedestals used to elevate bridges in Georgia may affect the dynamic characteristics and consequently the bridge response similar to the performance of bridge bearings in past earthquakes.

Chapter 3 summarizes the experimental test setup used in this research project to evaluate the performance of bridge steel pedestals.

Chapter 4 presents the summary of the results from experimental testing. Complete details of the test results are provided in the Appendices.

Chapter 5 describes the detailed analytical modeling that incorporates the force-displacement hysteretic relationships obtained from the experimental test results to define the behavior of the pedestals. Results from the analytical study are used to determine the displacement demands for a candidate bridge modeled in OpenSees.

Chapter 6 shows the recommendations for the best practices and design guidelines for the design, construction, and retrofit of bridges rehabilitated with steel pedestals.

Finally, in **Chapter 7**, the conclusions for the performance of steel pedestals are presented and future research needs are identified.

Appendix A and **Appendix B** show more details of the experimental test results and the development of the synthetic ground motions used for the nonlinear time history analyses (NTHA), respectively.

CHAPTER 2

LITERATURE REVIEW

2.1 Impact Loads on Bridges

Bridge damage due to impact loads from over-height vehicle collisions is a major issue occurring throughout the transportation network (Fu, Burhouse et al. 2004; El-Tawil, Severino et al. 2005). Due to the lack of a nationwide database of over-height vehicle collisions, Fu, Burhouse, et al. (2004) conducted a national survey to collect data on the number of incidences due to over-height vehicle collisions. From the responses, 62% (18 of 29) of the states that responded to the survey reported over-height vehicle collisions to be a significant problem. The data revealed an 81% increase in over-height vehicle collisions between 1995 and 2000 in the state of Maryland.

Damage from impact loads can range from minor distortion or spalling in fascia girders to almost complete bridge destruction. In either case, there are high costs associated with bridge repair, rerouting traffic, and indirect economic and societal costs. Common limited damage to fascia girders is shown in Figure 2.1 for the case of a portion of a piece of construction equipment striking a bridge on an interstate in south Atlanta, Georgia. In this case, the girder had to be replaced at considerable cost but without having to reroute traffic except for limited periods during weekend nights. As an illustrative example of larger damage, consider the case of an over-sized load traveling from Oklahoma to a refinery in Illinois that was granted access to I-44 per a permit from the Missouri Department of Transportation (MoDOT). By mistake, the driver entered I-44 one exit too early, and was too tall for the 15 foot clearance. At 35 miles per hour, the

oil tanker struck the bottom chord at an estimated speed of 35 miles per hour. The impact resulted in a total lateral deformation of the steel beams of approximately 7 feet (Figure 2.2). The truck was cut free after MoDOT crews worked several hours with cutting torches to remove the tank. The interstate traffic had to be rerouted via ramps around the bridge. The total damage was estimated to be about $4.5 million to demolish and replace the bridge and caused traffic delays due to reconstruction for 299 days (Decker 2001). Similar damage to a concrete bridge is shown in Figure 2.3 for the case of a backhoe whose working arm became loose accidentally during transportation, which is a contrast to the damage shown in Figure 2.1.

Clearly, impact loads mainly posed by over-height vehicle collisions will continue to be a problem given the large number of bridges in the interstate highway system at the limit of the required federal vertical clearance of 16 feet. The Georgia Department of Transportation (GDOT) has begun to address the problem by implementing a statewide program to elevate more than 50 bridges with steel pedestals to reduce the likelihood of impact damage. Review of GDOT's current practice for elevating bridges with steel pedestals is presented in the next section, while elevation tactics for bridges in neighboring and other states in the CSUS are presented in *Section 2.3*.

Figure 2.1: Damage to fascia girder of a bridge in south Atlanta, Georgia

Figure 2.2: MoDOT I-44 bridge impacted by oil tanker in Lebanon, Missouri

2.2 GDOT Review of Current Practice for Elevating Bridges with Steel Pedestals

The Georgia Department of Transportation (GDOT), which sponsored this study, raises bridges to increase the vertical clearance height by installing steel pedestals. For GDOT's standards, typically the contractor is to provide a minimum vertical clearance of 16'-9" over the travel way and paved shoulders. The steel pedestals are basically short steel columns consisting of W-shapes with 1" top and bottom steel plates. These columns are connected to the bridge superstructure (generally a steel rolled beam or plate girder) by two anchor bolts, and to the substructure via embedded anchor bolts aligned within a pair of L-shaped angles. The angles are welded to the base plate of the pedestals, and a ⅛" elastomeric pad is placed under the pedestal for better bearing and increased flexibility in shear capacity as shown in Figure 2.3 (Georgia Department of Transportation).

In this research, the plans for the installation of pedestals on GDOT Bridge No. 72, located in Liberty County, Georgia, were taken as typical of this type of project. The details for the construction sequence are noted as follows:

1. Remove guardrail and place temporary barrier at all four corners of bridge.
2. Raise tops of wingwalls.
3. Cut approach slab full depth at the edge of paving. Rest and remove endwall concrete as required to allow jacking of bridge.
4. Remove portion of endwall between exterior beam and wingwall as to provide access to bearings and allow drilling of new anchor bolt holes.
5. Jack bridge without disrupting traffic. Install pedestals. Place asphalt as required at ends of bridge while jacking to provide a smooth transition

from pavement to bridge.

6. After jacking is complete, extend the endwalls.
7. Remove the temporary barrier at each corner of the bridge and replace the guardrail.
8. Reduce traffic to one lane.
9. Construct portion of new approach slab.
10. Clean and reseal transverse construction and expansion joints and clean and reseal joints with low-density, closed cell, polyethylene seals.
11. Remove existing joint and edge beams and reconstruct. Replace joints with low-density, closed cell, polyethylene seals.
12. Shift traffic to opposite side and repeat steps 9 through 11.
13. Remove temporary barrier and re-open bridge to two lanes of traffic.
14. Clean and paint existing structural steel.

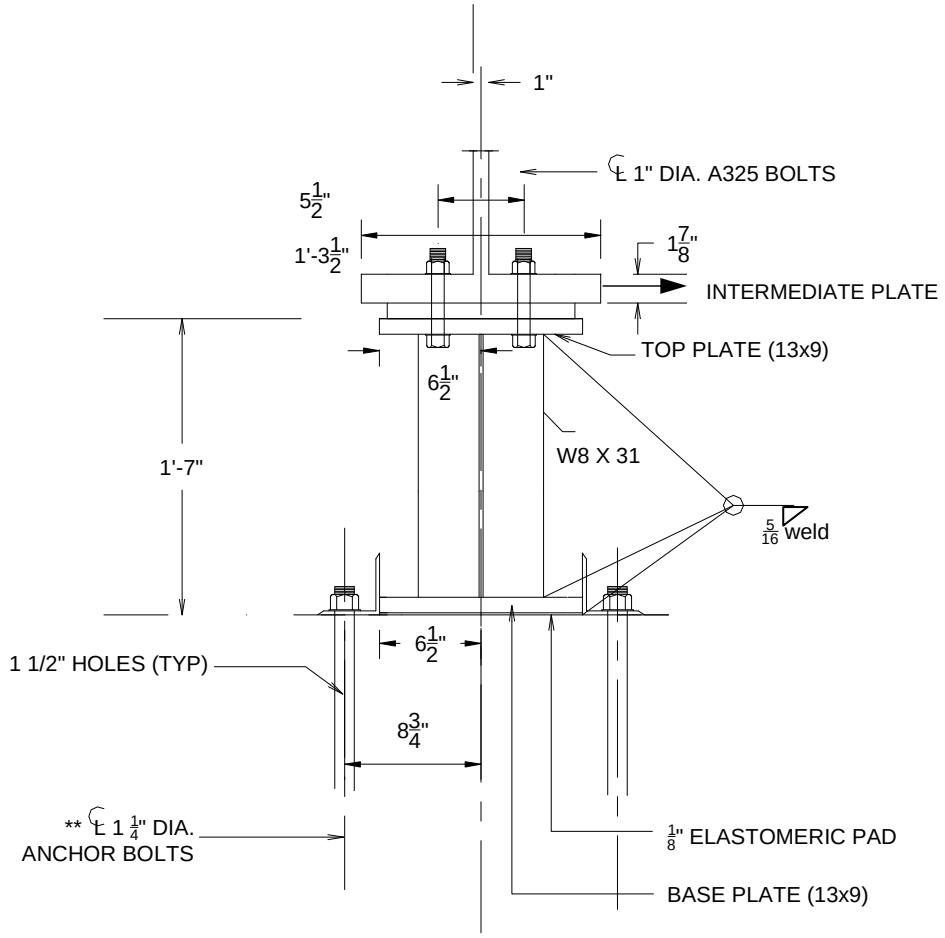

Figure 2.3: Design of steel pedestal (Georgia DOT)

2.3 Elevation Procedures for Bridges in the CSUS

Other procedures besides the use of steel pedestals are used in the CSUS to elevate bridges. While the elevation procedures for bridges in the CSUS are different, the process for elevating bridges is not a new concept. Almost 70 years ago, the Jhelum railway bridge, one of the longest in India at that time, was raised due to rising water levels of the Jhelum River (McIntyre 1937). Jacking operations were used to lift the spans off the bearings, one pier at a time. To adjust for the elevation differences, newly cast steel bottom bearings were placed under the outer girders to keep the steel grillages, or I-beams, level. Following that, the steel grillages were encased with concrete. Both the grillages and bearings were used to raise the bridge, where the bearings transfer loads in a similar manner to how steel pedestals transfer load from the superstructure to the substructure. To reduce the likelihood of collisions from over-height vehicles, other states besides Georgia within the CSUS use a variety of methods to elevate bridges in Mississippi, Indiana, Illinois, and Missouri.

The Mississippi State Highway Department uses steel pedestals similar to those used by the Georgia Department of Transportation (GDOT). Figure 2.4 shows the pedestal bearing assembly of a 4-span prestressed concrete bridge system with existing expansion and fixed bearings. The total length of the bridge is 262'-3". Galvanized swedged anchor bolts are used along with the existing rocker and bearing plates. The bid price for raising this 4-span bridge was $95,000 in 1993 (Berry 2004). As additional preventive measures, the Mississippi State Highway Department also has an over-height warning system to alert over-height vehicles before approaching a bridge (Hanchey and Exley 1990). For some critical structures such as railroad bridges, the Japanese use large

tubes suspended from (rigid) frames or (rigid) frames before approaching a bridge bypass to prevent collisions by over-height vehicles (Figure 2.5).

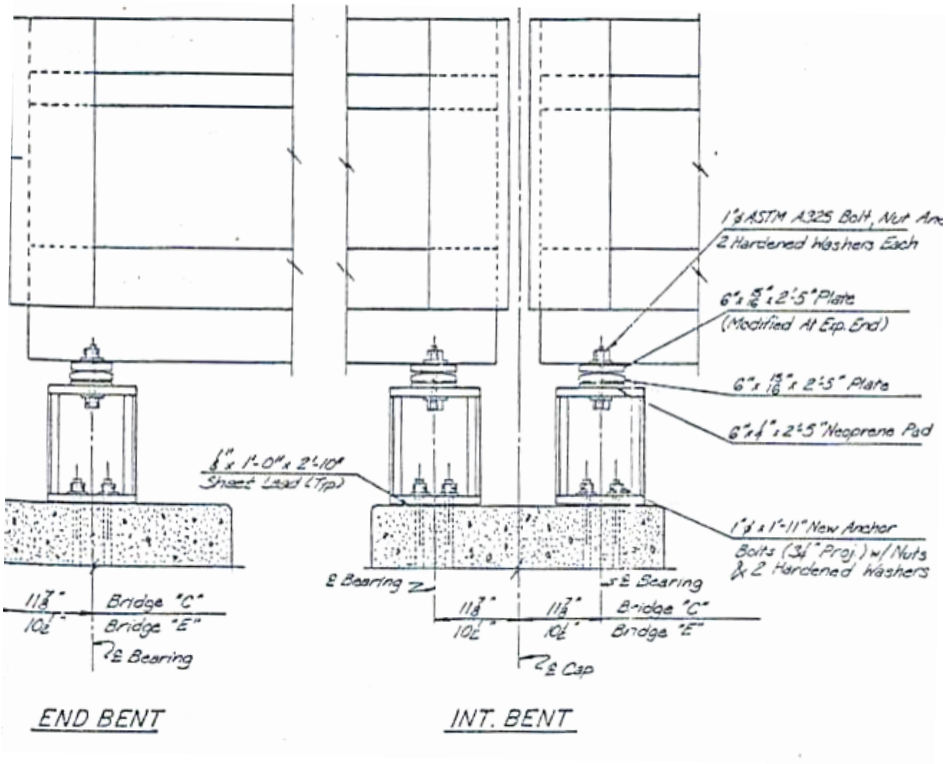

Figure 2.4: Pedestal bearing assembly of a 4-span prestressed concrete bridge (Mississippi State Highway Department)

Figure 2.5: Large (rigid) frames to prevent bypass and potential collisions of over-height vehicles in Japan

The Indiana Department of Transportation (InDOT) has used bearing assemblies similar to steel pedestals used in Georgia to increase the vertical clearance height of a couple of bridges in Indiana. The bearing assembly shown in Figure 2.6 is for a bridge located in Marion County, Indiana. The bearing assembly consists of a 10 x 14 x 2 ¼ A36 steel plate with ⅞" bolts that are drilled and tapped, six inches of steel plates with a thickness of 3/32 and two 1" diameter L-shaped threaded steel rods for which a side retainer is attached. The InDOTs construction procedure to install the bearing assemblies is as follows (Snyder 2005):

1. Close structure to traffic.
2. Install jacks and all equipment necessary to raise structure.
3. Raise structure while maintaining equal jacking height at each support (±1").
4. Construct bearing pedestals.
5. Install new bearing pads.
6. Install fixed shoes.
7. Construct approach items.
8. Install new joint seals.
9. Open to traffic.

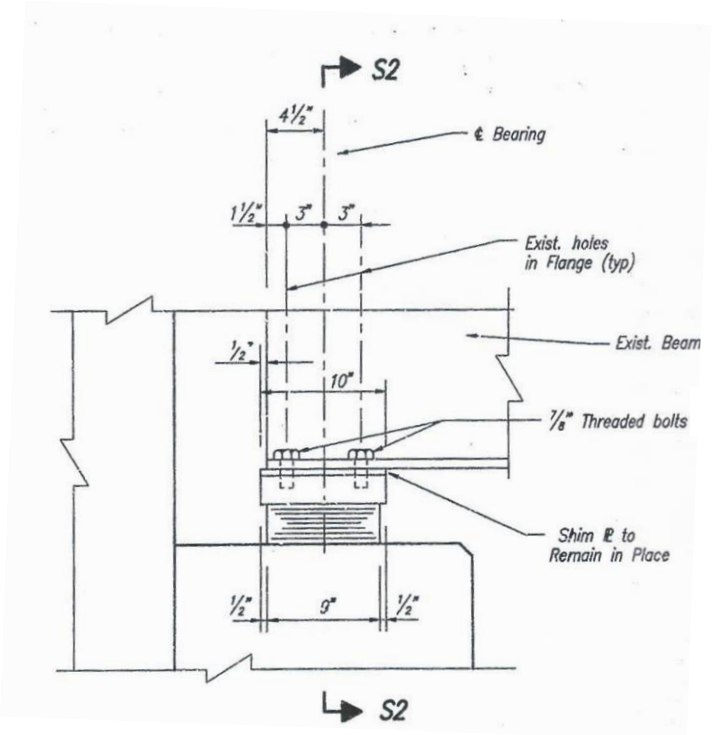

Figure 2.6: Indiana DOT's bearing assembly for elevating a bridge

The Illinois Department of Transportation does not raise existing bridges with steel pedestals. Instead, steel shim plates may be placed between the elastomeric bearing assembly and the superstructure if the height adjustment is less than 6 inches (Figure 2.7). For adjustment heights between 6 and 12 inches, 1 inch fabricated plates should be used (Figure 2.8). If the extension is greater than 12 inches, as in the case of a grade raise, a concrete extension is used to elevate the bridge (Figure 2.9). The bearing seat area of the abutment or pier is reconstructed to provide the proper elevation for the new elastomeric bearing assemblies (Illinois Department of Transportation).

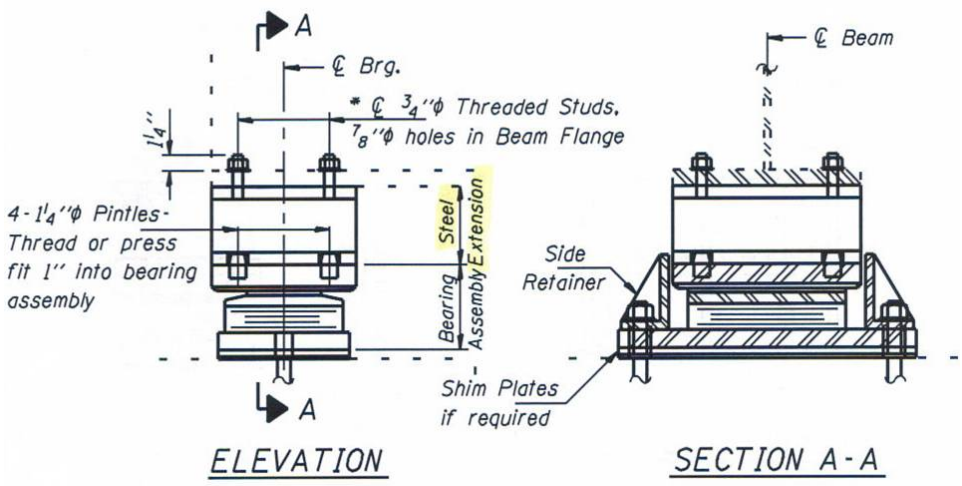

Figure 2.7: Stacked plate steel extension (Illinois DOT)

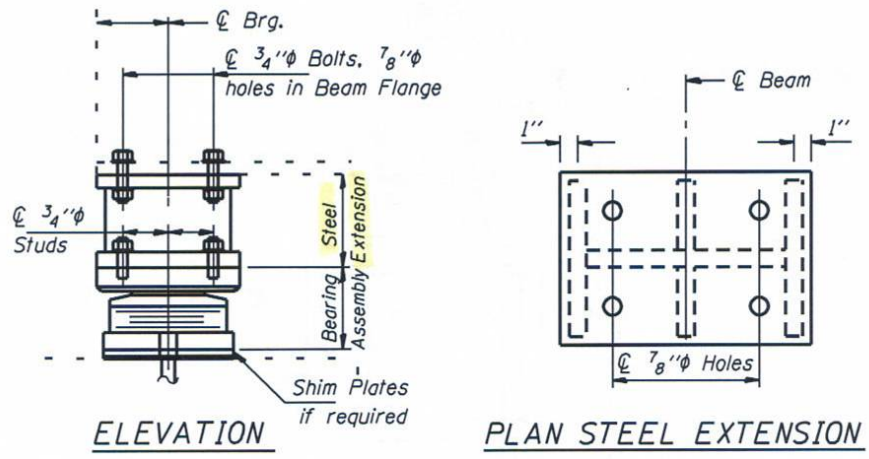

Figure 2.8: Fabricated steel extension (Illinois DOT)

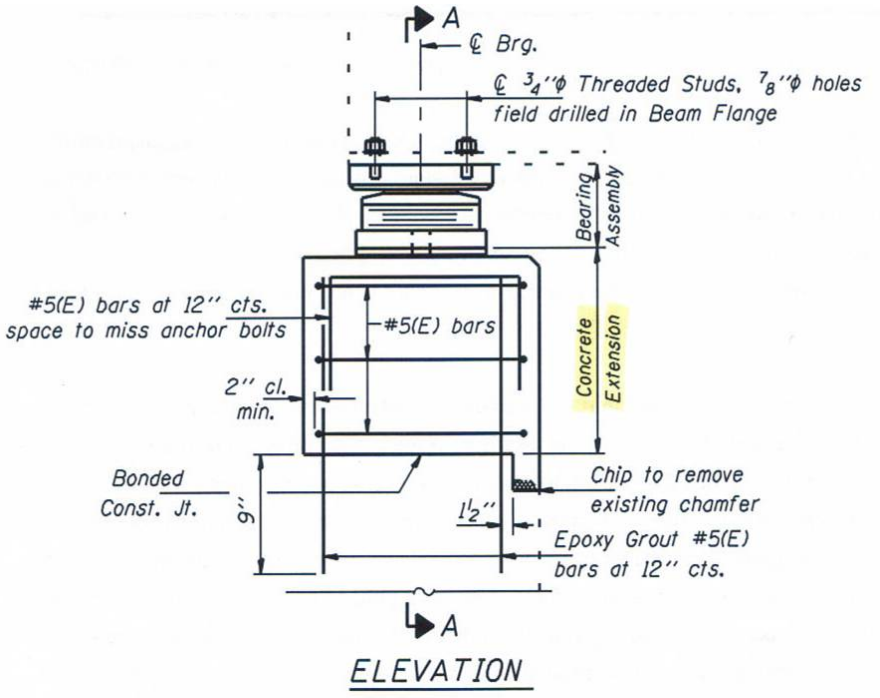

Figure 2.9: Concrete extension (Illinois DOT)

The Missouri Department of Transportation (MoDOT) has not raised the superstructure of any slab-on-girder bridge to increase the vertical clearance of the roadway beneath the bridge. However, MoDOT has raised laterals, wind bracing and portals to increase the vertical clearance on through-trusses (Hartnagel 2004).

2.4 Seismic Performance of Bridges

Many lessons have been learned about the seismic performance of bridges, especially after the 1971 San Fernando (California) earthquake, which was a major turning point in the development of bridge seismic design criteria and the initiation of retrofit programs (Roberts 1990; Yashinsky 1991). However, widespread awareness of bridge seismic vulnerability in areas of low-to-moderate seismicity such as the CSUS did not begin to develop until about 20 years later (Nielson 2005).

Severe damage from the 1971 San Fernando earthquake in the Los Angeles area exposed the following bridge vulnerabilities:

1. unseating of supports and collapse of the superstructure
2. brittle shear failures in columns and piers before flexural yielding occurred
3. inadequate anchorage that caused pullout failures of vertical column from foundations and superstructures
4. foundation and embankment failures

Current seismic design criteria and retrofit methodologies have addressed some of these shortcomings by including larger design force levels and detailing to provide adequate seismic resistance for bridge structures. Additionally, seismic design criteria focus on controlling the mode of failure such that ductile flexural yielding occurs instead of brittle shear failures as observed from the 1971 San Fernando earthquake, 1987 Whittier Narrows earthquake, and 1989 Loma Prieta earthquake, to name a few (Fung, Lebeau et al. 1971; Housner 1971).

Research funded by the National Science Foundation (NSF) and the California Department of Transportation (Caltrans) has also advanced the current state-of-the art of seismic bridge design and seismic retrofitting. Standards have been developed and adopted nationwide by the American Association of State Highway and Transportation Officials (AASHTO) and the Federal Highway Administration (FHWA). These standards have provided detailed guidelines for the preliminary screening, detailed evaluation, and design of retrofit measures for highway structures in the Seismic Retrofitting Manual for Highway Structures, Part 1-Bridges (Buckle et al. 2006). New and improved technologies have contributed to the understanding and enhancement of energy dissipation devices and base isolators that can be installed on structural members to minimize seismic demands. Other conventional retrofit measures such as column jacketing have also been outlined in the Seismic Retrofit Manual for Highway Structures, Part 1-Bridges, to increase the structural capacity. In summary, significant progress has been made in the development of guidelines for seismic design and retrofitting of highway structures based on past performance of highway structures during earthquakes and fundamental research.

2.5 Bridge Bearings

The behavior of high-type (rocker/bolster) and low-type (sliding) bridge steel bearings, which are commonly used in the CSUS (Figure 2.10) and which have performed poorly in past earthquakes, is of concern to CSUS bridge engineers. High-type (rocker) and low-type (sliding) steel bearings can be classified into two types, fixed and expansion bearings based on the movement they allow or prevent (Figures 2.11 and 2.12, respectively). High-type (rocker) bearings have typically been used for spans greater than 65' and low-type (sliding) bearings have typically been used for spans less than 65' in length (Dutta 1999; Nielson 2005).

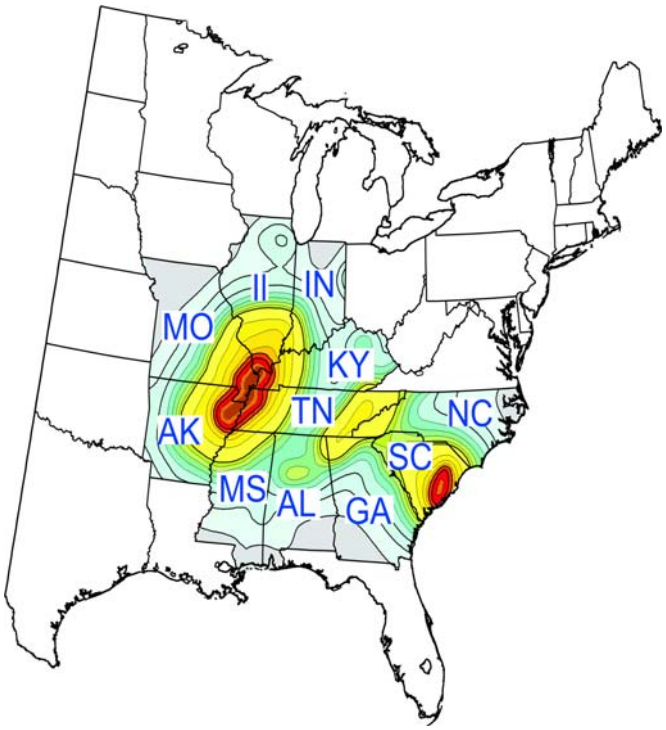

Figure 2.10: Central and Southeastern United States (CSUS) region considered for this study

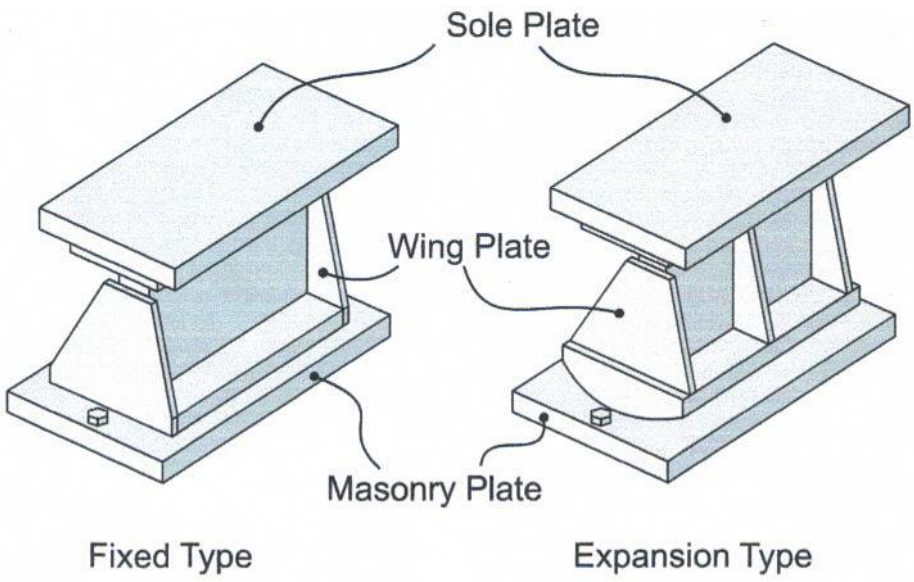

Figure 2.11: High-type steel (rocker/bolster) bearings (Nielson 2005)

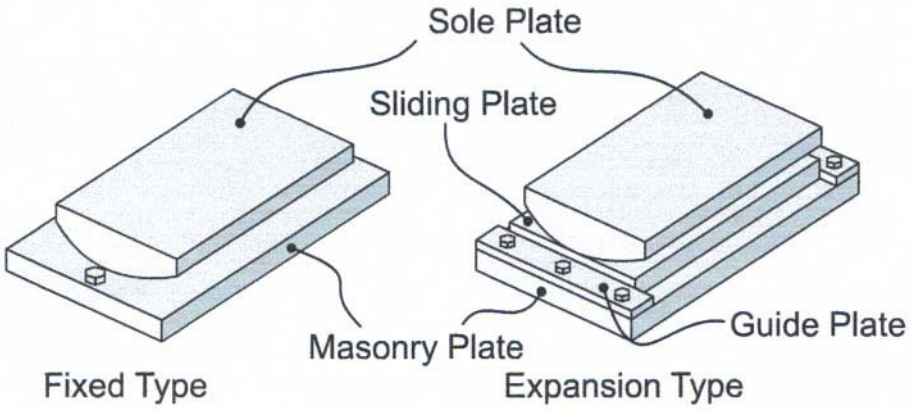

Figure 2.12: Low-type (sliding) bearings (Nielson 2005)

Limited cyclic experimental testing has been reported on the performance of steel bridge bearings. More than twenty years ago, monotonic tests were conducted on rocker bearings to determine frictional coefficients under longitudinal movements for ordinary service thermal loading (Mazroi, Wang et al. 1983). However, Mander et al. (1996) conducted cyclic lateral load tests on both rocker and sliding bearings since many of those vulnerable bearings are still in service today on many bridges in the CSUS. The results from the reversed cyclic lateral load tests provided realistic force-displacement responses to be used for proper modeling and analysis. The tests were conducted in both longitudinal and transverse directions for each bearing based on typical field conditions (Figures 2.13 through 2.16). Vertical load on the specimen remained constant for each test. Other parameters explored included the level of velocity dependency and the effect of unloading-reloading (Mander, Kim et al. 1996). Testing was complemented with nonlinear analytical models developed in DRAIN-2DX to represent the behavior of the bearings.

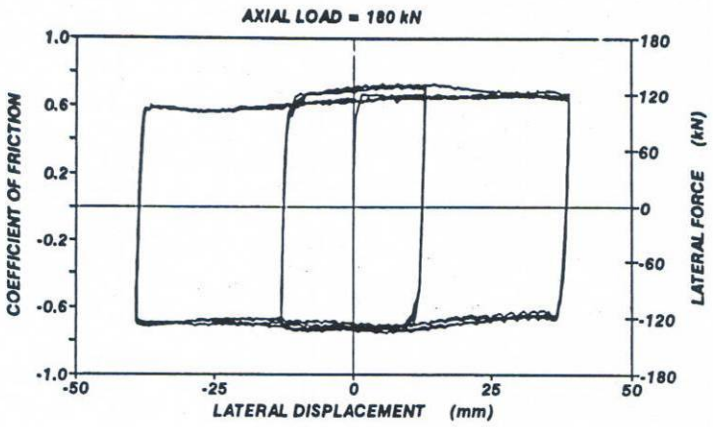

Figure 2.13: Experimental test results for the low-type (sliding) bearings – longitudinal direction (Mander et al, 1996)

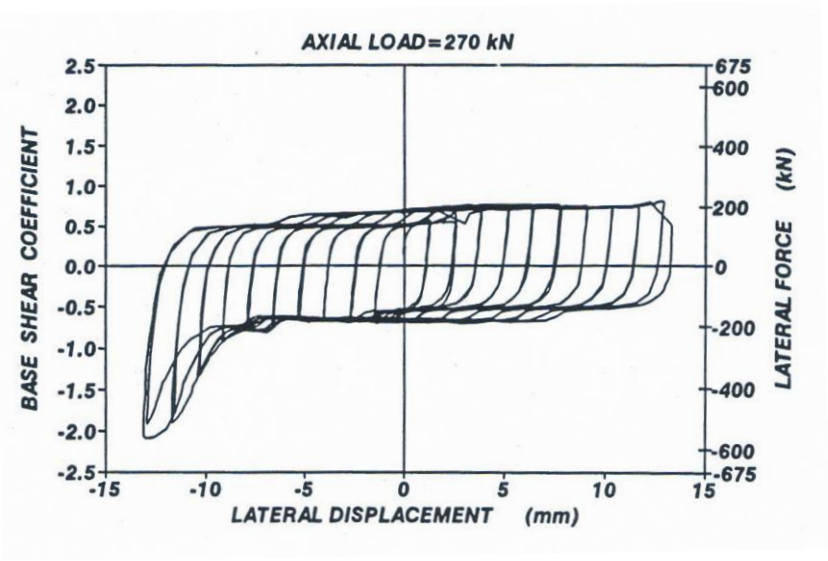

Figure 2.14: Experimental test results for the low-type (sliding) bearings – transverse direction (Mander et al, 1996)

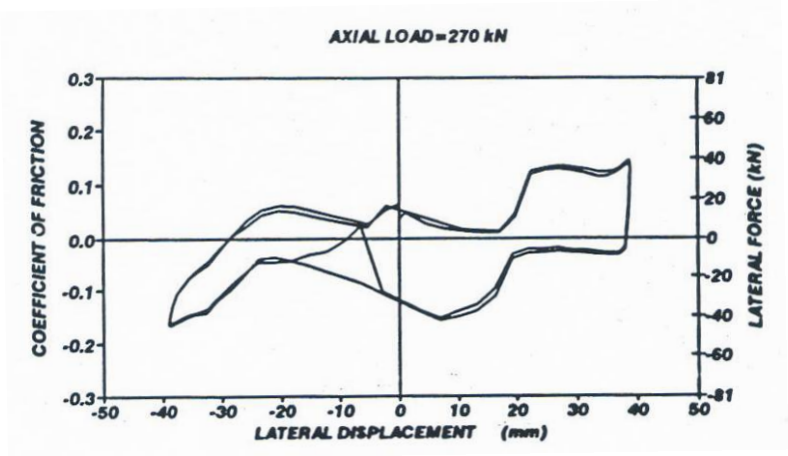

Figure 2.15: Experimental test results for the high-type (rocker/bolster) bearings – longitudinal direction (Mander et al, 1996)

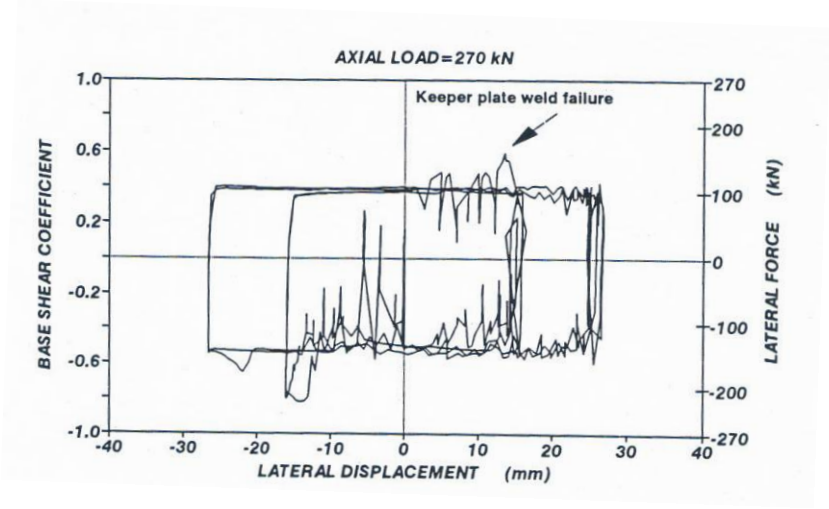

Figure 2.16: Experimental test results for the high-type (rocker/bolster) bearings – transverse direction (Mander et al, 1996)

Previous research has also been conducted to validate the vulnerability of bearings within multi-span simply-supported (MSSS) bridges as observed in past earthquakes such as the 1976 Guatemala City (Guatemala) earthquake, 1980 Eureka (California, USA) earthquake, and 1995 Kobe (Japan) earthquake (Dicleli and Bruneau 1995). This research indicates that there exists a lack of strength, ductility, and stability of these bearings in MSSS bridges (Mayes, Buckle et al. 1990; Dicleli and Bruneau 1995; Rashidi and Ala Saadeghvaziri 1997; DesRoches, Leon et al. 2000; Kim, Mha et al. 2006). More specifically, the following damage was reported regarding the performance of bearings in many older bridges: damage to rocker bearings in the 1989 Loma Prieta (California, USA) earthquake, failure of keeper plates on a sliding bearing during the 1991 Talamanca (Costa Rica) earthquake, and toppling of rocker bearings during the 1993 Scott Mills (Oregon, USA) earthquake (Mitchell, Sexsmith et al. 1994).

Since steel bearings transfer loads from the bridge deck to the columns like bridge steel pedestals, it is hypothesized that steel pedestals may also be found to be vulnerable bridge components. Some potential vulnerabilities include instability, limited strength and deformation capacity, and poor performance of connection details, particularly on multi-span simply supported (MSSS) bridges that are common in the CSUS as past earthquakes and research has revealed. Experimental testing of steel pedestals will add to the current state of knowledge of steel pedestals as bearing elements, thereby providing realistic force-displacement responses to calibrate an analytical model used to evaluate the seismic performance of bridge steel pedestals.

CHAPTER 3

EXPERIMENTAL TEST SETUP

3.1 Overview

Since it is hypothesized that steel pedestals may behave as unstable steel bearings performed in past earthquakes, an experimental study of six full-scale tests of a 40' two-girder bridge specimen is conducted to evaluate the performance of 19" and 33½" steel pedestals subjected to quasi-static loading. The major testing objective is to assess any structural vulnerabilities, if any, of the steel pedestals due to lateral loads. Other objectives include assessing the strength and deformation capacity of the pedestals from the experimental test results presented in the next chapter. The details of the experimental test setup are described in this chapter. Particular emphasis is placed on the design of the experimental test setup, bridge substructure, steel pedestals, bridge superstructure, instrumentation, and methodology for testing is presented. The six testing configurations are discussed within the context of a testing matrix where the test procedure and loading protocol are described.

3.2 Testing Facility

Full-scale testing of the 40' two-girder bridge specimen was conducted in the Structures Laboratory at the Georgia Institute of Technology in Atlanta, Georgia. The specimen sat on a 6'-0" thick concrete strong floor and was loaded laterally by an actuator connected to a large L-shaped structural reaction wall.

The structural wall and floor have a series of four anchor points that are located at 4'-0" on center. The actuator used for testing is situated on an anchor point that is comprised of straight, horizontal tubes in an 8" square pattern to accommodate high strength threaded Dywidag bars that are threaded through the wall. Each Dywidag bar has a service capacity of 50 kips, with a factor of safety of 2.5 to provide a comfortable margin for low cycle fatigue loading.

3.3 Test Setup

The test setup consists of a 40' two-girder bridge specimen resting on rollers at one end and on steel pedestals connected to reinforced concrete cap beams via post-installed stainless steel stud anchor bolts at the other end. The piers are post-tensioned to the structural floor. From the structural floor to the centerline of the actuator, the bridge specimen is elevated 6'-1" for all six tests. The experimental test setup for the 19" and 33½" pedestals tested are shown in Figures 3.1 and 3.2, respectively. The construction of the test setup is based on field conditions for installing steel pedestals and its connection elements. Assemblage of the superstructure, steel pedestals, and substructure for the experimental test setup are presented next.

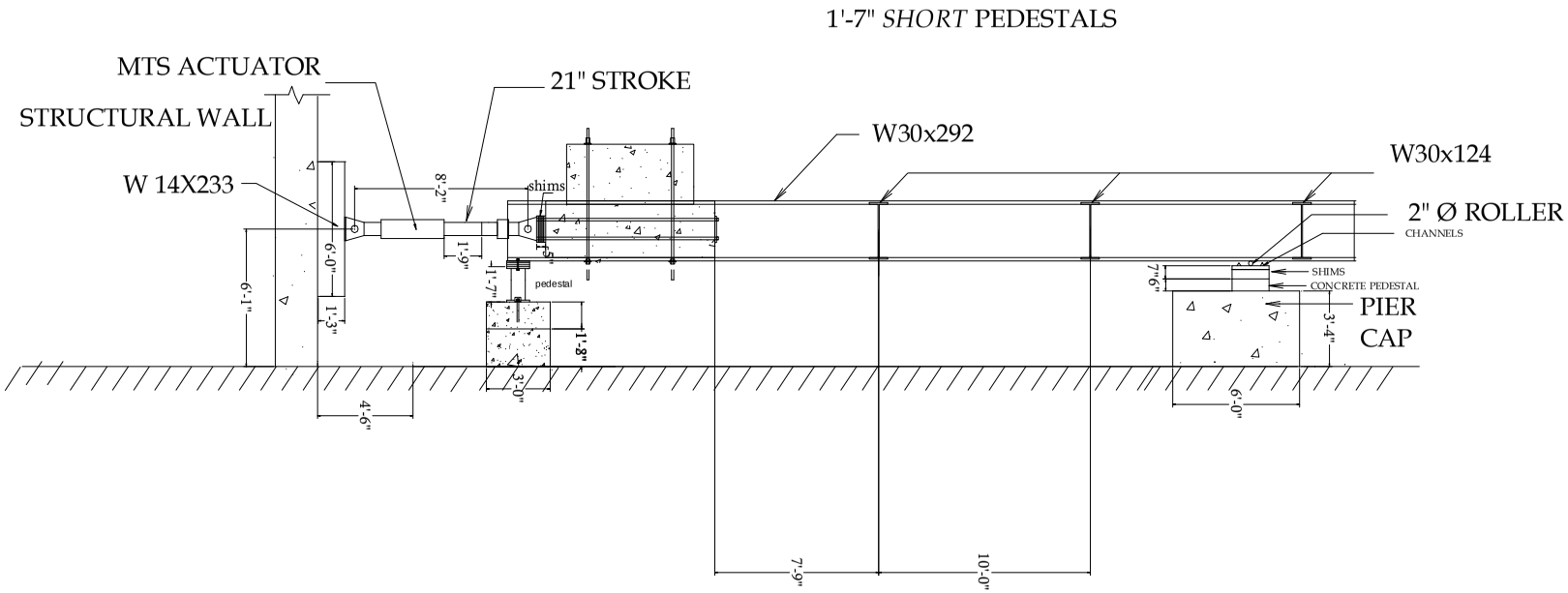

Figure 3.1: Experimental test setup for 19-inch ("short") pedestals

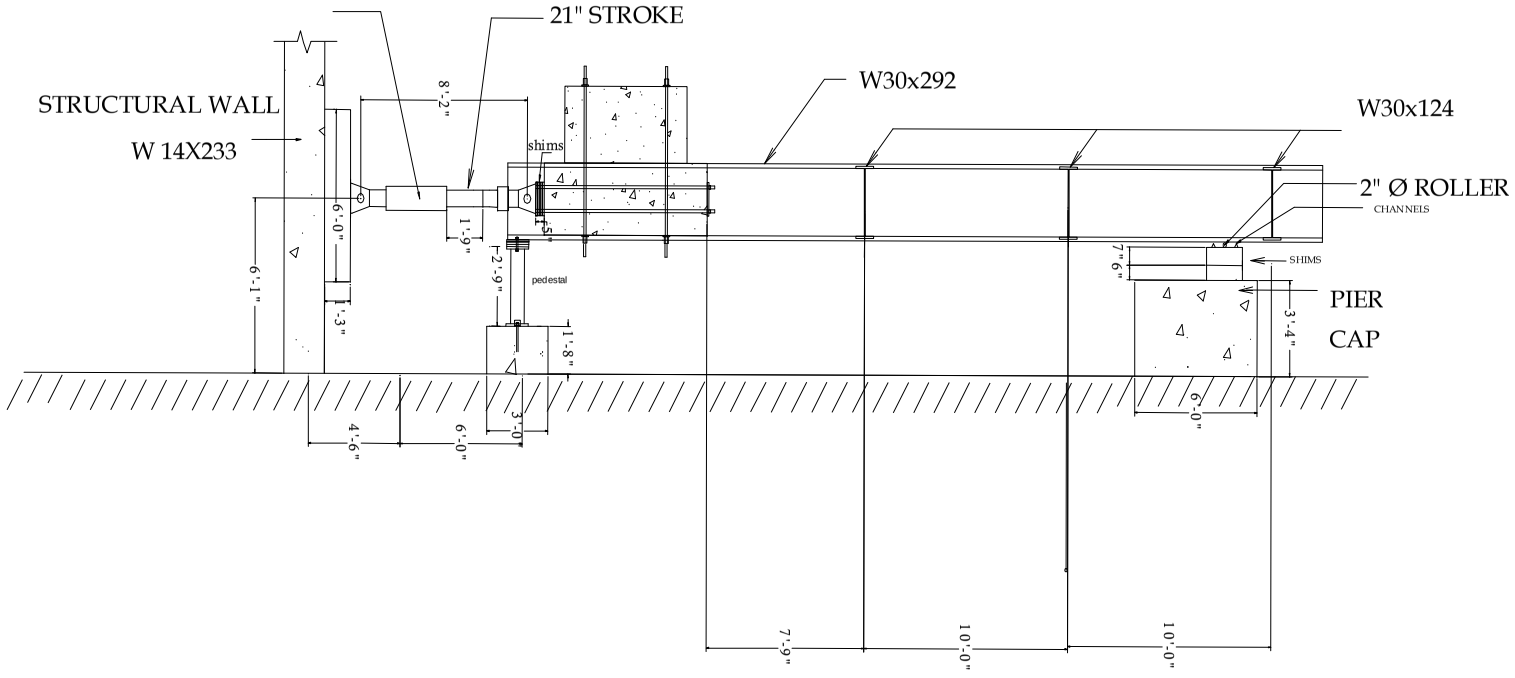

Figure 3.2: Experimental test setup for 33½-inch ("tall") pedestals

3.4 Bridge Superstructure

The large-scale bridge model used in this research was built by Lam (2001) and by Pfeifer (2002). It is based on an existing steel girder bridge in Tennessee. The bridge superstructure consists of two main girders and three transverse beams that are connected with A325 bolts. The two main girders are A36 W30x292 steel sections and span 40'-0" at a distance of approximately 7'-9½" from the centerline of the two girders (Figure 3.3). Three W30x124 transverse stiffener beams are spaced between the main girders to maintain the in-plane loading of the bridge while minimizing torsional effects (Figures 3.4 through 3.6). Two concrete blocks weighing 20 and 22 kips, respectively, are used to model the dead weight of the bridge. The first block, a 8'-0" x 7'-8½" x 2'-6" reinforced concrete monolith, is wedged between the main girders, and a second block, a 6'-0" x 8'-0" x 2'-8" unreinforced concrete monolith, rests on top of the reinforced concrete block (Figure 3.7).

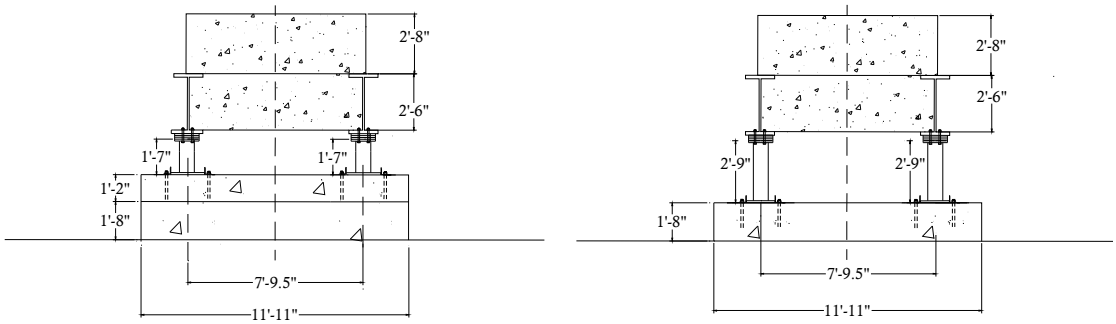

CROSS-SECTION
"short" pedestals

CROSS-SECTION
"tall" pedestals

Figure 3.3: Cross-sectional view of test setup for the 19"and 33½" pedestals

Figure 3.4: Perspective view of three W30x124 transverse beams and wedged concrete block

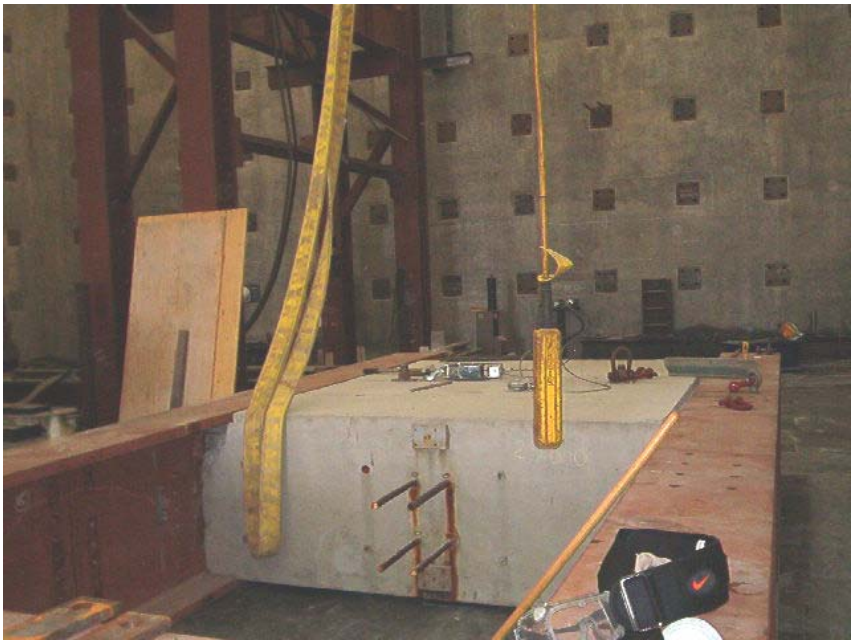

Figure 3.5: Reinforced concrete block wedged between the two W30x292 girders

Figure 3.6: Aerial view of dead load reinforced concrete block wedged between girders

The blocks were cast with four horizontal tubes to allow for post-tensioning of both blocks since the actuator is to be attached to the lower block. Post-tensioning the blocks to each other helps to prevent slippage between the blocks during loading. The reinforced concrete block, which is wedged between the girders, provides the bearing surface for the actuator to transfer loads (Figure 3.8).

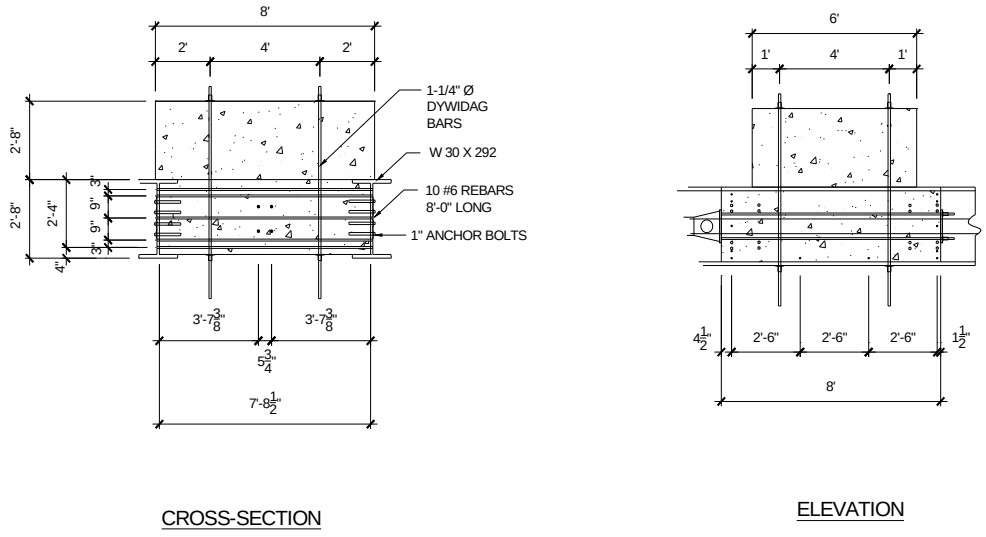

Figure 3.7: Reinforcement for dead load concrete blocks (Pfeifer 2002)

While 3"-diameter holes were core drilled 12" into the reinforced cap beams, which serve as the substructure as shown in Figure 3.8, the superstructure is erected onto temporary wood supports on top of the reinforced concrete piers (Figure 3.9).

Figure 3.8: Drilling holes into cap beams for post-installed stud anchor bolts (pictured: Jason Crouse, undergraduate laboratory assistant)

Figure 3.9: Erection of superstructure on temporary wood supports before connected to steel pedestals

The superstructure is connected to the pedestals, which, in turn are connected to the substructure (Figure 3.10). An aerial view of the 40' span test setup is shown in Figure 3.11. To prevent out-of-plane movement of the setup for loading in the longitudinal direction, two square columns are placed within an inch of the north and south side of each girder. The square columns are bolted to a spreader beam that is post-tensioned to the structural floor (Figure 3.12).

Figure 3.10: Connectivity of bridge assembly to 19" steel pedestals

Figure 3.11: Aerial view of bridge assembly

Figure 3.12: Erection of square columns to restrict out-of-plane movement

3.5 Bridge Steel Pedestals

The bridge steel pedestals are W-shape sections or built-up members, designed and fabricated by Bellamy Brothers, a contractor that has done this type of work for the Georgia Department of Transportation (GDOT). For this experimental investigation, 19" and 33½" steel pedestals are used and tested under six (6) configurations for loading and positioning of the post-installed stainless steel stud anchor bolts. The 19" pedestals chosen for this investigation are based on GDOT Bridge No. 72, Sandy Run over I-95 in Liberty County, Georgia. The 33½" pedestals used for testing are made available from GDOT Bridge on I-75 over Franks Creek in Lowndes County, Georgia, although these pedestals were rescinded from use because of the uncertainty of their performance and potential vulnerability due to instability. The 19" pedestals consist of a W8x31 section with 1" top and bottom plates that are welded to the W8x31 (Figure 3.13). The top and bottom plates have dimensions of 13" by 9" (Figure 3.14). The 33½" pedestals consist of a built-up section, also with 1" top and bottom plates welded to the members (Figures 15 and 16). For the short and tall pedestals, holes are drilled into the top plates to provide connectivity of the anchor bolts to the girders.

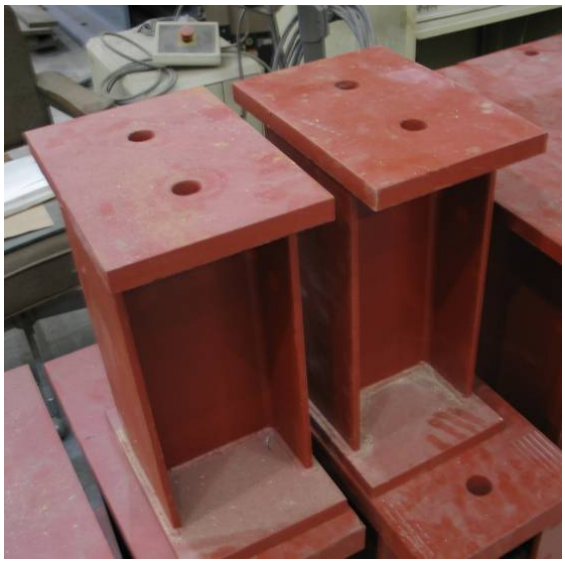

Figure 3.13: Photograph of 19" steel pedestals consisting of a W8x31 section

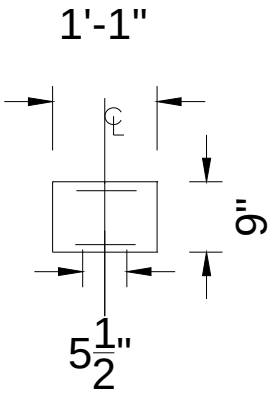

Figure 3.14: Dimensions of top plate of 19" steel pedestals

Figure 3.15: Photograph of 33½" steel pedestals consisting of built-up members

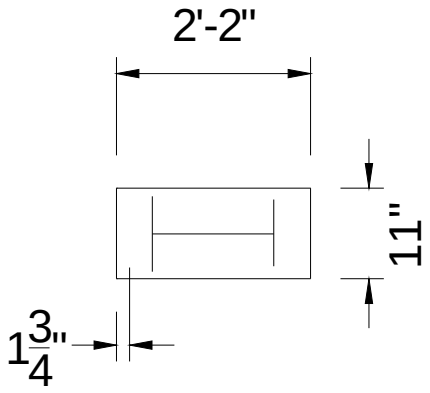

Figure 3.16: Dimensions of top plate of 33½" steel pedestals

Loads are resisted by 1¼" stainless steel stud anchor bolts that are set with a high strength grout in the drilled holes. Proper anchorage of the stud anchor bolts is important for the development of the bolt capacity. The stainless steel anchor bolts are 16" in length and embedded 12" within the cap beam as per field procedures specified by Bellamy Brothers. The stud anchor bolts are anchored in a non-shrink grout that conforms to the Corps of Engineers Specification, CRD-C 621 (ASTM C1107). Loads

are transferred to the stud anchor bolts either through 4" by 4" by ½" L-shaped angles that are welded to the base plate of the pedestals as shown in Figure 3.17 or when the anchor bolts themselves are placed within the cross-section as shown in the testing matrix in *Section 3.8*. The L-shaped angles have a slot in the angle that enables the anchor bolts to be aligned. A high strength grout is used to set the anchor bolts, where precise measurements are taken so that the anchor bolts are properly aligned with the centerlines of the pedestals and girders. The pedestals rest on a ⅛" elastomeric (neoprene) pad. Steel plates and the reused bearings are placed between the superstructure and the rigid 1" top plate. With the pedestals in place, the superstructure is connected with A36 anchor bolts and the nuts of the stainless steel stud anchor bolts are hand-torqued with a very long pipe attached to a wrench to provide the fixity to the substructure (Figure 3.18).

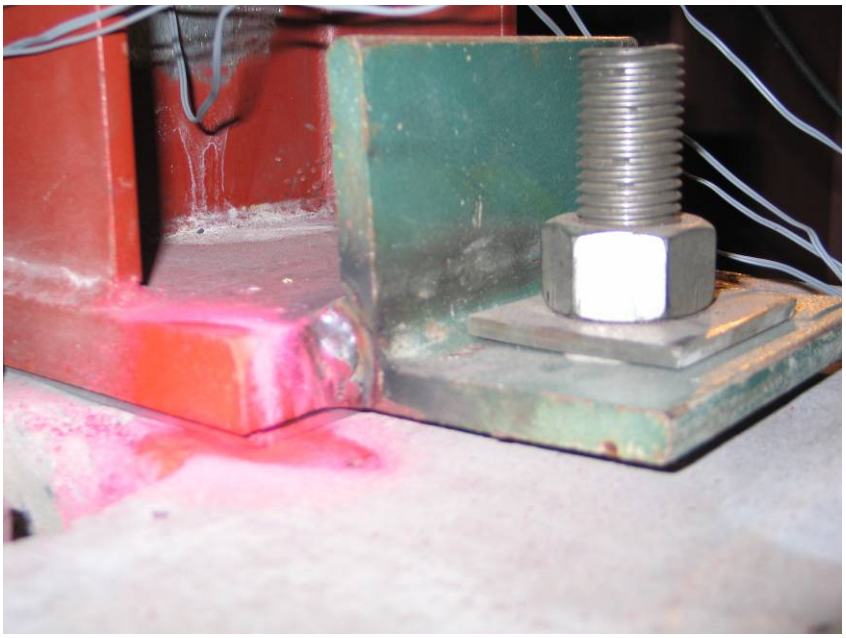

Figure 3.17: L-shaped angles welded to the base plate of the pedestals

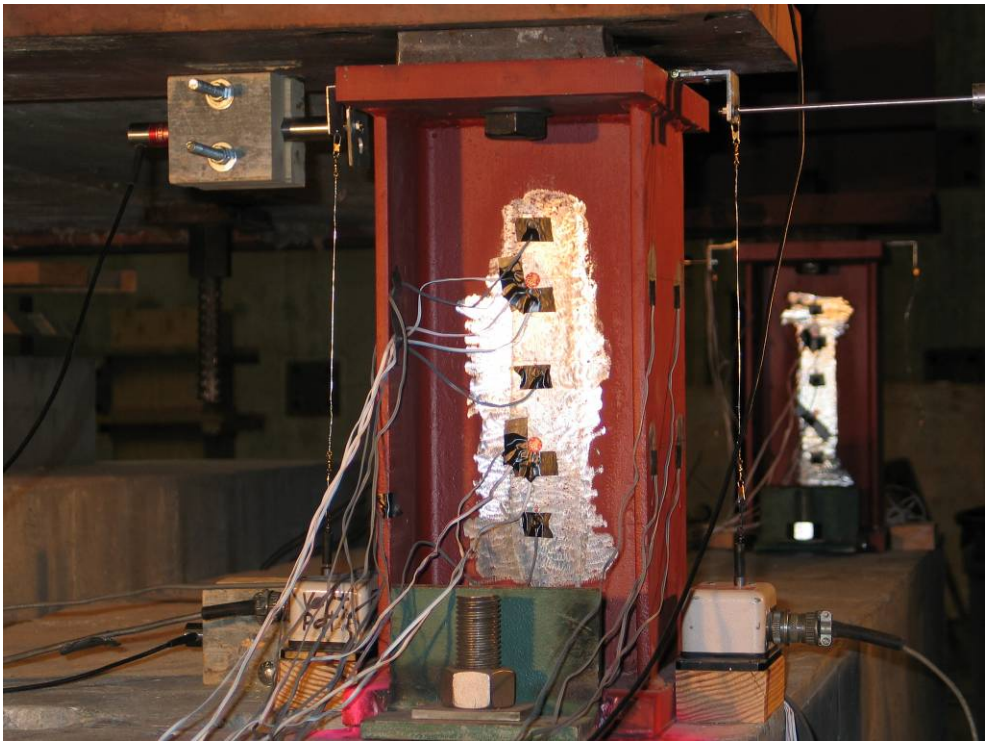

Figure 3.18: Short pedestals connected to the superstructure and substructure with stainless steel stud anchor bolts

3.6 Bridge Substructure

To accommodate the varying heights of the steel pedestals in question without having to vary the existing height of the actuator positioned on the reaction wall, two new reinforced concrete cap beams are cast while reinforced concrete piers are reused from Lam (2001) and Pfeifer (2002) to act as the substructure for the experimental test setup. The newly cast reinforced concrete beams have heights of 14" and 20", and are stacked on top of each other to easily accommodate the 19" and 33½" pedestals. A high strength mortar is placed between the beams to minimize slip between the blocks. Holes in the center of the beams are cast-in-place and Dywidag bars are inserted for post-tensioning the two blocks to allow for connectivity of the cap beam to the structural floor. The newly cast reinforced concrete cap beam is based on the abutment support steel

reinforcement details of GDOT Bridge No. 72 to accurately predict the behavior of the connection of the steel pedestals to the bridge pier caps (Figure 3.19). The details of the newly cast reinforced concrete pier cap is shown in Figure 3.20. A concrete strength of 3500 psi is specified and provided by a local ready-mix plant in Georgia. From two 4"x8" cylinder tests, the average 28-day compressive concrete strength is approximately 5800 psi.

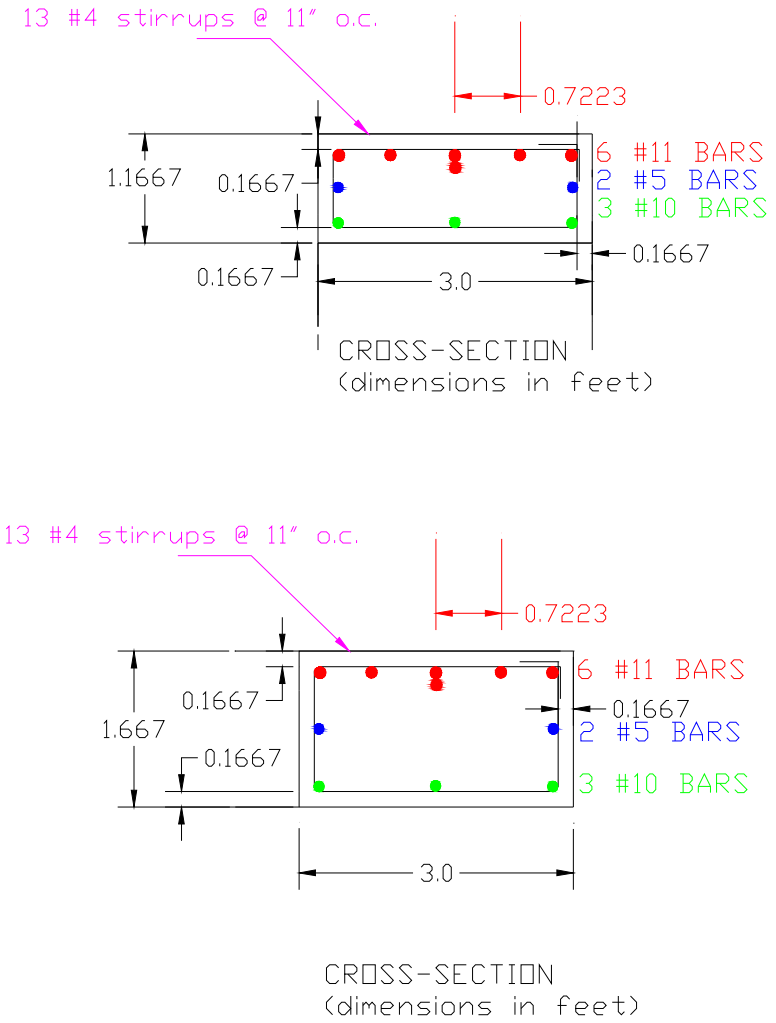

Figure 3.19: Details of steel reinforcement for piers

Figure 3.20: One of the newly cast reinforced concrete cap beams

3.7 Instrumentation

The steel pedestals are instrumented to determine the strain and displacement kinematics of the bridge system. To monitor the data of the experimental testing, an OPTIM Electronics MEGADAC model 3415AC is used to collect the data readings from the sensors at a specific scan rate. This data acquisition system samples data up to 25,000 times per second with a maximum capacity of 300 channels of input. For the experimental tests herein, two readings of data are captured per second. The MEGADAC 3415AC is connected to an external computer and controlled remotely by the OPTIM Test Control Software (TCS), so that data can be easily exported.

Five different types of sensors are used to monitor the data, and are shown in Figures 3.21 and 3.22:

1. linear variable differential transducers (LVDT) – to measure relative displacements
2. one load cell with an LVDT located on the MTS actuator – to measure the force and displacement applied to the entire bridge specimen
3. uniaxial strain gauges – to measure axial strains within the pedestal at different height locations
4. triaxial rosettes – to measure the strains in 3-directions and compare the axial strain measured to the measurements recorded by the uniaxial strain gauges
5. string potentiometers – to measure the rotation (rocking) of the pedestals as the system is displaced laterally

In this test setup, LVDTs are placed on the bridge components to measure the relative displacement, if any, between 1) the girders and the dead load concrete block, 2) the actuator load cell with LVDT, Δ_1, 3) the girders and each pedestal, Δ_2, 4) the pedestals and a fixed reference, Δ_3, and 5) sliding between the concrete surface and the pedestal base that rests on the elastomeric (neoprene) pad, Δ_4. The uniaxial strain gauges and triaxial rosettes used are from Tokyo Sokki Model FLA and FRA ones obtained from Texas Measurements (TML). The uniaxial strain gauges, FLA-1-11-3L, are placed on the pedestal flanges to measure the strain as a quarter-bridge. These gauges are used to compute the moments and therefore shear forces in the system from the strains measured (Figure 3.23). The 45º-90º-45º rosettes, FRA 5-11-LT, are evenly spaced along the web of the pedestals with two levels of strain gauges placed on the pedestal flanges roughly at the third points. Two strain gauges are intermittently spaced along the web between the rosettes (Figure 3.24). String potentiometers are placed alongside the pedestals in the

plane of loading to measure the uplift of the pedestal relative to the cap beam during loading. Mechanical dial gauges are used in most of the tests to quantify the uplift in the bolts during loading (Figures 3.25 and 3.26). String potentiometers are also used to ensure the cap beams, Δ_5 and Δ_6, act as monolithic members where neither slippage nor sliding occurs. The string potentiometers are attached with a high strength epoxy from the cap beam to the "fixed" reference.

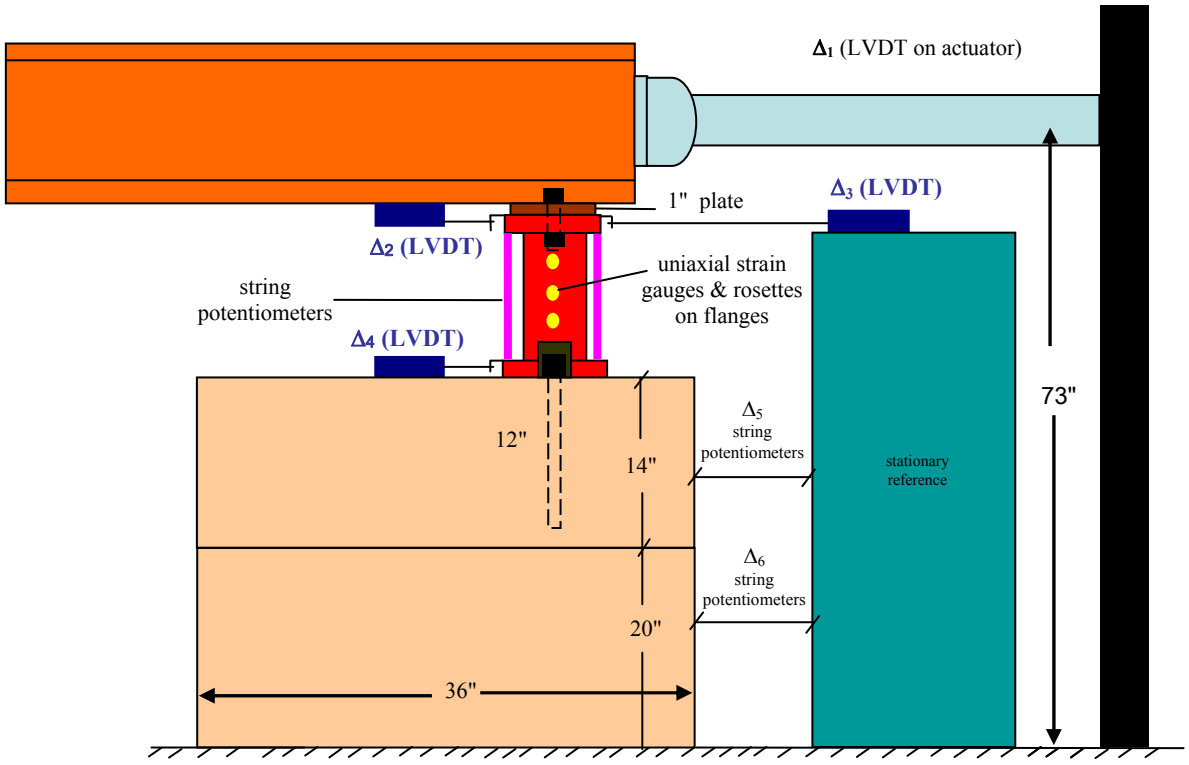

Figure 3.21: Schematic view of instrumentation for experimental test setup

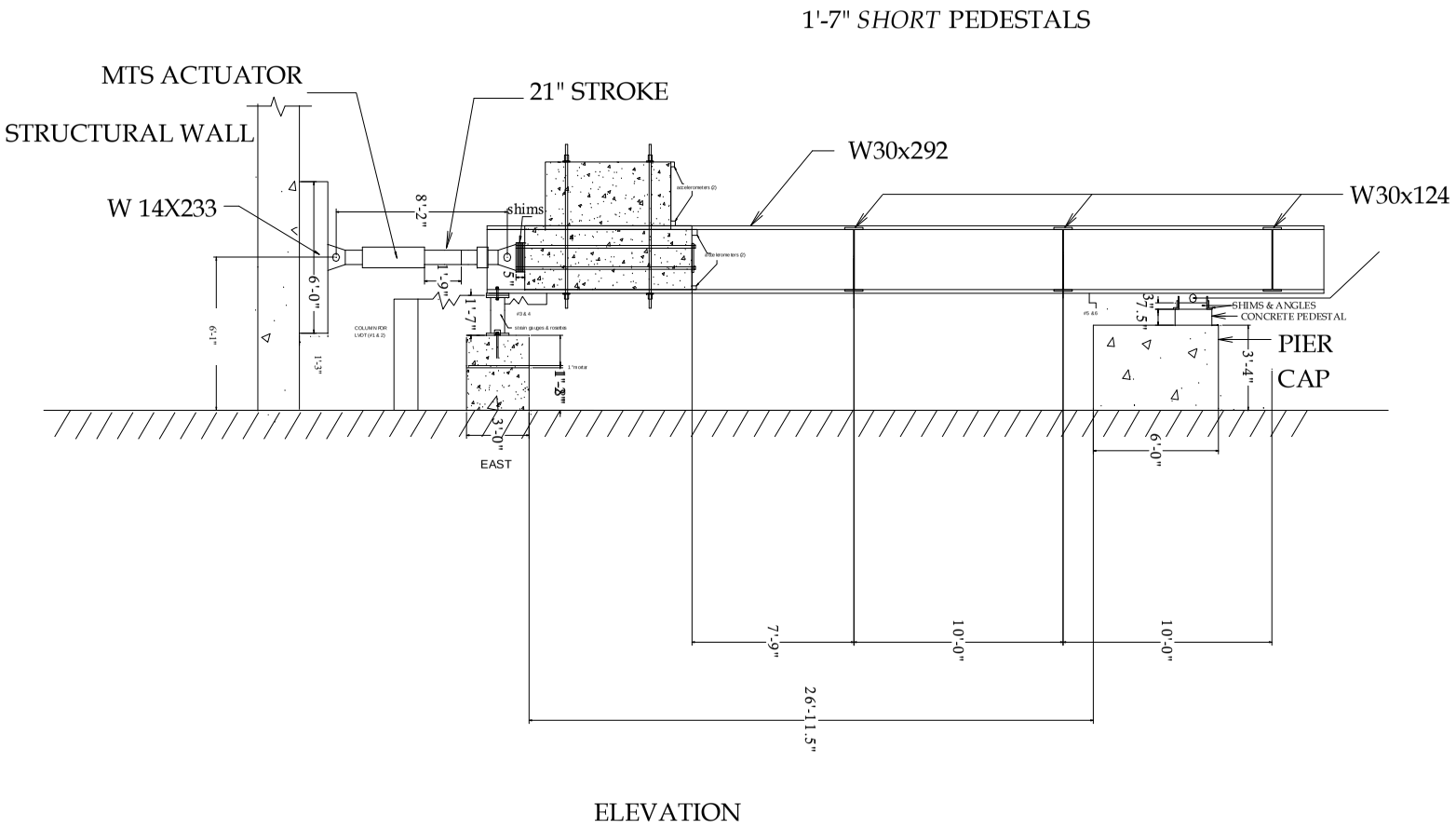

ELEVATION

Figure 3.22: Instrumentation for experimental test setup

Figure 3.23: Mechanical dial gauge to measure uplift of stainless steel stud anchor bolts (tall pedestal, strong-axis testing with bolts attached to welded angles)

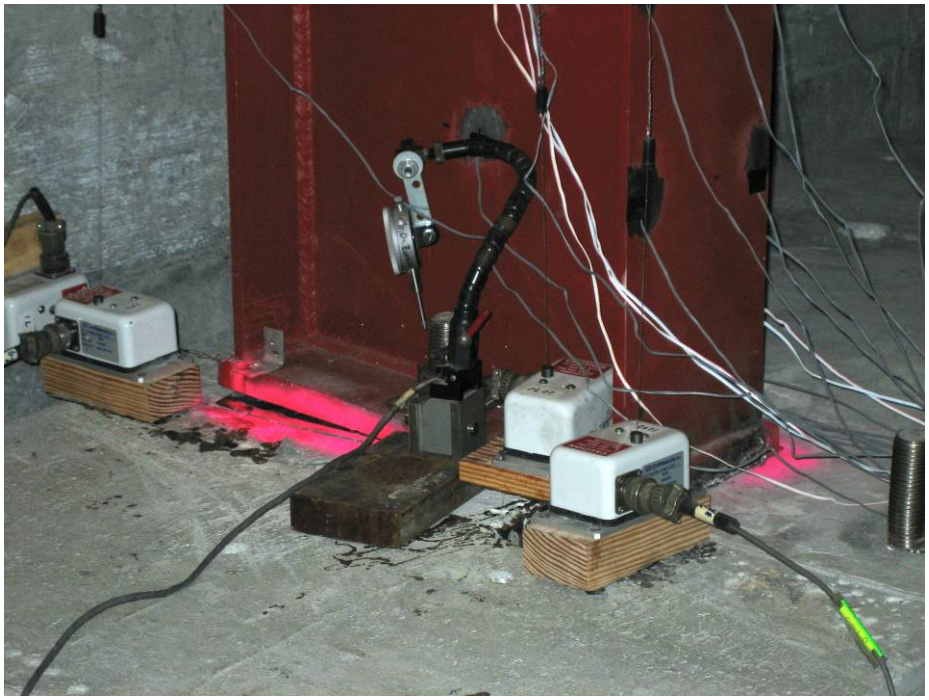

Figure 3.24: Mechanical dial gauge to measure uplift of stainless steel stud anchor bolts (tall pedestal, strong-axis with bolts within the cross-section)

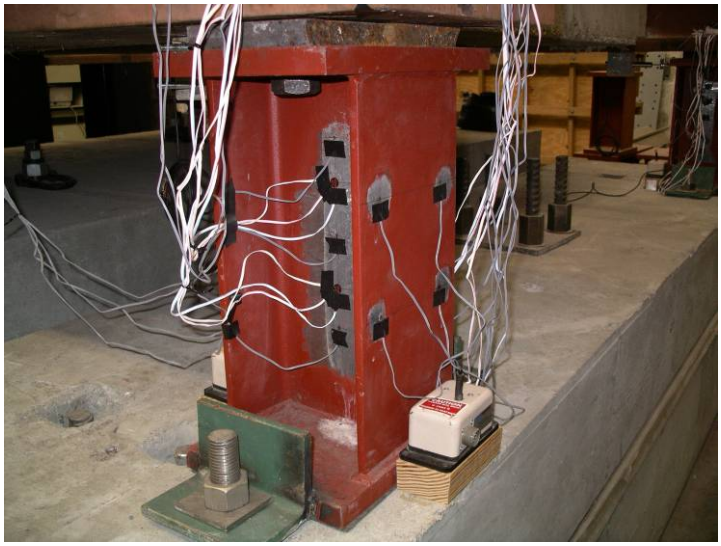

Figure 3.25: Strain gauges are placed at the third-points on the flanges to obtain the cross-sectional stress distribution

Figure 3.26: Strain gauges and rosettes are placed along web and string potentiometers are placed alongside pedestal

3.8 Testing

3.8.1 Hydraulic actuators

To assess the behavior of steel pedestals, quasi-static tests are conducted using an MTS hydraulic actuator that is post-tensioned to the structural wall. A spreader beam is post-tensioned to the structural wall, and supports the MTS actuator that applies the loading to the structure (Figure 3.27). An MTS 243.45 actuator is used for tests P1-1 through P2-2 and an MTS 243.35 is used for tests P3-1 and P3-2. The actuators measure the displacement via an LVDT (Δ_1) and load imposed on the bridge specimen via a high capacity load cell. The tests are conducted in displacement control. The actuator is powered by a 150 gpm hydraulic power supply and single 15 gpm servovalve that are connected to the 8'-0" x 7'-8½" x 2'-6" concrete block wedged between the two steel girders (Figure 3.28). The dual servovalves are used to displace the full-scale bridge during testing, and can allow for the actuator to theoretically displace up to a maximum speed of 12 inches per second.

Figure 3.27: Spreader beam positioned and post-tensioned to structural wall

Figure 3.28: MTS 243.45 actuator attached to dead weight reinforced concrete monolith positioned between the girders

3.8.2 Testing matrix

The testing matrix consists of six (6) configurations of pedestal orientations and anchor bolt placement. The experimental design intends to assess how pedestal orientation and anchor bolt configuration affect the local and global response. The various orientations and anchor bolt configurations are based on actual bridge plans provided by the GDOT for cases where bridges have been elevated with steel pedestals. The steel pedestals are oriented such that the steel pedestal is loaded along is strong- or weak-axis of bending with the anchor bolts either attached to angles welded to the base plate or within the cross-section. The various configurations of loading are similar to tests conducted by Mander et al. (1996) on high-type and low-type steel bearings to better understand the strength and capacity demands produced by seismic events. Table 3.1 presents the testing matrix for the six (6) reversed, cyclic quasi-static tests conducted on both 19" and 33½" steel pedestals.

Table 3.1: Testing Matrix for Steel Girder Bridge Rehabilitated with 19" and 33½" Steel Pedestals

	Phase I (P1)	**Phase II (P2)**	**Phase III (P3)**
Loading Direction	Short Pedestals 19"	Tall Pedestals 33½"	
P →	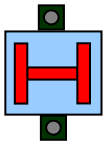  P1-1	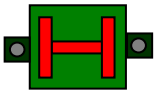  P2-1	  P3-1
→	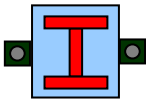  P1-2	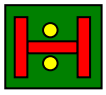  P2-2	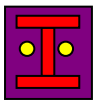  P3-2

3.9 Loading Protocol

The loading protocol consists of reversed cyclic loading to target displacements, typically in increments of 0.25" and/or 0.5". However, the loading rate is 2 inches per minute for tests P1-1 through P2-2 and 1 inch per minute for tests P3-1 and P3-2. In all cases, the loading rate is slow enough such that the effects of strain rate can be ignored. Figure 3.29 shows a portion of a typical loading protocol for a quasi-static, reversed cyclic test conducted in displacement control. Pre-defined target displacements are specified for the actuator to respond in displacement control. Loading occurs as the bridge specimen is pushed away from the structural wall. The specimen is unloaded and then reloading occurs such that the specimen is pulled toward the structural wall.

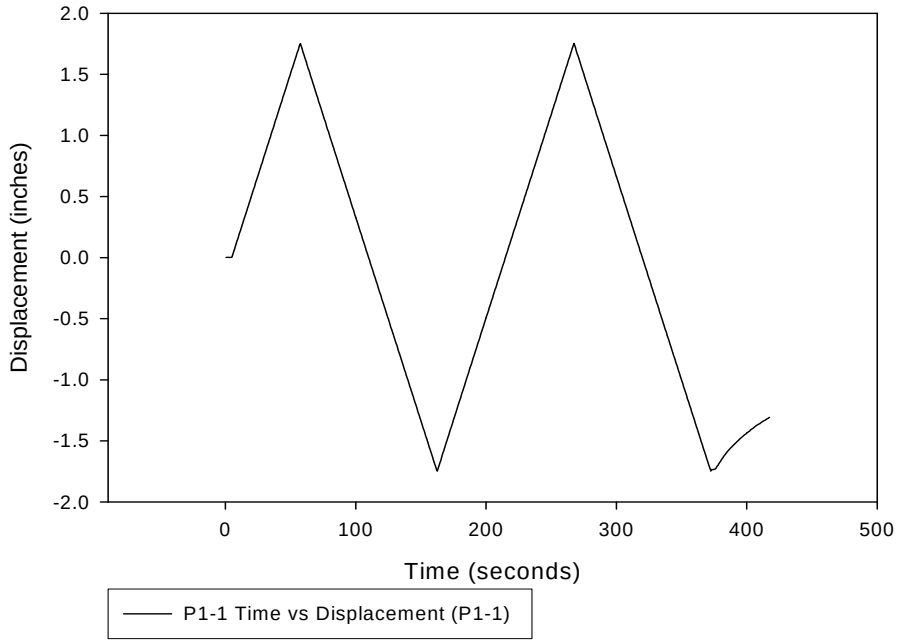

Figure 3.29: Typical loading protocol for test P1-1 at 1.75" (peak) displacement

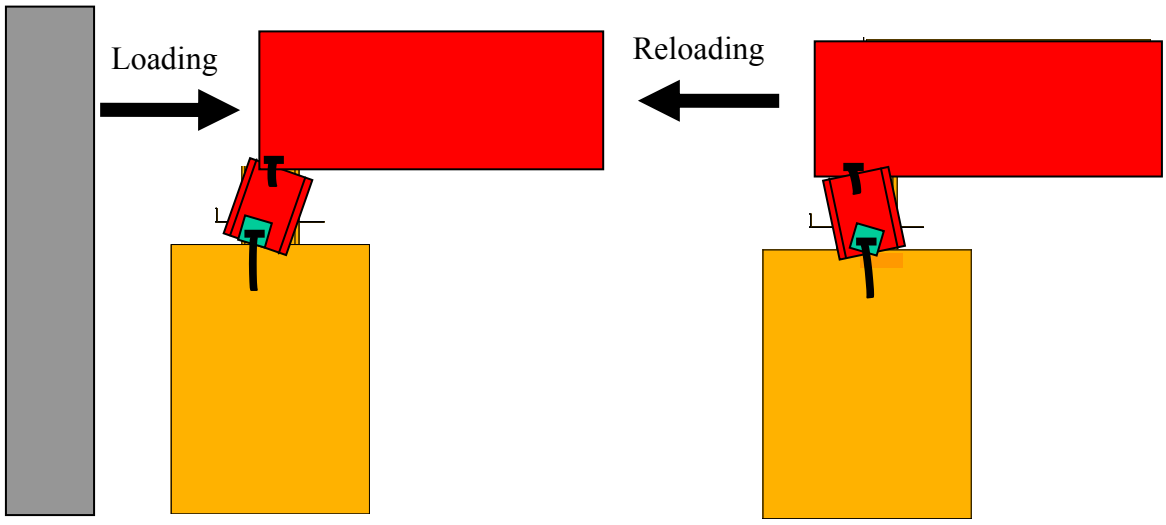

Figure 3.30: Loading and unloading schematic of full-scale tests on 40' bridge specimen

CHAPTER 4

EXPERIMENTAL TEST RESULTS

4.1 Summary

Evaluation of the performance of the steel pedestals is primarily based on the *force-displacement relationships*, *rigid body kinematics*, and *deformation modes* revealed by testing. The force-displacement relationships of the steel pedestals show the characteristic hysteretic behavior of the pedestals for each configuration. The hysteretic behavior of the steel pedestals is characterized by bolt slip, sliding of the pedestals on the ⅛" elastomeric (neoprene) pad, and prying-action of the swedged stainless steel anchor bolts as the pedestals rock about their center of rotation. The sliding and rocking phenomena observed during testing and captured by the instrumentation are a function of the rigid body kinematics that reveal the pedestals as very flexible elements. The deformation modes leading to potential failure mechanisms are identified, showing the performance of the anchor bolts as the critical parameter typically governing the peak response of the system. Several other factors, including the initial direction of loading (load path dependence), construction imperfections such as eccentricities, and friction within the system can affect and influence the force-displacement relationships. All six experimental tests provide insight to understanding the system performance of bridge steel pedestals. However, details from only a few of the tests are presented in this chapter to highlight the overall responses observed. Complete details about each test and its results can be found in the Appendices.

4.2 Response Assessment of Bridge Steel Pedestals

4.2.1 Force-displacement Hysteretic Relationships

The inherent hysteretic behavior of the steel pedestals is captured by the force-displacement relationships, which represent the system response of the 40' bridge specimen rehabilitated with a pair of steel pedestals. The peak displacements and loads from the force-displacement hysteretic relationships provide information on the strength and deformation capacity of the steel pedestals for each specimen. Table 4.1 summarizes the test specimen names for the configurations tested. Force-displacement hysteretic loops are recorded from all of the cycles at prescribed target displacements. In the plots of the force-displacement hysteretic loops, the positive (tensile) and negative (compressive) loads reflect whether the actuator is pulling (loading half-cycle) or pushing (reloading half-cycle) on the specimen. The peak displacement is defined as the corresponding displacement when the test is stopped due to the onset of a deformation mode that can lead to a failure mechanism.

Table 4.1: Nomenclature for six (6) test specimens

Loading Direction →	**Phase I (P1)**		**Phase II (P2)**	**Phase III (P3)**
Phase I: 19" pedestals *P1-1: W8x31 strong-axis loading* *P1-2: W8x31 weak-axis loading*	P1-1 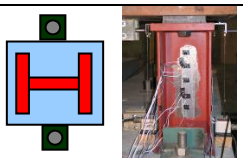	*Phases II & III - 33½" pedestals* *P2-1 & P2-2: strong-axis loading* *P3-1 & P3-2: weak-axis loading*	P2-1 	P3-1 
	P1-2 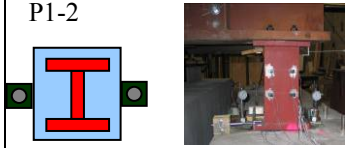		P2-2 	P3-2 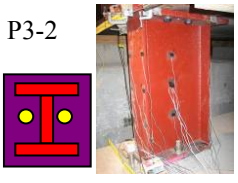

The peak displacement and peak loads obtained for each test are shown in Table 4.2. Test P1-2 shows the largest force resisted: 78.1 kips in tension and -96.4 kips in compression. Test P2-2 demonstrates the largest deformation capacity with a displacement of 3.5". Table 4.3 presents a comparison of the strength and stiffness at 0.5" and peak displacements. These results clearly show stiffness degradation with increased cycling. Test P1-2, when the pedestal is loaded about is weak-axis and the anchor bolts are positioned in the direction of loading, has the largest stiffness increase from its initial to peak cycle. Test P2-2, which experienced the largest deformation capacity at 3.5", has the most significant stiffness degradation (-71%) from 0.5" cycling to its peak cycling of 3.5". The configuration for test P2-2 shows the resiliency of the tall pedestals as being flexible elements capable of resisting large deformations. The position of the anchor bolts also influences the system response and dictates the allowable resistance before a deformation mode leading to a failure mechanism occurs.

Table 4.2: Summary of peak displacement and load from all tests

Test Specimen	**Peak Displacement (inches)**	**Peak Tensile/Compressive Loads (kips)**
P1-1	±1.75	28.2/-65.7
P1-2	±3.25	78.1/-96.4
P2-1	±1.4	36.8/-30.6
P2-2	±3.5	54.6/-61.3
P3-1	±2.0	53.0/-46.0
P3-2	±2.0	55.4/-53.4

Table 4.3: Comparison of strength and stiffness for all test data at 0.5" and peak displacements

Test Specimen	Δ (inches)	Load (kips)	Effective Stiffness (kips/in)	Stiffness degradation (%)
Short strong-axis (P1-1)	0.5"	13.9	37.2	-28%
	Peak @ 1.75"	28.2	26.8	
Short weak-axis (P1-2)	0.5"	15.8	35.8	-25%
	Peak @ 3.25"	78.1	26.9	
Tall strong-axis (P2-1)	0.5"	18.4	40.9	-41%
	Peak @ 1.4"	36.8	24.1	
Tall strong-axis (P2-2)	0.5"	24.6	54.1	-71%
	Peak @ 3.5"	54.6	16.5	
Tall strong-axis (P3-1)	0.5"	22.5	40.8	-39%
	Peak @ 2.0"	53.0	24.8	
Tall strong-axis (P3-2)	0.5"	23.0	49.5	-45%
	Peak @ 2.0"	55.4	27.4	

Each test begins with shakedown tests that are conducted at small displacements ranging from 0.1" to 0.3" displacements. The shakedown tests validate the linear, elastic region and verify accurate performance of the instrumentation used for data collection. The shakedown tests also help to eliminate any initial imperfections in the system, and conditions at the end of these runs are used as the zero points for all tests. The force-displacement relationships from the shakedown tests reveal the pedestals to respond in a linear, elastic fashion as seen in Figures 4.1 and 4.2 for test P1-1 and P2-2, respectively. However, at larger displacements, the response becomes nonlinear, signifying sliding and rocking. Energy is dissipated when the pedestals slide on the ⅛" elastomeric (neoprene) pad and the anchor bolts are engaged as a result of prying-action from the concrete.

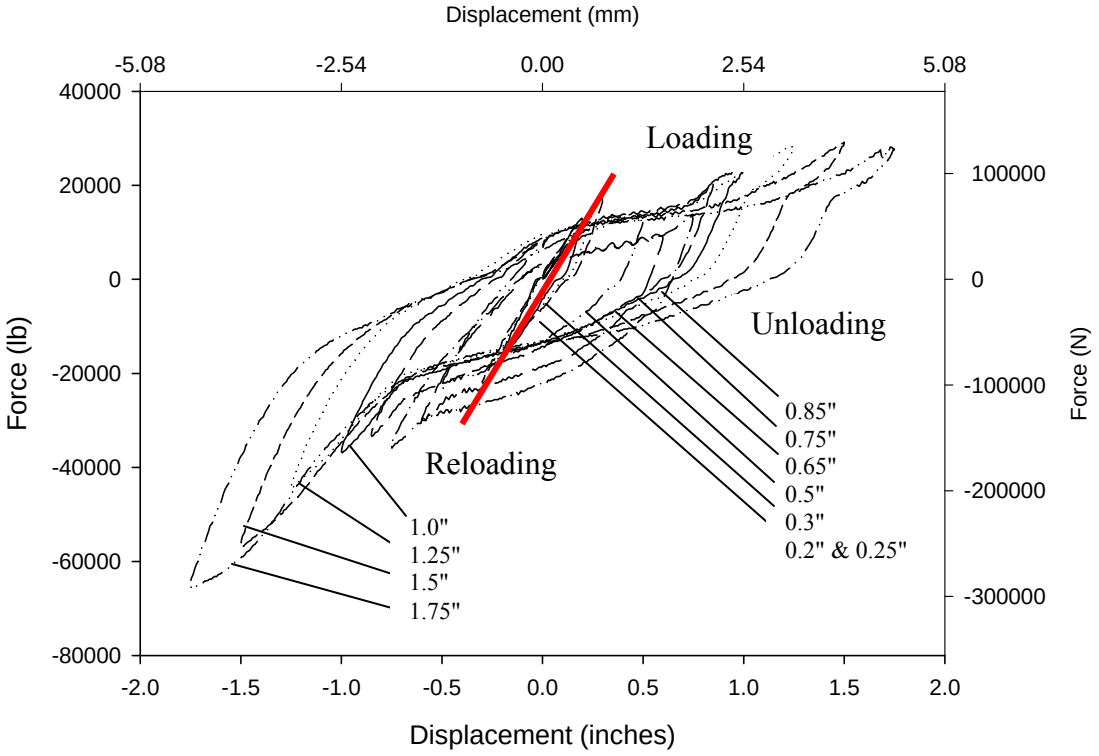

Figure 4.1: Force-displacement hysteretic relationship of all cycles for test P1-1, 19" pedestals with loading about its strong-axis

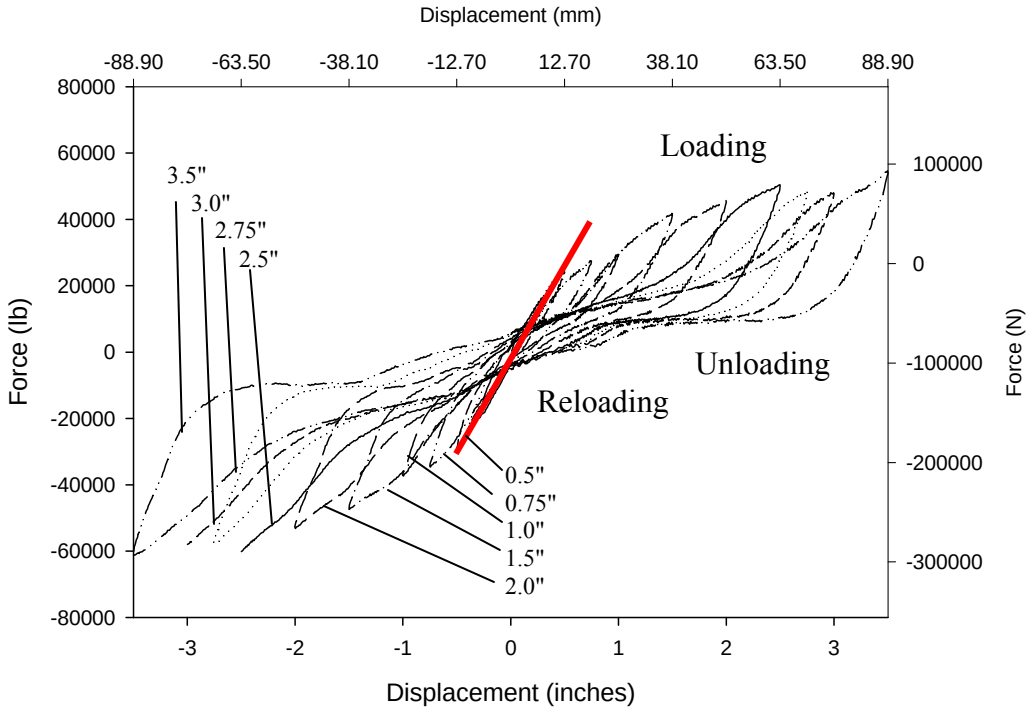

Figure 4.2: Force-displacement hysteretic relationship of all cycles for test P2-2, 33½" pedestals with loading about its strong-axis

Several response parameters are computed from the force-displacement hysteretic relationships to understand the effective stiffness (K_{eff}), energy dissipated (E_D), equivalent viscous damping (ζ_{eq}), and residual and relative displacements within the system response. These quantities are computed using Equations 4.1 through 4.3 at the first cycle of each target displacement and shown in Tables 4.4 and 4.5. From all six tests, the average peak effective stiffness was 24.4 kips/in for a set of two pedestals. While Tables 4.2 and 4.3 provide a side-by-side direct comparison of the experimental test results for all of the tests, test results from P1-1, P2-1, and P2-2 are compared in more detail in *Section 4.3*. Based on the amount of energy dissipated and equivalent viscous damping, the results for each pair of tests (see Table 4.4) are quite similar at the peak displacements despite the differences in the placement of the anchor bolts. The amount of energy dissipated is computed by calculating the area within the hysteresis curve and dividing it by the total area of an assumed rigid-plastic force-deformation behavior (rectangular area) shown in Figure 4.3. The percent of the energy dissipated is calculated by multiplying the ratio by 100 for the first cycle of each target displacement as shown in Eq. 4.2. The force-displacement hysteretic loops also reveal the rigid body kinematics observed during cycling, verified by the instrumentation, and explained in the next section.

$$K_{eff} = \frac{Force_{\max} - Force_{\min}}{\Delta_{@Force_{\max}} - \Delta_{@Force_{\min}}} \tag{4.1}$$

$$E_D(\%) = \frac{\int_{\Delta_{\min}}^{\Delta_{\max}} P(\delta)d\delta}{Area} 100\% \tag{4.2}$$

$$\zeta_{eq} = \frac{1}{4\pi}\frac{E_D}{E_{so}} \quad , \quad \text{where} \quad E_{so} = \frac{1}{2}k\Delta_{\max}{}^2 \tag{4.3}$$

and E_D = energy dissipated by damping (computed from area within hysteresis loop as shown in Eq. 4.2 without multiplying by 100%), E_{so} = maximum strain energy, k = effective stiffness, K_{eff}, computed in Equation 4.1, and Δ_{max} = target displacement (inches).

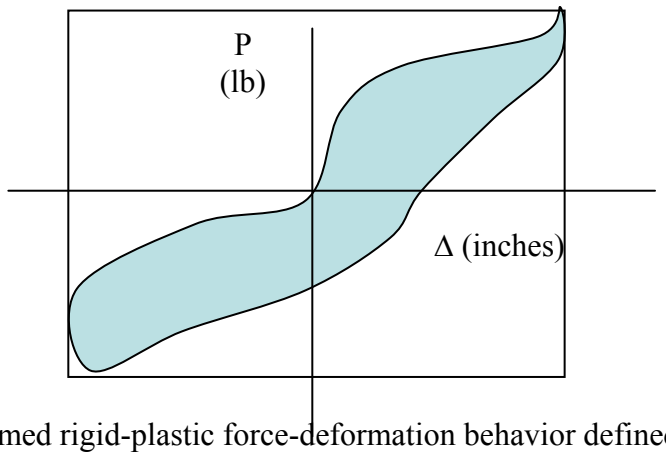

Figure 4.3: Assumed rigid-plastic force-deformation behavior defined by rectangular area cropping the hysteresis loop for calculating the amount of energy dissipated

Table 4.4: Summary of computed results for the effective stiffness (K_{eff}), energy dissipation (E_D), and equivalent viscous damping (ζ_{eq}) at peak displacements for a pair of pedestals

Test Specimen	Effective Stiffness at Peak Displacement (kips/in)	Energy Dissipation at Peak (%)	Equivalent Viscous Damping at Peak (%)
P1-1	26.8	18.7	11.9
P1-2	26.9	19.9	12.6
P2-1	24.1	12.4	7.9
P2-2	16.5	12.6	8.1
P3-1	24.8	22.6	14.4
P3-2	27.4	27.0	16.9

Table 4.5: Comparison of effective stiffness, K_{eff}, for all test data at the target displacements

Target Δ (inches)	P1-1 6-6-2005 150k actuator (strong-axis)	P1-2 6-11-2005 150k actuator (weak-axis)	P2-1 11-21-2005 150k actuator (strong-axis)	P2-2 12-7-2005 150k actuator (strong-axis)	P3-1 5-3-2006 85k actuator (weak-axis)	P3-2 5-5-2006 85k actuator (weak-axis)
0.2	73.5	-	-	-	-	-
0.4	-	-	-	57.5	-	-
0.5	37.2	35.8	40.9	54.1	40.8	49.5
0.75	33.1	28.7	-	41.5	37.3	46.0
0.8	-	-	32.7	-	-	-
1.0	30.4	25.76	-	33.3	34.1	41.8
1.4	-	-	**24.1**	-	-	-
1.5	28.7	26.0	-	29.7	28.8	33.5
1.75	**26.8**	-	-	-	-	30.4
2.0	-	27.7	-	24.7	**24.8**	**27.4**
2.5	-	28.1	-	22.1	-	-
2.75	-	28.1	-	19.4	-	-
3.0	-	28.4	-	17.7	-	-
3.25	-	**26.9**	-	-	-	-
3.5	-	-	-	**16.5**	-	-

Note: "-" indicates no data recorded at respective target displacement or because a deformation mode leading to a mode of failure occurred (peak displacements reached for each test is expressed in boldface)

Table 4.6: Comparison of amount of energy dissipated, E_D, for all test data at the target displacements

Target Δ (inches)	P1-1 19" short strong-axis	P1-2 19" short Weak-axis	P2-1 33½" tall strong-axis1	P2-2 33½" tall strong-axis2	P3-1 33½" tall weak-axis1	P3-2 33½" tall weak-axis2
0.2	14.8	-	-	-	-	-
0.4	-	-	-	9.6	-	-
0.5	35.1	23.2	14.9	9.4	12.2	7.3
0.75	33.6	26.3	-	12.8	11.9	9.0
0.8	-	-	11.6	-	-	-
1.0	24.0	26.0	-	7.4	10.9	20.8
1.4	-	-	**12.4**	-	-	-
1.5	18.6	20.6	-	12.0	16.1	17.4
1.75	**18.7**	-	-	-	-	19.5
2.0	-	19.9	-	11.7	**22.6**	**27.0**
2.5	-	16.2	-	17.9	-	-
2.75	-	18.6	-	10.9	-	-
3.0	-	18.7	-	16.6	-	-
3.25	-	**19.9**	-	-	-	-
3.5	-	-	-	**12.6**	-	-

Note: "-" indicates no data recorded at respective target displacement or because a deformation mode leading to a mode of failure occurred (peak displacements reached for each test is expressed in boldface)

Table 4.7: Comparison of equivalent viscous damping, ς_{eq}, for all test data at the target displacements

Target Δ (inches)	P1-1 19" short strong-axis	P1-2 19" short Weak-axis	P2-1 33½" tall strong-axis1	P2-2 33½" tall strong-axis2	P3-1 33½" tall weak-axis1	P3-2 33½" tall weak-axis2
0.2	9.4	-	-	-	-	-
0.4	-	-	-	6.2	-	-
0.5	22.4	14.8	9.5	6.0	7.8	4.6
0.75	21.4	16.7	-	8.2	7.6	5.7
0.8	-	-	7.4	-	-	-
1.0	15.3	16.6	-	4.7	6.9	13.2
1.4	-	-	**7.9**	-	-	-
1.5	4.9	13.1	-	7.6	10.3	11.1
1.75	**11.9**	-	-	-	-	12.4
2.0	-	12.7	-	7.5	**14.4**	**16.9**
2.5	-	10.3	-	11.4	-	-
2.75	-	11.8	-	6.9	-	-
3.0	-	11.8	-	10.6	-	-
3.25	-	**12.6**	-	-	-	-
3.5	-	-	-	**8.1**	-	-

Note: * = no data recorded at indicated target displacements or because a deformation mode leading to a mode of failure occurred (peak displacements reached for each test is expressed in boldface)

The displacement ductility of the steel pedestals can be quantified based on the value of the initial yield and peak displacements recorded from testing. The initial yield displacement defined for the pedestal tests is estimated to be the corresponding displacement value at which strain hardening is noted. The displacement ductility ratio, μ, is used as a comparative metric for assessing the potential seismic performance of the steel pedestals. The displacement ductility ratio is measured as the peak displacement divided by the initial yield displacement as revealed by the force-displacement relations. Table 4.6 shows the displacement ductility for each test, which ranges from 2.8 to 13. Displacement ductility ratios of 4 to 6 may be expected in extreme seismic events (Priestley, 1995). More details on the performance of the steel pedestals are discussed in *Chapter 5, Seismic Performance Assessment of Bridge Steel Pedestals*.

Table 4.8: Displacement ductility ratios for all six quasi-static, cyclic tests

Test Specimen	**Initial Yield Displacement (inches)**	**Peak Displacement (inches)**	**Displacement Ductility Ratio, μ_Δ**
P1-1	0.3	1.75	5.8
P1-2	0.25	3.25	13.0
P2-1	0.5	1.4	2.8
P2-2	0.3	3.5	11.7
P3-1	0.5	2.0	4.0
P3-2	0.5	2.0	4.0

4.2.2 Rigid Body Kinematics of Steel Pedestals

The steel pedestals undergo rigid body kinematics, where both sliding and rocking occur, during the cyclic testing (Figure 4.3). The steel pedestals dissipate more energy and begin to slide on the neoprene pad once the pedestals overcome the coefficient of friction at their base. Table 4.5, included in the previous section, shows the amount of energy dissipated at the first cycle of each target displacement for all six tests. The pedestals slide until the anchor bolts are engaged as the pedestals begin to rotate (or rock) about its rigid base plate, thereby causing prying-action of the anchor bolts. Figure 4.4 shows the rigid body kinematics. Sliding is typically noted when there is an increase in displacement with relatively little increase in force. At the peak displacements when the pedestal rocks as a result of prying of the anchor bolts from within the concrete, the pedestals are in double-curvature. Rocking is typically noted when there is a pinching of the hysteresis loop at the target displacement.

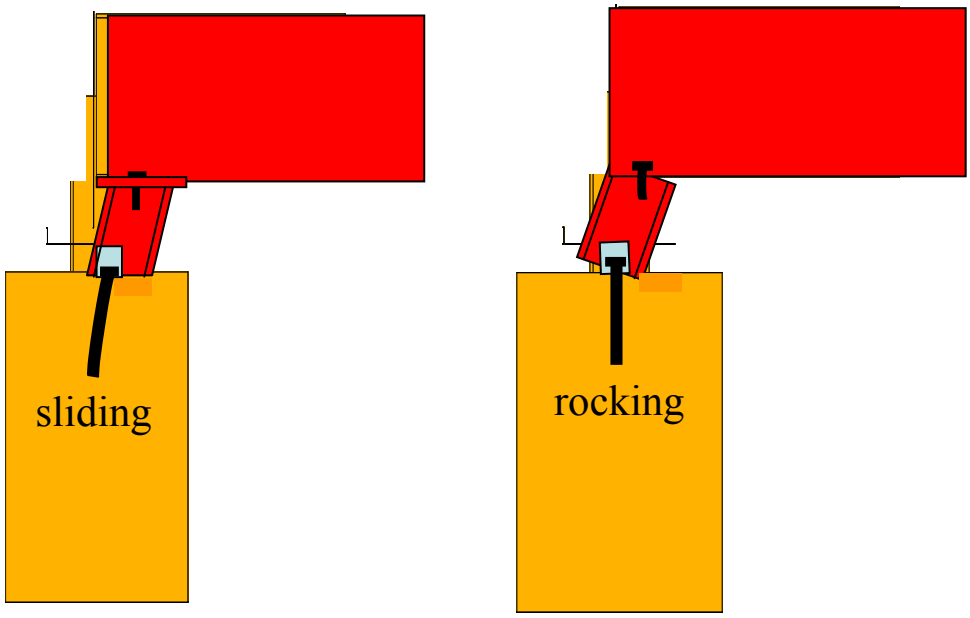

Figure 4.4: Rigid body kinematics observed during reversed, cyclic loading of pedestals

After the target displacement is reached, the specimen is unloaded and the pedestals return close to their original position before reloading and undergoing rigid body kinematics in the opposite loading direction. In some cases, the location of the center of rotation shifts from being at the neutral axis of the pedestal cross-section, resulting in unsymmetric bending. Consequently, unsymmetric loading is evident in the force-displacement hysteretic relationships. Test P1-1 shown in Figure 4.5 is an example of the unsymmetric loading as revealed by the force-displacement hysteretic relationship.

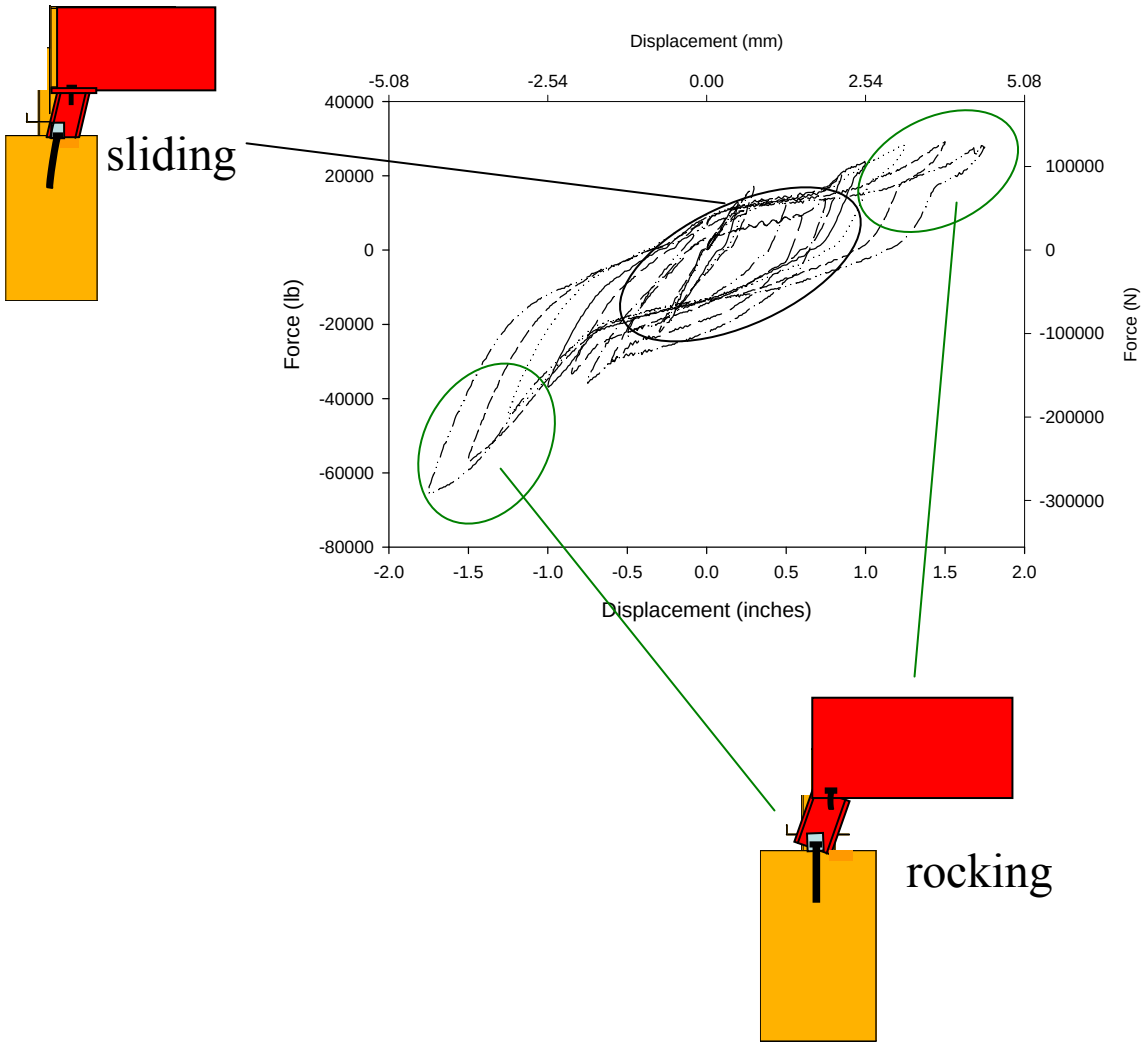

Figure 4.5: Rigid body kinematics indicated within force-displacement hysteretic relationship for test P1-1 (19" pedestals, strong-axis loading)

The rigid body kinematics of the system response are not only observed physically and indicated within the force-displacement hysteretic behavior, but also is captured by the instrumentation. LVDTs and string potentiometers are placed at various locations on the experimental test setup to quantify the displacements in the system. The displacements ideally show how the pedestal is behaving and in which direction displacements are measured. As mentioned in *Section 3.8* with respect to the system instrumentation, there are four LVDTs that measure the relative movement and any slip between members in the system between the following: 1) the girders and the dead load concrete block, Δ_1, 2) the underside of the girders and each pedestal, Δ_2, and 3) the pedestal and a fixed reference, Δ_3, and 4) the base of the pedestal sliding along the surface of reinforced concrete cap beam, Δ_4 as shown in Figure 4.5. Ideally, the relative movement of Δ_2 should essentially be zero, representing no slip between the girders and pedestals. Results show that Δ_3 almost equals the target displacement, Δ_1. However, as noted from the hysteretic relations, the pedestals are sliding on the concrete surface as reflected by the data captured by Δ_4. String potentiometers, Δ_5 and Δ_6, are also attached from the cap beams to the fixed reference to quantify any slip, if at all, between the two cast reinforced concrete piers. The angle of rotation of the pedestals is measured by string potentiometers that are attached from the pedestal top plate to the reinforced concrete cap beam. The string potentiometers are attached to wood blocks that are glued to the concrete surface. The string potentiometers are positioned parallel to the height of the pedestals. The angle of rotation is computed by taking the difference in the relative displacement measured by the southwest (SW) string potentiometer and southeast (SE) string potentiometer divided by the length as expressed in Equation 4.4. The

displacement measurements from the LVDTs and rotations of the pedestals from the data collected from the relative movement of the string potentiometers are presented in Tables 4.9 to 4.11. Results show the minimum and maximum readings captured to determine the displacement kinematics.

$$\theta(\text{deg}) = \frac{(SE - SW)}{L} * \frac{180}{\pi} \tag{4.4}$$

Table 4.9: Summary of minimum/maximum displacement kinematics from Phase I

Test specimen (duration)	Δ_1 (inches)	Load (kips)	Δ_3 Ped-Fixed (inches)	Δ_4 Sliding (inches)	Δ_2 Sgirder-Ped (inches)	Rotation (degrees)
P1-1	-1.75	-65.7	-1.6	-0.2	-.02	-0.4
(417.5 sec)	1.75	28.2	1.6	0.2	.02	0.1
P1-2	-3.25	-96.4	-3.0	-	-	-2.9
(694.5 sec)	3.25	78.1	2.3			5.4

Note: "-" indicates that no data was recorded; all numbers reported are rounded to the nearest tenth

Table 4.10: Summary of minimum/maximum displacement kinematics for Phase II

Test specimen (duration)	Δ_1 (inches)	Load (kips)	Δ_3 Ped-Fixed (inches)	Δ_4 Sliding (inches)	Δ_2 Sgirder-Ped (inches)	Rotation (degrees)
P2-1	-1.4	-30.6	-1.2	-0.2	0.0	-1.8
(455.5s)	1.4	36.8	1.4	0.1	0.0	2.0
P2-2	-3.5	-61.3	-1.7 (@ 2")	-0.1	0.6	-6.3
(1024.5s)	3.5	54.6	1.9 (@ 2")	0.0	-0.7	4.7

Note: "-" indicates that no data was recorded; all numbers reported are rounded to the nearest tenth

Table 4.11: Summary of minimum/maximum displacement kinematics for Phase III

Test specimen (duration)	Δ_1 (inches)	Load (kips)	Δ_3 Ped-Fixed (inches)	Δ_4 Sliding (inches)	Δ_2 Sgirder-Ped (inches)	Rotation (degrees)
P3-1	-2.0	-46.0	-1.5	-0.2	0.0	-2.3
(858.5s)	2.0	53.0	2.0	0.4	0.0	2.0
P3-2	-2.0	-53.4	-1.8	-0.1	0.0	-1.1
(2944s)	2.0	55.4	1.9	0.2	-0.1	0.9

Note: "-" indicates that no data was recorded; all numbers reported are rounded to the nearest tenth

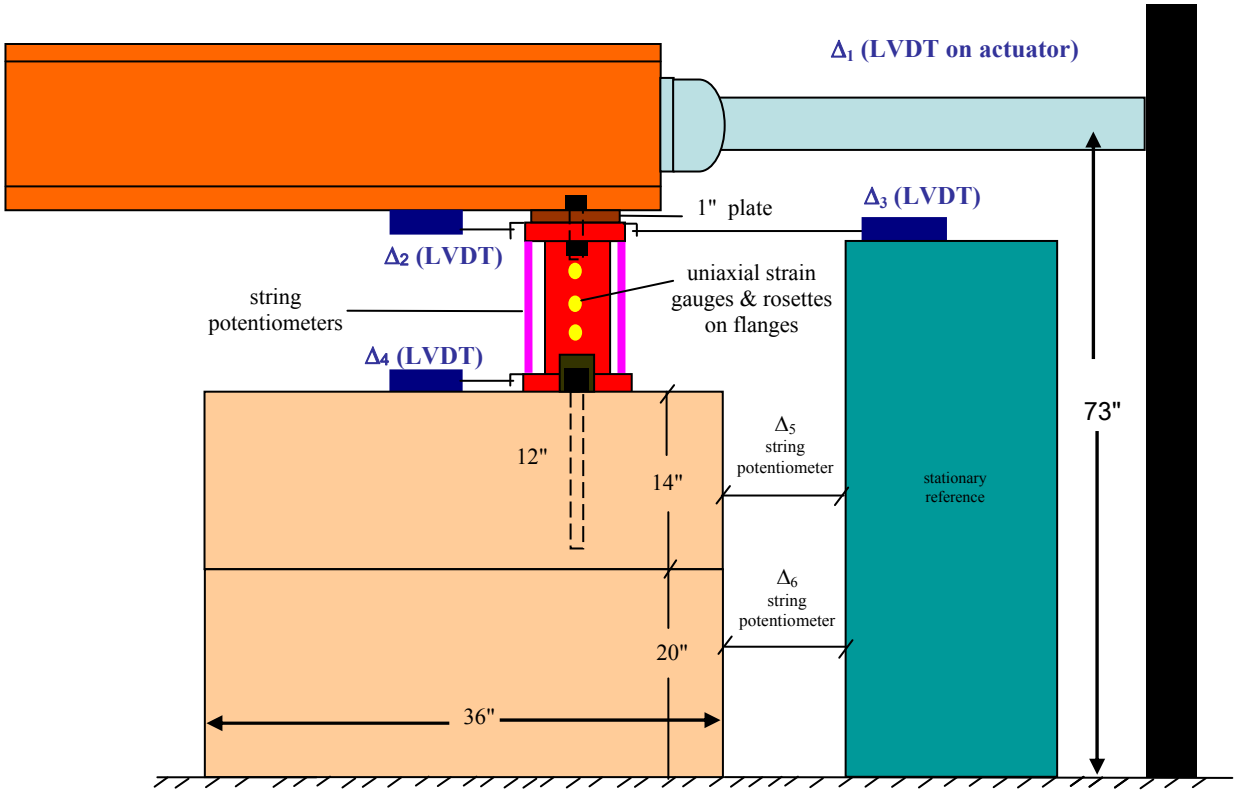

Figure 4.6: Schematic of instrumentation to determine the displacement kinematics

4.2.3 Deformation Modes

Experimental results indicate three major deformation modes that can lead to failure mechanisms for a 40' bridge simply-supported bridge span rehabilitated with steel pedestals:

i) prying-action of post-installed stud anchor bolts (predominant mode)

ii) bolts yielding

iii) concrete breakout (or concrete edge failure)

All three of these mechanisms are anticipated failure modes of anchors under shear loading as reported by the American Concrete Institute (ACI) Committee 318, Appendix D (2005), ACI Committee 355 (2004), and Eligehausen et al. (2006). Weld fracture was observed in test P2-1, resulting in two of the three mechanisms leading to modes of failure (bolts yielding and concrete breakout). This configuration, where the pedestals are relying heavily on the welds subjected to flexure from the cyclic loading, can be problematic in the event of an earthquake. Details of all the mechanisms leading to modes of failure for the post-installed stud anchor bolts for steel pedestals are described in this section.

4.2.3.1 Prying-action

Prying-action of the post-installed stud anchor bolts was the predominant mechanism observed in all of the tests, leading to surface failures (concrete breakout) or yielding of the bolts in certain cases. Prying-action, where a schematic drawing is shown in Figure 4.7, causes spalling or crushing of the surrounding concrete, thereby inducing bearing stresses in the concrete. As the surface concrete spalls or crushes, there is a shift of the centroid of resistance of the concrete breakout shear strength. It was observed that

with increasing loads, the stud elongates and the base plate rotates and loses contact with the concrete surface. As a result, a compression force between the base plate and concrete as well as a tensile force in the stud anchor bolt generate a moment. These forces can be translated into how the stud anchor bolt performs as a load-bearing mechanism.

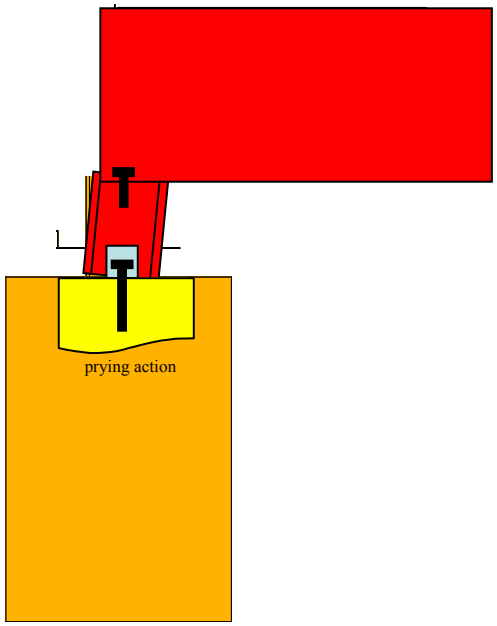

Figure 4.7: Prying-action of stainless steel stud anchor bolts causing spalling or crushing of surrounding concrete

The layout of the anchor bolts was selected in order to evaluate the performance of concrete edge distance, especially since close edge distances were observed in the field (Figure 4.8). Figure 4.9 shows the failure surfaces from tests P1-1 and P1-2 of the reinforced concrete cap beam subjected to shear loading close to an edge. The diagonal crack propagated through the depth of the 20" reinforced concrete cap beam as shown in Figure 4.10. Had the testing been continued, the concrete breakout strength would have

been exceeded. Tests revealed a failure surface angle of approximately 35° shown in Figure 4.11 and referenced in ACI 318-05, Appendix D and Eligehausen et al. (2006). Likewise in test P1-2, similar diagonal cracks create a failure surfaces that is also approximately 35° (Figure 4.12). This provides validation to the concern related to minimum concrete edge distances for the stud anchor bolts of steel pedestals. This concern is discussed in *Chapter 6 – Recommendations*. Figure 4.13 shows slip of the nut on the stud anchor bolt as a result of engaging the anchor bolt as the pedestal rocks as shown in Figure 4.14 for test P2-2. This prying-action of the anchor bolt is a phenomenon commonly observed in all of the tests, and therefore the predominant deformation mode for all of the six tests.

Figure 4.8: Existing GDOT bridge with pedestals close to edge of cap beam

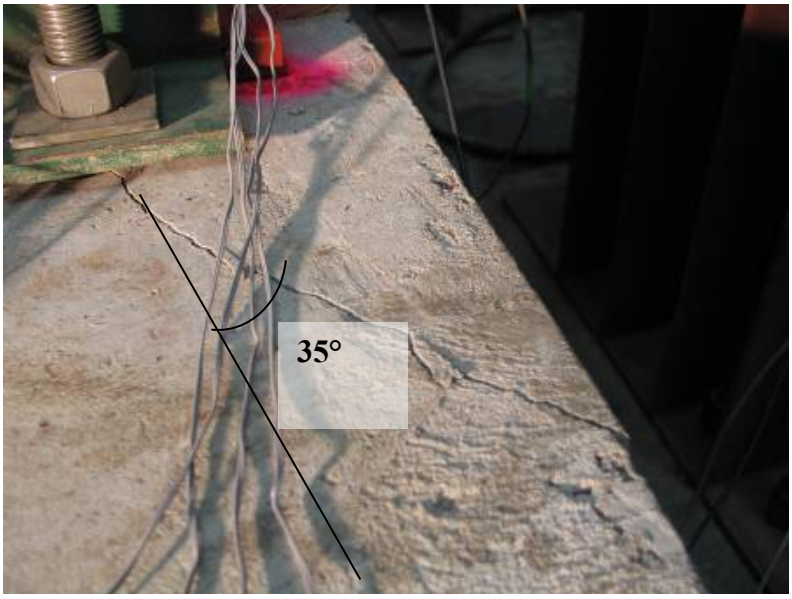

Figure 4.9: Failure surface of reinforced concrete cap beam subjected to shear loading with bolt close to edge during test P1-1

Figure 4.10: Diagonal crack propagated through the depth of the 20" reinforced concrete cap beam during test P1-1

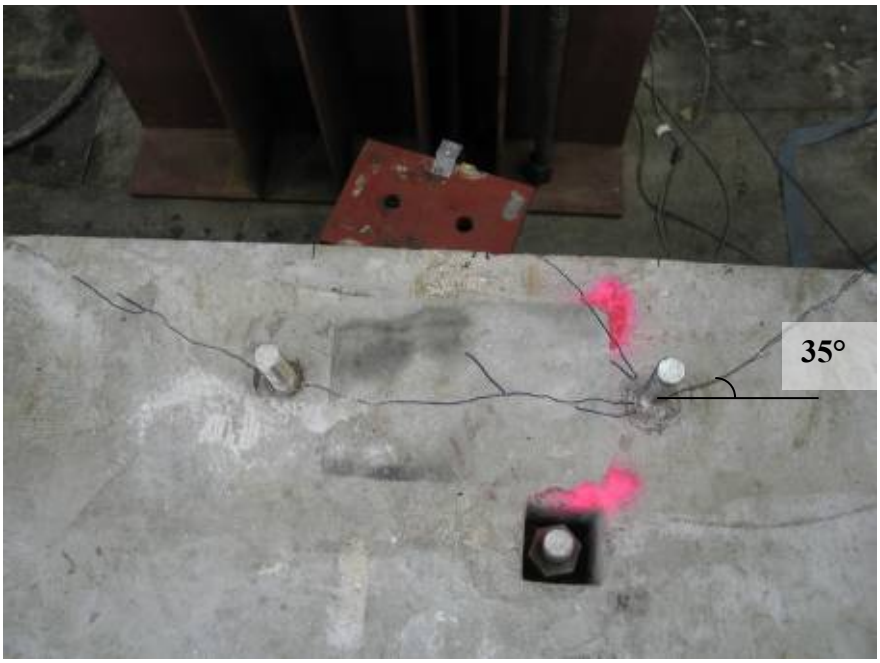

Figure 4.11: Failure surface angle of approximately 35° after test P1-1

Figure 4.12: Failure surface angle of approximately 35° after test P1-2

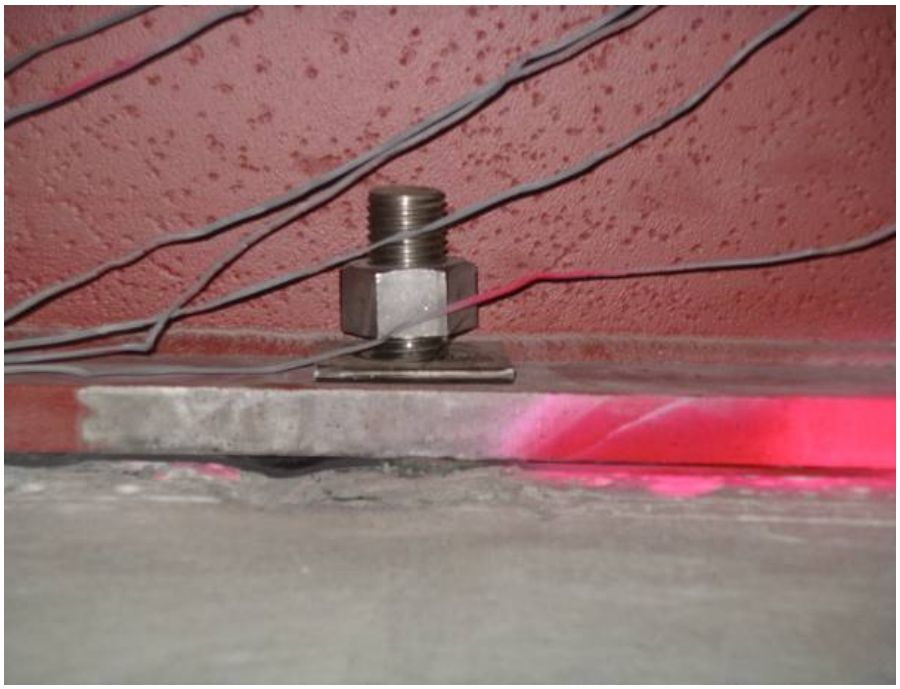

Figure 4.13: Slip of nut on stainless steel stud anchor bolt as a result of prying-action as the pedestal rocks

Figure 4.14: 33½" pedestal rocking and engaging prying-action of stainless steel anchor bolt

4.2.3.2 Bolts yielding

The second mechanism observed was yielding of the post-installed stud anchor bolts. Yielding occurred at relatively large displacements and loads. Figure 4.15 shows a schematic of yielding of the bolts and the actual yielding observed in test P1-2, where peak loads were 78 kips (tensile loading) and -96 kips (compressive loading) and peak displacements were 3.25". Sufficient resistance was provided by the anchor bolts because there was adequate embedment length of the bolts into the concrete pier and adequate concrete edge distance such that concrete breakout did not occur. Consequently, yielding of the bolts allowed for greater strength and deformation capacity within test P1-2. Additional factors that can affect this mechanism are the anchor bolt strength, diameter of anchor bolt, concrete strength and anchor bolt spacing. Mechanical dial gauges were connected to measure uplift (pullout) of the bolts. For all of the tests, the maximum pullout was 0.2". Testing was stopped at the onset of noticing yielding of the bolts such that a catastrophic failure did not result with continued loading.

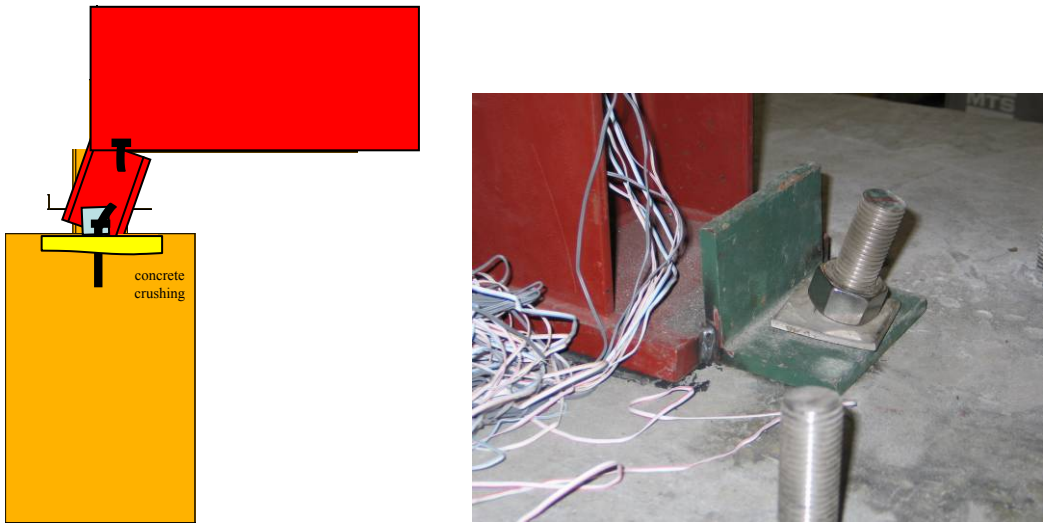

Figure 4.15: Schematic (left) and photo of bolt yielding (right) during test P1-2

4.2.3.3 Concrete breakout

The third mechanism that can lead to a mode of failure is concrete breakout, also called concrete edge failure. Concrete breakout occurs when the concrete fractures before the load-carrying capacity of the steel is reached. Figure 4.15 shows a side-view schematic of the surface failure, where the surface failure on top of the concrete pier occurs at an angle of 35° (Figure 4.16). For test P2-1, the tall pedestal was loaded along the plane of the strong-axis of the steel pedestal. The angle was welded to the base plate in the direction of loading such that the weld that connects that angle to the pedestal base plate was in flexure during cyclic loading. The weld fractured due to low cycle fatigue such that the L-shaped angle separated from the base plate of the pedestal, thereby disengaging the anchor bolt from the pedestal. However, due to sliding of the pedestal, the base plate of the pedestal reconnected to the weld and reactivated the resistance of the anchor bolt based on frictional contact alone. When the load in the system exceeded the allowable resistance provided by frictional contact with the weld, concrete breakout resulted and testing was stopped. The concrete breakout essentially consisted of unconfined concrete as a result of the anchor bolt being close to the edge of the concrete pier. The surface failure occurred at the predicted angle of 35° for test P2-1. Since limited resistance was provided by this anchor bolt configuration and connectivity, the peak displacement was 1.4" and peak tensile and compressive loads were 36 kips and -30 kips, respectively, for test P2-1.

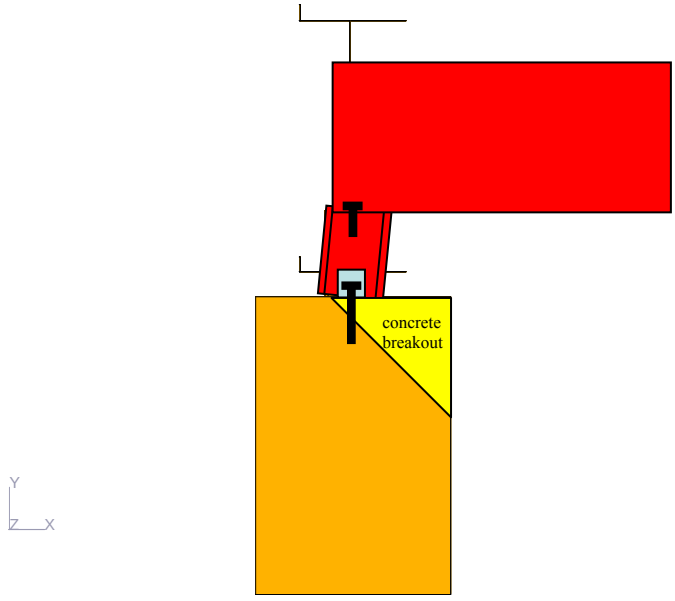

Figure 4.16: Side-view schematic of concrete breakout for anchors close to the edge of the reinforced concrete cap beam

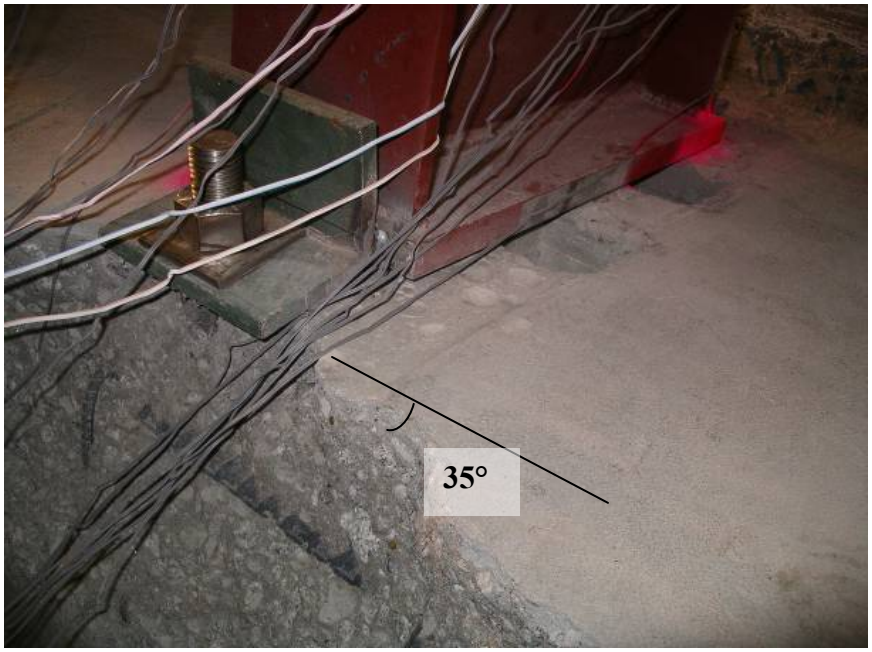

Figure 4.17: Concrete breakout at approximately 35° on reinforced concrete cap beam

4.3 Comparison of Short and Tall Pedestal Tests: P1-1, P2-1, and P2-2

Although six tests were conducted, tests comparing the short (P1-1) and tall (P2-1 and P2-2) pedestals along its strong-axis of bending (longitudinal loading) are compared in depth. At 0.5" cycling, test P2-2 revealed to be the stiffest among the three tests, with its anchor bolts positioned within the cross-section and at the center of rotation, rigidity and mass of the steel pedestals (Table 4.12). Test P1-1 showed the smallest amount of effective stiffness as the setup allowed for more sliding of the 19" short pedestal to occur between the pedestal base and neoprene pad that rested on the reinforced concrete cap beam. With the increase in sliding in test P1-1, more energy is dissipated. Therefore, sliding of the pedestals along its base enabled more energy to be dissipated and larger amounts of equivalent viscous damping to be quantified as noted in test P1-1. The equivalent viscous damping of the steel pedestal compares favorably to traditional energy dissipating devices with damping ratios. Prying-action of the anchor bolts in test P1-1 led to cracking of the concrete cap beam that resulted in a surface failure (Figure 4.8) at approximately 35° as predicted by ACI, Appendix D (2005) and Eligehausen et al. (2006).

Table 4.12: Comparison of tests P1-1, P2-1, and P2-2

Test Specimen	Effective Stiffness at 0.5" Cycling (kip/in)	Energy Dissipation at 0.5" (%)	Equivalent Viscous Damping at 0.5" (%)
P1-1	37.2	35.1	22.4
P2-1	40.9	14.9	9.5
P2-2	57.5	9.4	6.0

For test P2-1, the angle was welded to the base plate of the 33½" tall pedestal in the direction of loading such that the weld that connects that angle to the pedestal base plate was in flexure during cyclic loading. Weld fracture occurred from low cycle fatigue. The fracture disengaged the anchor bolt to the pedestal. However, due to sliding of the pedestal, the base plate of the pedestal reconnected to the weld and reactivated the resistance of the anchor bolt based on frictional contact alone. When the load in the system exceeded the allowable resistance provided by frictional contact with the weld, concrete breakout resulted and testing was stopped. The concrete breakout essentially consisted of unconfined concrete as a result of the anchor bolt being close to the edge of the concrete pier. The surface failure occurred at the predicted angle of 35° for test P2-1 (Figure 4.16). Since limited resistance was provided by this anchor bolt configuration and connectivity, the peak displacement was 1.4" and peak tensile and compressive loads were 36 kips and -30 kips, respectively, for test P2-1.

However, test P2-2 did not dissipate as much energy as the other two specimens, P1-1 and P2-1. The connectivity for test P2-2 with the bolts within the cross-section prevented significant sliding from occurring such that the anchor bolts were engaged throughout the loading cycle. The forces resisted by the bolts can be translated into how the stud anchor bolts perform as a load-bearing mechanism. The low amount of energy dissipated of 9.4% is also evidence of this observation. At the peak displacements, test P2-2 doubled the deformation capacity and tensile strength capacity of test P1-1. Test P2-2 revealed the flexibility of the steel pedestals when anchored at its center of rigidity.

CHAPTER 5

SEISMIC PERFORMANCE ASSESSMENT OF BRIDGE STEEL PEDESTALS

5.1 Summary

The force-displacement hysteretic relationships obtained from experimental testing are used to calibrate an analytical bridge model to assess the seismic performance of steel pedestals with varying heights and orientations. Experimental tests results have provided realistic data to represent the hysteretic behavior of the pedestals, which may govern the response of the system. The CSUS, in particular, has the potential for large, events per paleoseismic studies of the New Madrid Seismic Zone (NMSZ) and the Charleston (South Carolina) Seismic Zone (UMKC, 2002). Although the seismic hazard in the Western United States (WUS) is greater than in terms of the frequency of events, parts of the CSUS can have ground motions with similar intensities as that of the WUS.

To analytically assess the seismic performance of the bridge steel pedestals, a seismic hazard analysis is conducted to evaluate the displacement demands of a candidate bridge idealized as a one-dimensional, three-degree-of-freedom (3DOF) structure using uniform hazard response spectra and nonlinear time history analyses. The time history analyses of the 3DOF structure are used to evaluate the displacement demands of the steel pedestals subjected to low-to-moderate synthetic ground motions developed by Fernandez and Rix (2006). These ground motions account for geological effects such as deep profiles of unconsolidated sediments that have significant influence on the maximum acceleration response. A suite of ground motions are used to assess how varying levels of acceleration, frequency content of ground motions, and pedestal heights

and orientations tested affect the response of a linear model with inelastic behavior defined for the steel pedestals. The results of the analyses are useful in synthesizing recommendations for the best practices for the design and installation of steel pedestals to GDOT and other states interested in adopting the use of steel pedestals.

5.2 Seismicity in the CSUS

One source that is capable of producing strong ground motions is the New Madrid Seismic Zone (NMSZ), located at the intersection of southern Illinois, southeastern Missouri, and northwestern Tennessee. Past geological evidence has shown that there have been at least six (possibly nine) earthquakes centered around New Madrid from 1811-1812 with moment magnitudes greater than $M_w = 7$ including two events with moment magnitude of approximately $M_w = 8$ (Johnson and Schweig 1996). These events were two of the largest earthquakes recorded in the continental United States. Survivors reported open cracks in the earth's surface and the ground rolling in visible waves. Because the NMSZ was sparsely populated at this time, little damage was noted. More densely populated now, the NMSZ has potential for significant losses (e.g. economic and casualties) due to the known potential for large earthquakes, and the lack of seismic detailing of the built environment in the region.

The continental crust in the CSUS does not attenuate seismic waves as rapidly as younger crust in the WUS, hence, the seismic waves from a large magnitude earthquake from the NMSZ would be felt throughout a wider area of the CSUS as compared with a similar magnitude earthquake in the WUS (Long 2005) as shown in Figure 5.1. Missouri alone could anticipate losses of at least $6 billion from such an event (Southeast Missouri

State University 2002). Inclusive of the CSUS is the state of Georgia, which is within an area of low-to-moderate seismic risk. The peak ground acceleration for the central and south eastern United States for 2% probability of exceedance in 50 years is shown in Figure 5.2 (USGS 2002). Parts of north Georgia would expect peak ground accelerations exceeding 0.09g and 0.40g for the 475-year and 2475-year design earthquake based on the USGS (2002) hazard maps.

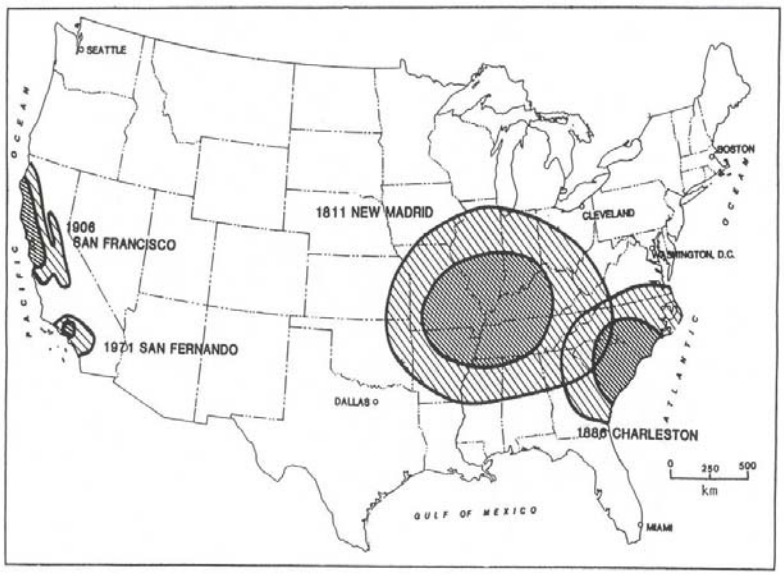

The dark areas: MMI VIII
The light areas: MMI VI-VII

Figure 5.1: Larger areas affected in the central and southeastern U.S. than in the Western U.S. based on the Modified Mercalli Intensity (MMI) of large past earthquake activity in the U.S.

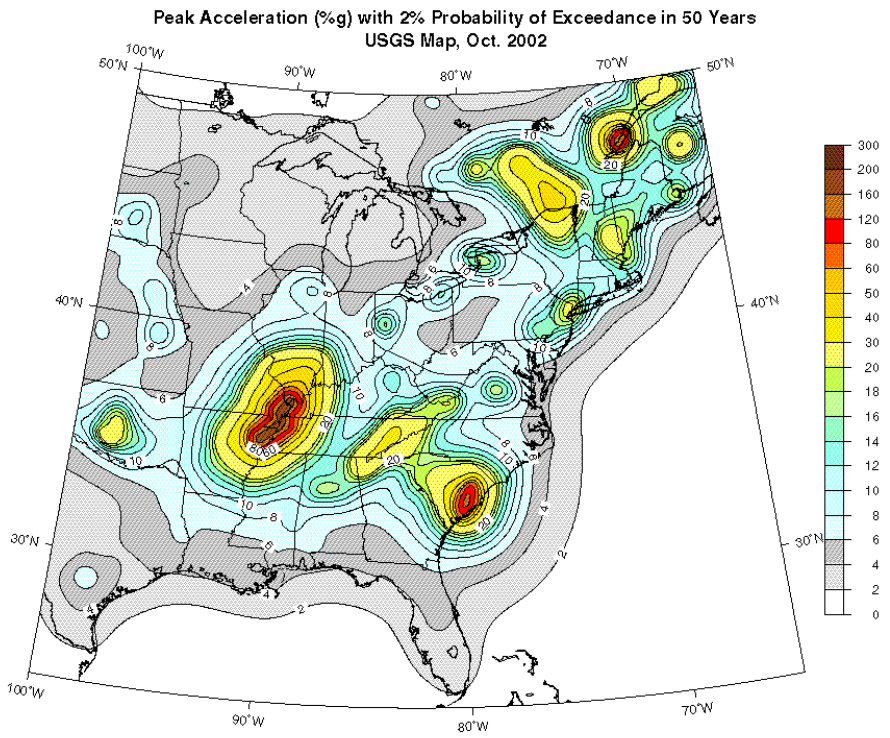

Figure 5.2: USGS (2002) national seismic hazard map for conterminous U.S.

Figure 5.3 shows a map of Georgia and the location of all earthquakes that are known to have occurred within 25 km (15 miles) of Georgia in the past 100 years, while Figure 5.4 shows the seismic design map used for the Georgia Department of Transportation (GDOT). For seismic design in Georgia, bridges are designed for Seismic Category A except for bridges in the part of Georgia where the Acceleration Coefficient is greater than 0.09 and where bridges shall be designed for Seismic Category B, according to GDOT (2005). However, the 4 counties (Catoosa, Dade, Walker, and Chattooga highlighted in Figure 5.4) omitted can expect spectral accelerations of almost 0.3g for the 2475-year return period earthquake. Consequently, bridges designed in these

counties should be considered for at least for Seismic Category B. More details about design recommendation are presented in *Chapter 6, Recommendations.*

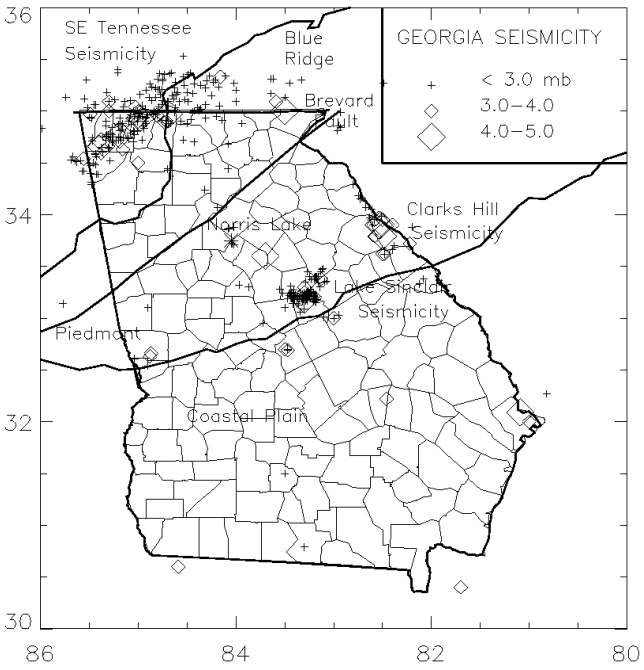

Figure 5.3: Past seismic activity in Georgia

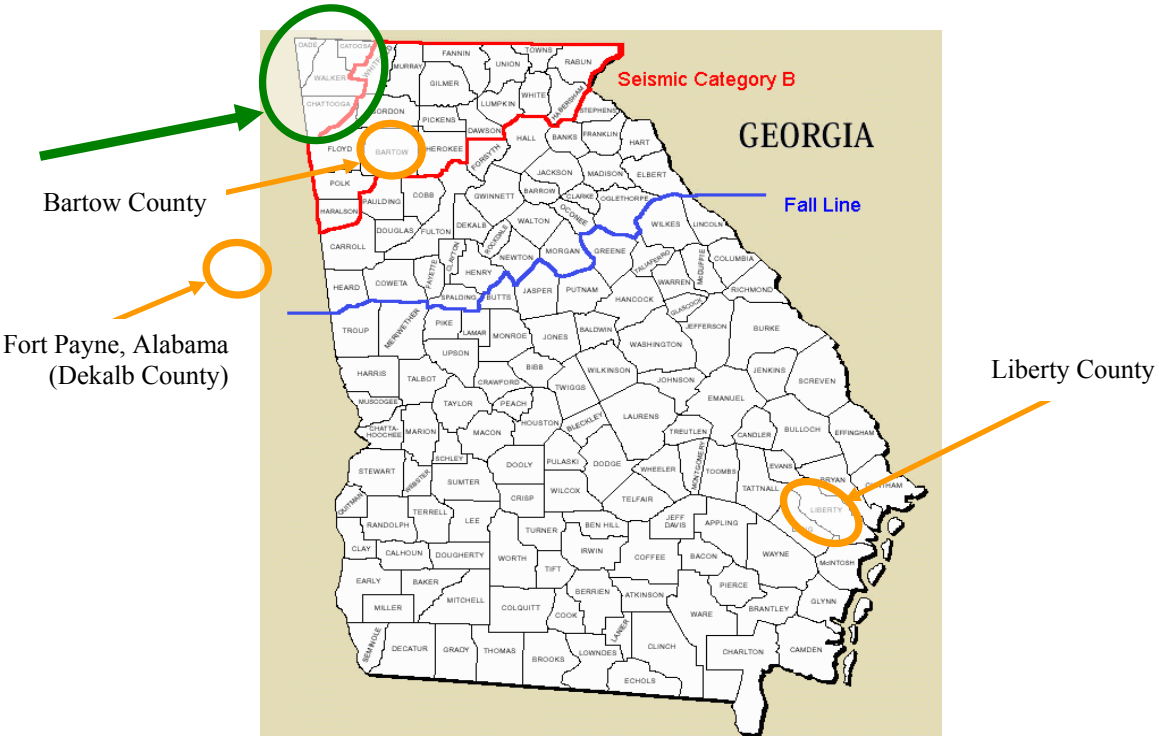

Figure 5.4: Seismic design map for GDOT (2005)

5.3 Analytical Model Development of Candidate Bridge

To assess the seismic performance of a multi-span continuous bridge rehabilitated with steel pedestals, a three-degree-of-freedom (3DOF) bridge model is developed in OpenSees to determine the expected elastic displacements. While a more detailed model can be developed, the 3DOF bridge model can represent the bridge response and can justifiably provide:

1) a means to simply evaluate the elastic displacement and assess the vulnerability of existing bridges rehabilitated with steel pedestals,
2) the ability to model the nonlinear behavior of the steel pedestals as the majority of the deformation is expected to occur in the pedestals with the deck remaining primarily elastic, and
3) the ability to model the columns as elastic members since preliminary analyses for low seismic loads do not show nonlinear behavior in the columns (column drifts are less than 0.3%.

The bridge model is an upright cantilever beam, and is based on GDOT Bridge No. 72 located on Sandy Run Road over I-95 in Liberty County, Georgia with the following details:

- The total bridge length is 410 feet, and the superstructure is supported on bents with reused bearings that are attached to the steel pedestals. (A schematic drawing of the bridge is shown in Figure 5.5).
- The bridge is elevated with 19" steel pedestals for a nominal vertical clearance height of 17 feet. Pedestal details are mentioned in *Section 2.2.*

- The cross-section of the bridge consists of four girders and a total width of 28.3' (Figure 5.6). The depth of the concrete deck is 7". At each bent, there is a reinforced concrete cap beam with reinforced square columns.

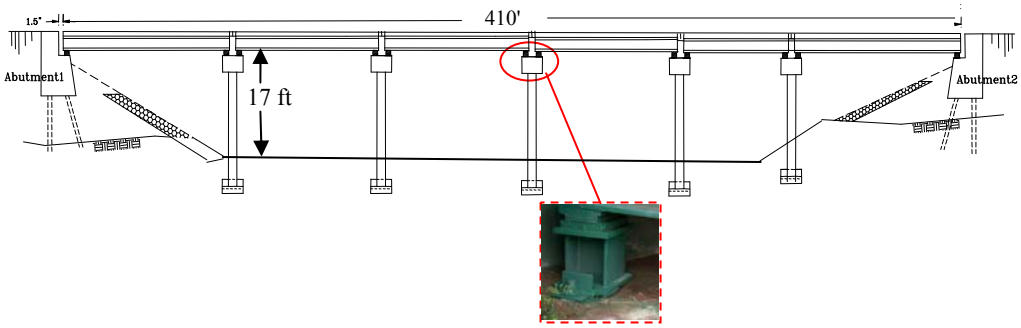

Figure 5.5: Schematic of GDOT Bridge No. 72 in Liberty County, Georgia

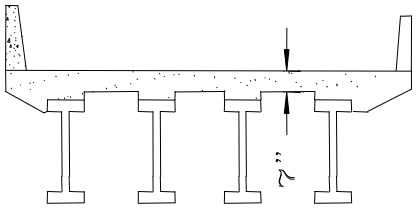

Figure 5.6: Cross-section of bridge showing four girders located at 9' on center

The candidate bridge is idealized into a 3DOF bridge model that resembles an upright cantilever beam, where the superstructure is represented as a lumped mass and the substructure (pedestals and columns) represent the upright cantilever beam. The modeling details for the upright cantilever beam are presented next.

5.3.1 Superstructure

The superstructure of the candidate bridge is comprised of the girders and deck, which operate in composite action. Since the composite deck is very stiff and behaves as a rigid element under lateral loads, the deck is simply represented by a lumped mass of 4 k-s^2/in. The mass of the superstructure is determined based on the density of concrete (deck and parapets) and all the steel members for the selected candidate bridge.

5.3.2 Substructure

The 3' square columns are modeled as elastic members using force beam-column elements. A clearance height of 17' is specified for both pedestals such that the column length is 15.4' and 14.2' for the 19" and 33½" pedestals, respectively. The stiffness for the two-column bents is summed to give an effective stiffness for the upright cantilever beam. The properties for moment of inertia of one bent is computed and multiplied by the total number of columns. A cracked gross-section reduction of 0.7 is then multiplied by the effective moment of inertia to account for cracking. The modulus of elasticity, E, for the concrete is 3372 ksi per a compressive strength of 3.5 ksi specified in the bridge plans. For this analysis, the footings are considered as rigid supports and are modeled with "fixed" support conditions.

5.3.3 Steel Pedestals

The upright cantilever beam also consists of the pedestals that are in series with the columns. The top of the column is modeled as "fixed" to the base joint of the pedestal where the sliding and rocking are captured by the hysteretic relationships defined for a translational spring. An effective stiffness of all of the pedestals is determined from the summation of all the pedestals along the length of the bridge. Depending on the pedestal being defined from the six tests, the pedestal section properties such as moment of inertia and area are specified uniquely for the pedestal element within the 3DOF bridge model. The modulus of elasticity for the steel material is assumed to be 29,000 ksi and the yield strength of 50 ksi is also specified. The length of the pedestal element is defined for both the 19" and 33½" pedestals to provide a 17' nominal length of the pedestal and column in series.

The force-displacement hysteretic relationships obtained from experimental test results are used to define a hysteretic material that is modeled in parallel with the steel material of the pedestal for composite behavior. The parallel material is assigned to a zero-length spring element that only translates in the longitudinal direction of the bridge. The zero-length spring is attached between the top of the pedestal node and deck node, which are coincident nodes. The zero-length spring records the relative displacement between the deck and top of the pedestal when subjected to various ground motions. The mass of the deck is defined at the deck represented by node 2, and the top of the pedestal is node 3. A mass of 1 kip is also defined at the top of the columns, node 5, to represent the summation of mass of the bent caps and columns. The hysteretic material is defined for two displacements, 0.5" and peak, which create the loading, unloading, and reloading

for the hysteresis of the spring element. The stiffness of all the pedestals is used to define the hysteretic material from the values of the effective stiffness at 0.5" and the peak displacement that are multiplied by the total number of pedestals along the bents. Table 5.1 shows the values noted for a pedestal. The total stiffness of the 3DOF bridge model is taken as a system of springs in series ($K_{pedestals}$, $K_{columns}$, and $K_{springs}$), as shown in Figure 5.7 and computed by Equations 5.1 and 5.2, where the peak effective stiffness of the pedestals, $K_{springs}$, is applied and governs the overall structural stiffness.

Table 5.1: Initial effective stiffness values at 0.5" and peak displacement from force-displacement hysteretic relationships

Test Specimen: Pedestal Height	**Initial Effective Stiffness of Pedestal**	**Peak Effective Stiffness of Pedestal, $K_{springs}$**
P1-1: 19"	18.6	**13.4**
P1-2: 19"	17.9	**13.5**
P2-1: 33½"	20.5	**12.1**
P2-2: 33½"	27.1	**8.27**
P3-1: 33½"	20.4	**24.8**
P3-2: 33½"	24.8	**13.7**

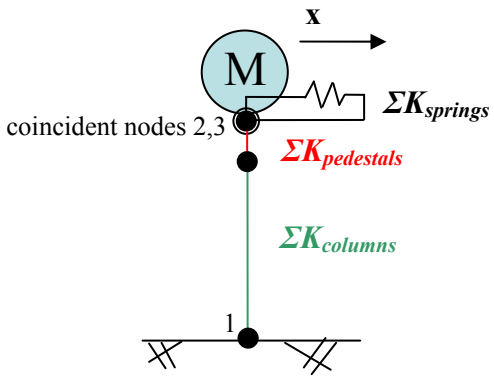

Figure 5.7: Idealization of 3DOF members in series

$$\sum K_t = \frac{K_{pedestals} K_{columns}}{K_{pedestals} + K_{columns}} \tag{5.1}$$

$$\sum K_{total} = \frac{K_t K_{springs}}{K_t + K_{springs}} \tag{5.2}$$

5.4 Analyses Using 3DOF Bridge Model

5.4.1 Eigenvalue Analysis

An eigenvalue analysis is conducted on the 3DOF bridge model based on the inherent properties, stiffness and mass, of the system for determining the structural period. The bridge model is amended to include the length of the pedestal (19" or 33½") and the hysteretic behavior obtained from experimental testing. The initial stiffness of the hysteretic material for the pedestal zero-length spring element corresponds to the initial stiffness of this element for the eigenvalue analysis. However, at larger amplitudes of motions, the structural period is undefined for an inelastic element for the system herein. Only tests P1-1, P1-2, P2-1, and P2-2 are used for analyses to provide a basis for comparison. Equations 5.3 and 5.4 show how the structural frequency and period are computed for the 3DOF bridge model. Table 5.2 presents the range for the structural periods that are used to select the peak acceleration values from the uniform hazard response spectra in *Section 5.4.3*.

$$\omega_n = \frac{2\pi}{T_n} \tag{5.3}$$

$$T_n = 2\pi\sqrt{\frac{m}{\sum K}} \tag{5.4}$$

Table 5.2: Range of structural periods as determined from an eigenvalue analysis of the 3DOF bridge model from 4 of 6 experimental test specimens modeled

Test Specimen: Pedestal Height	**Initial Effective Stiffness of a Pedestal, $K_{springs}$**	**Structural Period, T_n (seconds)**
P1-1: 19"	18.6	0.606
P1-2: 19"	17.9	0.774
P2-1: 33½"	20.5	0.574
P2-2: 33½"	24.8	0.527

For the eigenvalue analyses, all properties remained constant except for the pedestal cumulative stiffness, orientations (strong-axis/weak-axis), heights and therefore column lengths. Comparing the 19" pedestals to the 33½" pedestals, the 3DOF bridge model is quite sensitive to the change in stiffness as governed by the pedestal stiffness. Based on Equation 5.4, it is evident that with a slight decrease or increase in initial stiffness of the hysteretic behavior, the total stiffness changes. Consequently, the structural period changes. This 3DOF bridge model shows the stiffness of the pedestals to be the most flexible (smaller stiffness value) element within the system, thereby controlling the response of the system. Recommendations addressing inadequate seat widths due to large displacement demands as determined by the analyses are presented in *Chapter 6 – Recommendations*.

5.4.2 Nonlinear Time History Analyses (NTHA)

Nonlinear time history analyses (NTHA) are performed on the 3DOF bridge model developed in OpenSees for the undamped case to determine peak displacements of the bridge deck and inelastic spring deformations when subjected to a suite of ground motions. (Acceleration values for the suite of ground motions used for the analyses are presented in the Appendices). From the time histories, response spectra are generated in OpenSees for each ground motion at 2%, 5% and 10% damping. The effective stiffness of the 3DOF bridge model is calculated to determine the effective structural period and therefore the accelerations produced by the response spectra discussed in *Section 5.4.2.2*. These displacements represent the expected elastic displacements in the deck. The inelastic displacement demands from the spring element, which represent the

deformations of all the pedestals idealized for this candidate bridge, are also evaluated from the nonlinear time history analyses and reported in *Section 5.4.2.3*. The elastic displacements from the response spectra generated from the site specific time histories are later compared in *Section 5.4.4* to the elastic displacements computed from the uniform hazard response spectra based on the USGS (2002) national seismic hazard maps.

5.4.2.1 Development of Synthetic Ground Motions for Nonlinear Time History Analyses

A suite of synthetic ground motions are developed by Fernandez and Rix (2006) based on actual ground motions propagated from rock using SHAKE (Schnabel et al. 1972). The process to develop the synthetic ground motions is based on a site-specific probabilistic seismic hazard analysis (PSHA) for three specific locations previously shown in Figure 5.4:

- Cartersville, Georgia (Bartow County)
- Allenhurst, Georgia (Liberty County)
- Fort Payne, Alabama (Dekalb County)

The PSHA is conducted using EZ-FRISK^{TM}, a computer program for earthquake ground motion estimation developed by Risk Engineering, Inc. The characterization of seismic sources implemented in the PSHA is the same characterization that the U.S. Geological Survey (USGS) uses to develop their national seismic hazard maps (USGS 2002) for the CSUS region including the New Madrid and Charleston, South Carolina seismic sources and background seismicity of the CSUS (Frankel et al. 2002). The five rock attenuation relationships used to develop the USGS national seismic hazard maps (2002) are selected

to perform the analyses for this study based on past research conducted by Atkinson and Boore (1995), Campbell (2003), Frankel et al. (1996), Somerville and Saikia (2001), and Toro et al. (1997). The mean hazard curves at the three aforementioned locations for this study are computed using the same weight distribution applied to the attenuation relationships used in the development of the USGS national seismic hazard maps (USGS 2002). For each site, a deaggregation of the seismic hazard is used to determine the contribution of each magnitude and distance to the total hazard for a given return period. The mean hazard curves are used to calculate rock response spectra corresponding to a constant probability or uniform hazard response spectra (UHRS) for two return periods — 475 and 2475 years — corresponding to a 10% and 2% of probability of exceedance in 50 years, respectively. The UHRS calculated for rock are used to generate suites of spectrum-compatible ground motions for each site. The mean UHRS and its standard deviation are used to simulate 1000 response spectra for each hazard level. Ten simulations are then selected at random to use for spectral matching to obtain time histories compatible with the UHRS. The "seed" ground motions for the spectral matching process are selected from the time history database developed by McGuire et al. (2001). The CSUS time histories in this database are generated by scaling recorded motions for Western United States (WUS) conditions. The selection of the "seed" time histories is performed on records having similar magnitudes, epicentral distances, and site conditions to the earthquakes that dominate the hazard in each site as given by the seismic hazard deaggregation. The spectral matching process is performed in EZ-FRISK^{TM}. The rock time histories produced and used for the analyses are propagated from the rock to the surface level using the implementation of the program SHAKE, a

computer program for 1-D site response analysis (Schnabel et al., 1972), in EZFRISK^{TM}. Fernandez and Rix (2006) characterize the soil conditions to properly account for soil layer, shear wave velocity, type, thickness, classification, modulus reduction curves and damping curves for the three locations of interest for this study (Vucetic and Dobry 1991; Seed and Idriss 1970; Idriss 1990). Details of the soil conditions can be found in the Appendices.

Table 5.3: Magnitude and distance from controlling earthquake as determined from deaggregation maps

City	Moment Magnitude, M_w	Distance (km)
Cartersville, Georgia (Bartow County)	5, 6, 7	8-25
Allenhurst, Georgia (Liberty County)	7.5	125, 160
Fort Payne, Alabama (Dekalb County)	5, 6, 7	7-20, 30

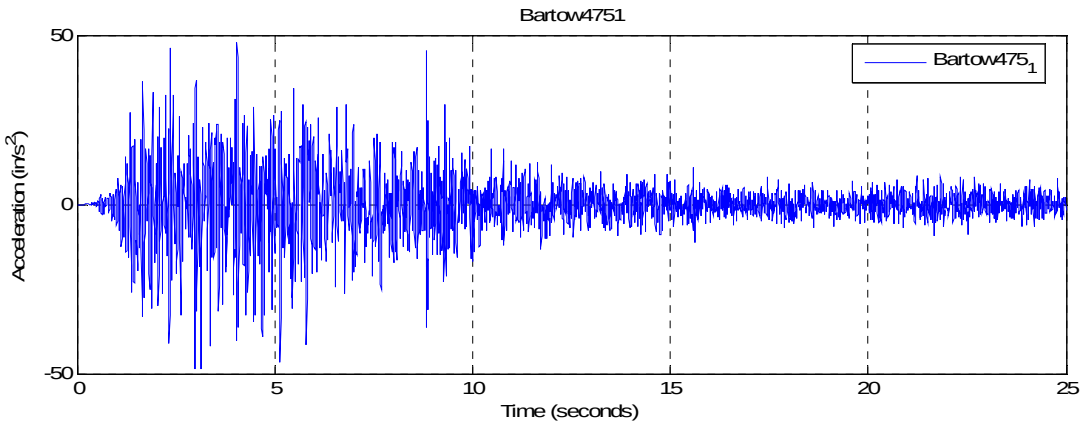

Figure 5.8: An acceleration time history for 475-year design earthquake for Cartersville, Georgia (Bartow County) developed by Fernandez and Rix (2006)

5.4.2.2 Response Spectra from Nonlinear Time History Analyses (NTHA)

The response spectra plotted in Figures 5.9 through 5.11 show the variation in acceleration with an average computed from the site-specific synthetic ground motions developed by Fernandez and Rix (2006) as a function of period for three locations noted previously in *Section 5.4.2.1*. The response spectra generated from the time histories for the suite of ground motions are compared to the uniform hazard response and design spectra presented in *Section 5.4.3* that are generated from the USGS (2002) national seismic hazard maps. The response spectra plots of the suite of ground motions used for the NTHA show that with increased damping from 2%, 5%, and 10% damping, the accelerations decrease, which is typical.

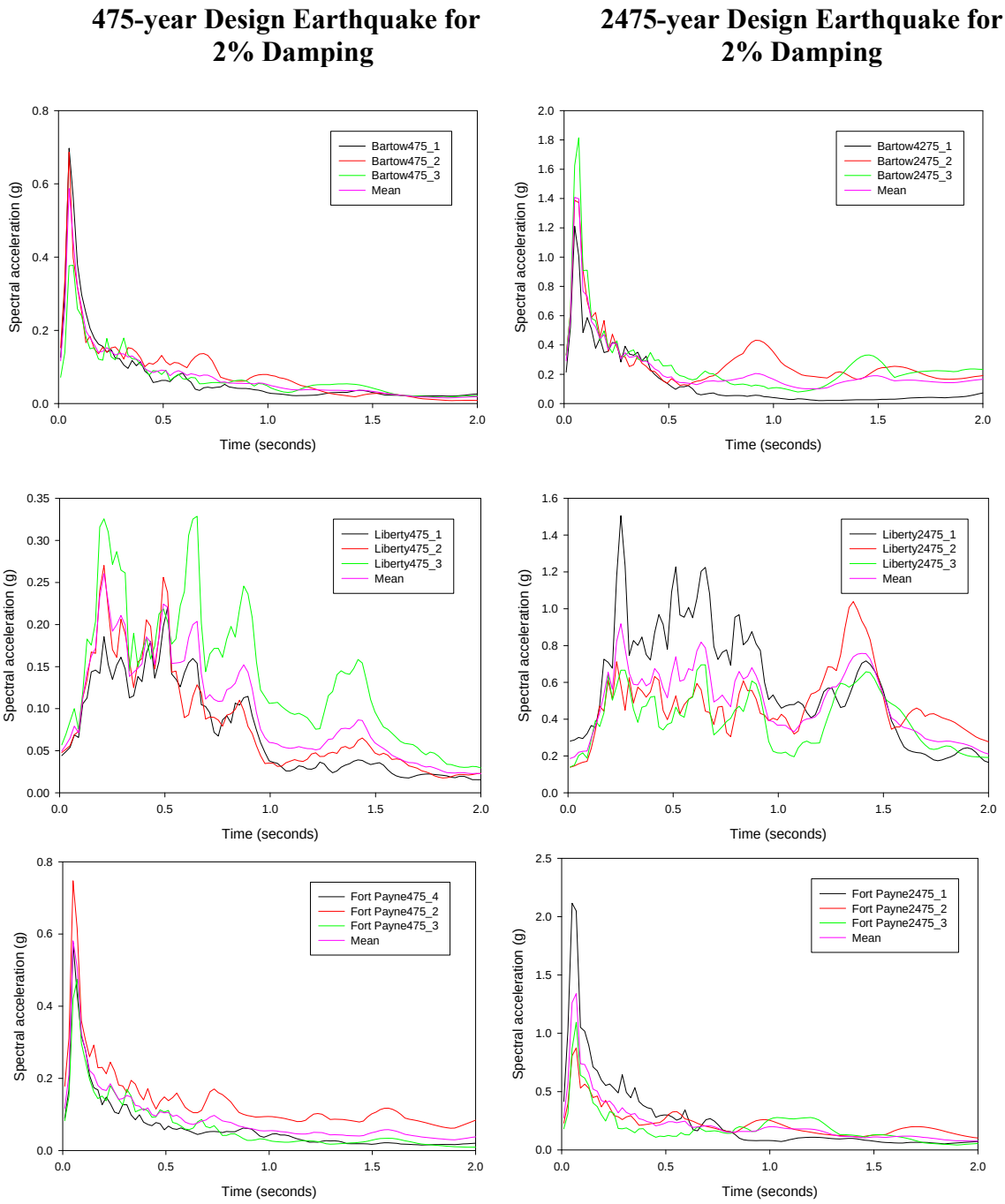

Figure 5.9: Response spectra of suite of synthetic ground motions used for NTHA for 475-year and 2475-year design earthquakes for 2% damping

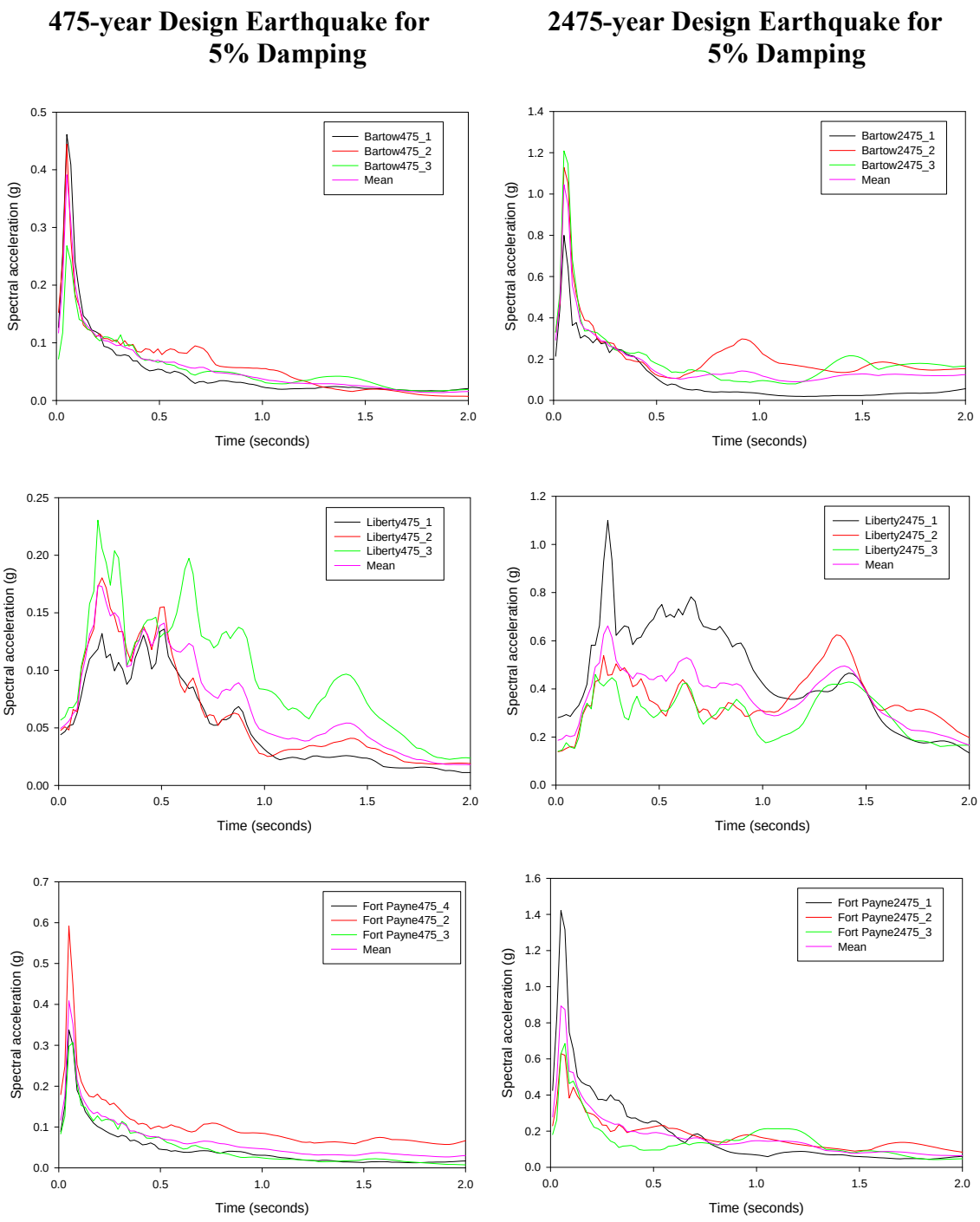

Figure 5.10: Response spectra of suite of synthetic ground motions used for NTHA for 475-year and 2475-year design earthquakes for 5% damping

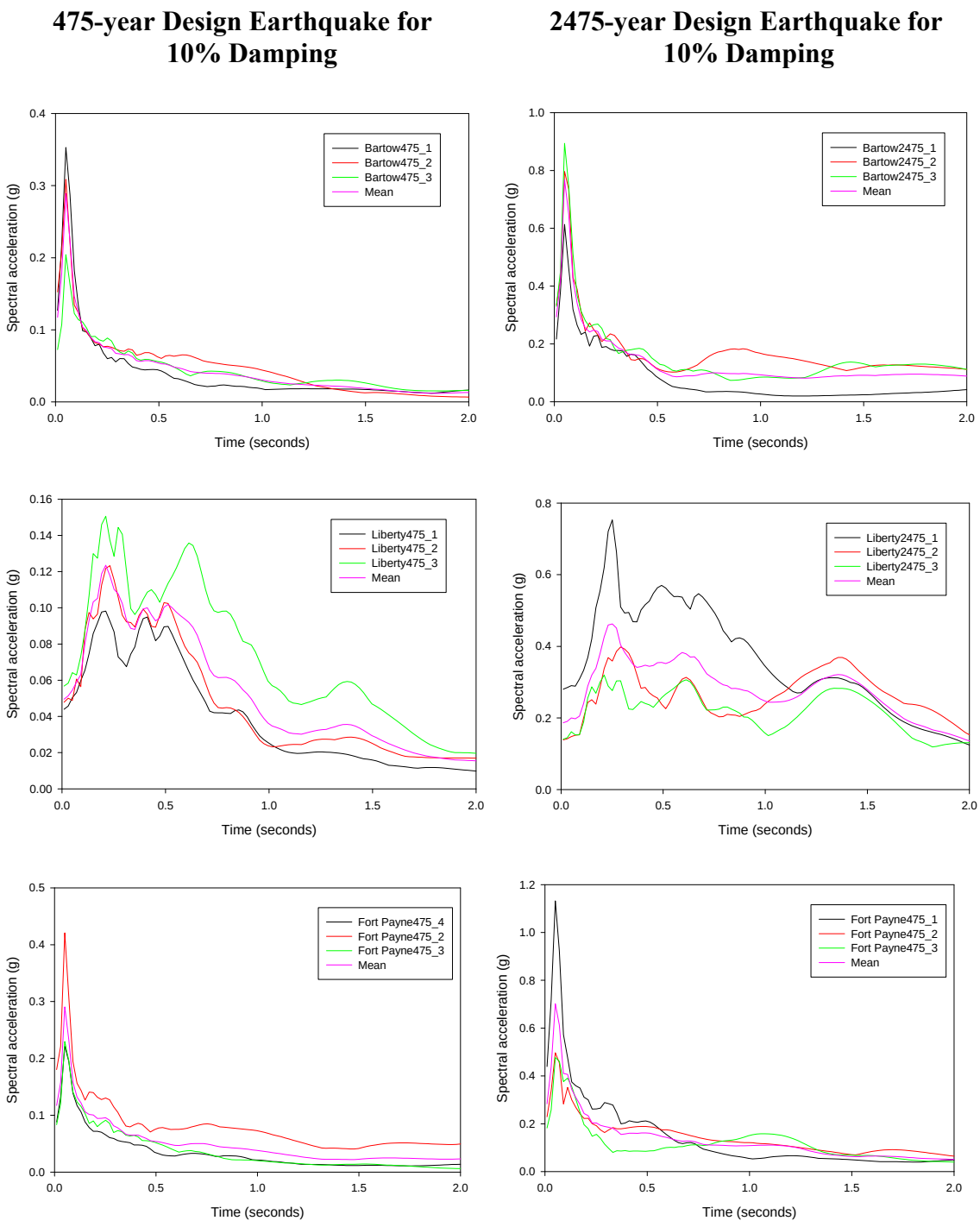

Figure 5.11: Response spectra of suite of synthetic ground motions used for NTHA for 475-year and 2475-year design earthquakes for 10% damping

5.4.2.3 Displacement Demands of Bridge Deck and Steel Pedestals

The displacement time history response shows how displacements in the system fluctuate as a function of the synthetic ground motion applied. The peak elastic displacements of the deck are important to note as pounding between multi-span decks or even the abutments can be of concern. While the peak elastic displacements for this 3DOF system can be directly determined from the response spectrum, the main point of the time history analyses is to determine the displacement demands on the pedestals as indicated by the inelastic force-deformation response of the spring element shown herein. The demand is compared to the peak deformation capacity from experimental testing of the pedestals, where the peak displacement is determined when a mode of deformation that may lead to a failure mechanism occurs.

The inelastic force-deformation response in the spring represents the relative motion between the deck (node 2) and the top of the pedestal (node 3) by which the displacement demands of the system are determined. The magnitude of the deformations plotted shows how the 3DOF is affected by inelastic action or yielding of the steel pedestal itself. The inelastic behavior defined by the hysteretic material in parallel with the steel pedestal material shows how the system is loaded, yields, unloads, and reloads at different points in time, if at all. The deformations in the spring are important as unseating or even instability of the pedestals may be a particular problem as the deformations get increasingly large. These large displacement demands may in fact exceed existing seat widths of the bent caps where the pedestals sit. Figures 5.12 and 5.13 show the output plots from OpenSees in terms of the acceleration time history from synthetic ground motion, displacement time history response of the 3DOF bridge model

revealing the peak displacements, and inelastic force-deformation response in the spring element for one case – test P1-1 subjected to a synthetic ground motion for Cartersville, Georgia (Bartow County). Figures 5.14 through 5.17 summarize the minimum and maximum deformation in the spring element of the 3DOF bridge model for a suite of ground motions at the 475-year and 2475-year design earthquake corresponding to 4 of the 6 test specimens.

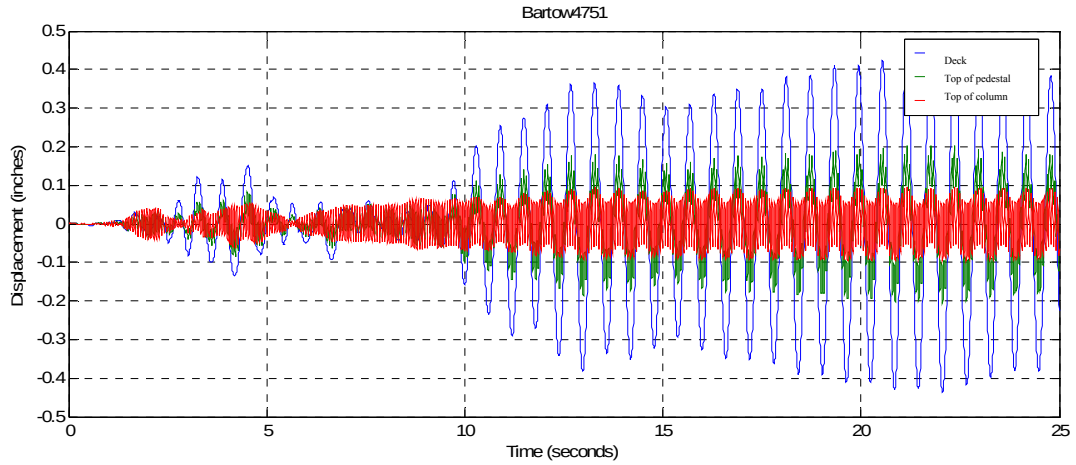

Figure 5.12: Displacements of the 3DOF bridge model for 475-year return period synthetic ground motion for Cartersville, Georgia (Bartow County)

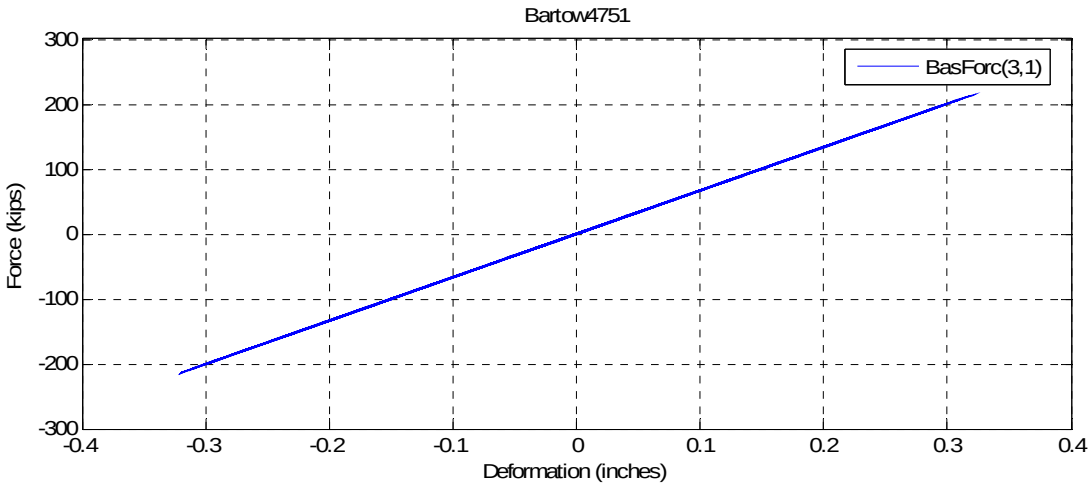

Figure 5.13: Inelastic force-deformation response of spring for 475-year return period synthetic ground motion for Cartersville, Georgia (Bartow County)

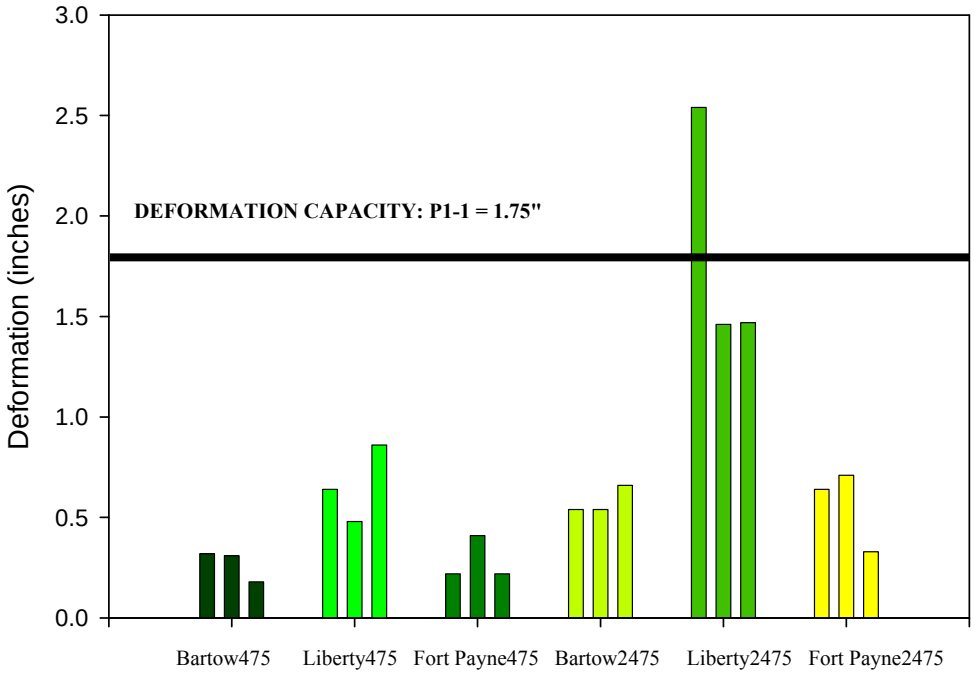

Figure 5.14: Absolute maximum deformation in the spring element for a suite of ground motions for the 3DOF bridge model corresponding to test P1-1 for the 475-year and 2475-year design earthquakes

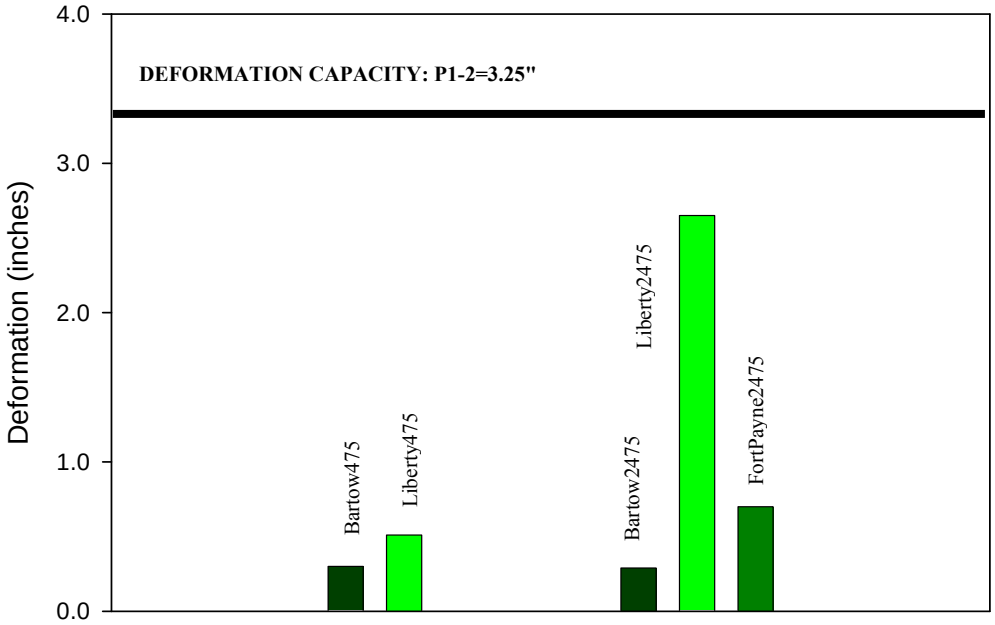

Figure 5.15: Absolute maximum deformation in the spring element for a suite of ground motions for the 3DOF bridge model corresponding to test P1-2 for the 475-year and 2475-year design earthquakes

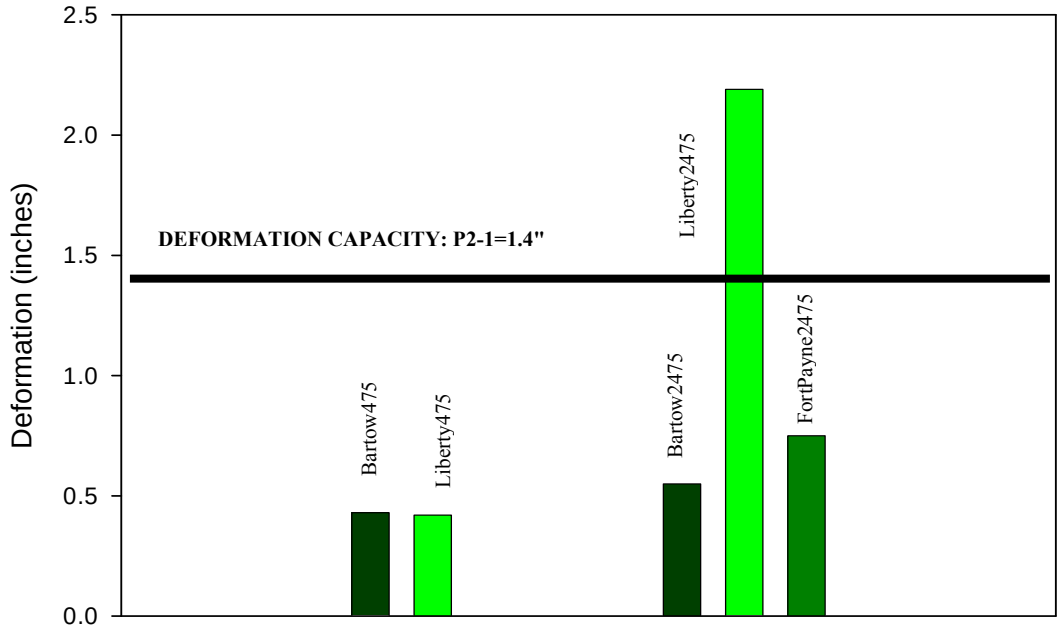

Figure 5.16: Absolute maximum deformation in the spring element for a suite of ground motions for the 3DOF bridge model corresponding to test P2-1 for the 475-year and 2475-year design earthquakes

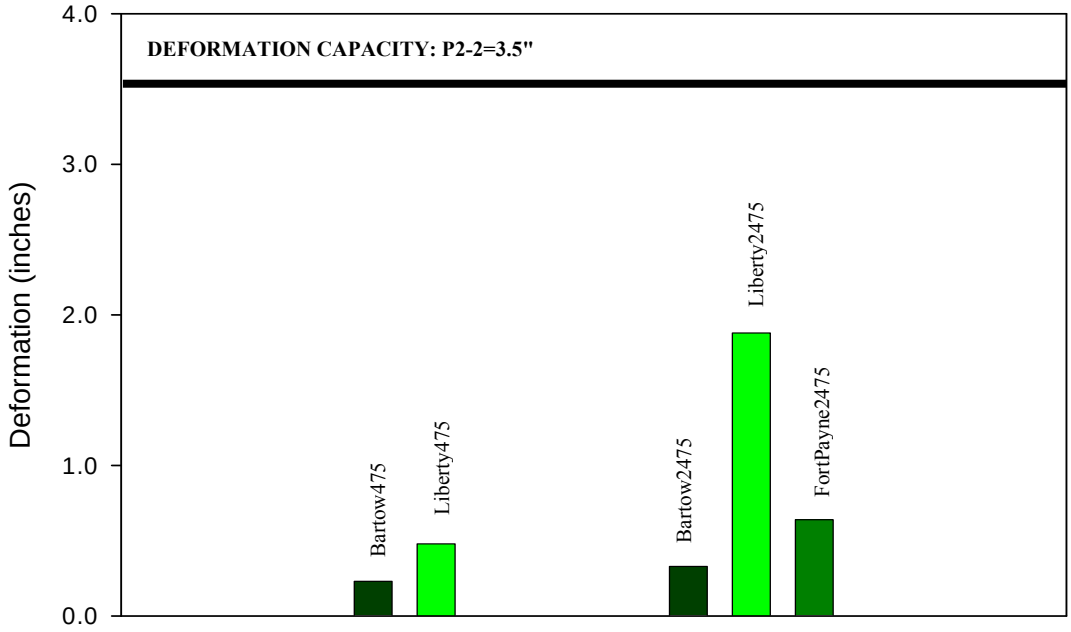

Figure 5.17: Absolute maximum deformation in the spring element for a suite of ground motions for the 3DOF bridge model corresponding to test P2-2 for the 475-year and 2475-year design earthquakes

5.4.3 Simplified Analysis using UHRS and Design Spectra from USGS National Seismic Hazard Maps

A simplified analysis to the nonlinear time history analyses (NTHA) is conducted by idealizing the 3DOF model into an effective single-degree-of-freedom (SDOF) model to determine the expected elastic displacements from the spectral accelerations for the range of structural periods noted in Table 5.3. The spectral accelerations for the uniform hazard response spectra (UHRS) are obtained using the *Probabilistic Hazard 3.10* software produced by Frankel and Leyendecker (2006), which provides the spectral accelerations based on the national seismic hazard maps (USGS 2002) for 5% damping. From the UHRS values for the short (0.2 seconds) and long (1.0 second) period, a 2-point procedure (FHWA 2006) is used to construct design spectra for three locations given a 475, 975, and 2475-year return period earthquake with appropriate site coefficients applied for site class C conditions that correspond to the respective locations:

- Cartersville, Georgia (Bartow County), zip code = 3012
- Allenhurst, Georgia (Liberty County), zip code = 31301
- Fort Payne, Alabama (Dekalb County), zip code = 35968

The locations chosen above are representative of low seismic loads. Specifically, the locations in Georgia are chosen because bridges in those respective counties have been elevated with steel pedestals (a complete listing of all bridges elevated in Georgia is shown in Table 6.2). The recent Fort Payne, Alabama earthquake (2003) has motivated the inclusion of this location for this study to determine levels of acceleration and elastic displacements that may be repeated in Georgia. Ground shaking was felt in Georgia during the Fort Payne, Alabama earthquake in 2003.

The expected elastic displacement demands of an effective SDOF bridge model are calculated from the spectral accelerations produced by the uniform hazard response spectra using Equation 5.5.

$$\Delta = Displacement(inches) = \frac{A*(386.4)}{\omega_n^{\,2}}, \qquad (5.5)$$

where Δ is the expected elastic displacement (in units of inches) computed from the spectral acceleration, A (in units of g) and the natural frequency, ω_n, of the idealized system. The spectra show the spectral acceleration in units of g versus the given periods in units of seconds for 5% damping. Figures 5.18 through 5.20 show the uniform hazard response spectra and design spectra for the three specified locations.

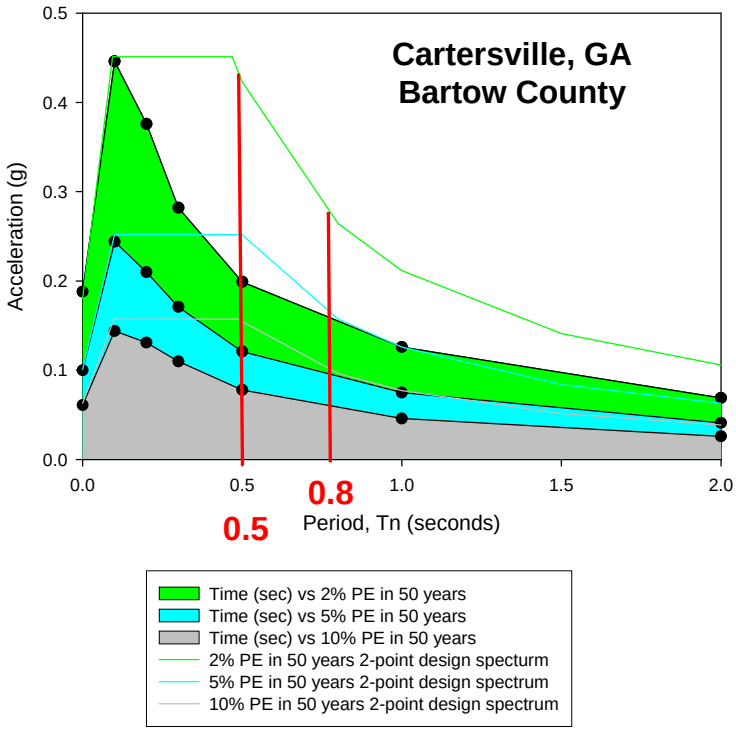

Figure 5.18: UHRS for Cartersville, GA for 2475, 975, and 475-year return period earthquake for the range of structural periods for the pedestals in Table 5.2

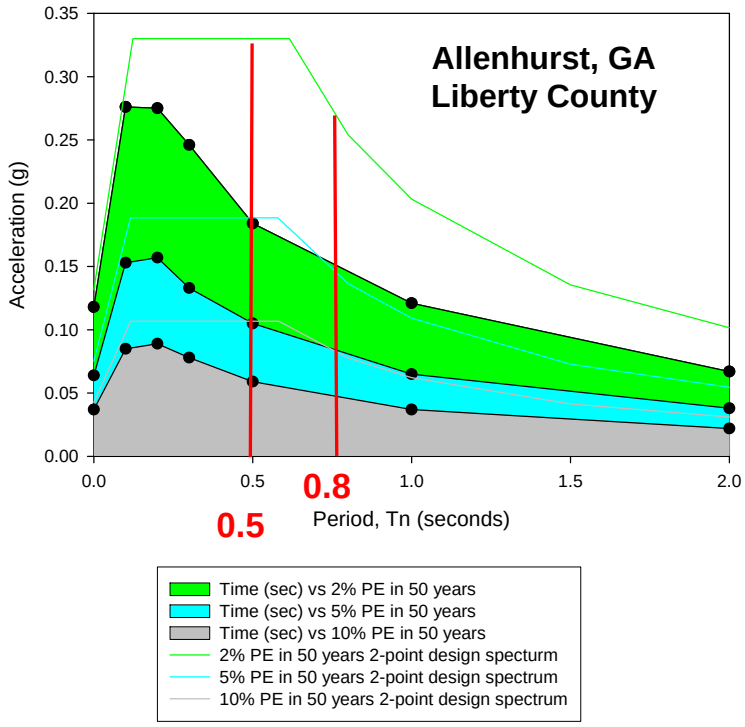

Figure 5.19: UHRS for Allenhurst, GA for 2475, 975, and 475-year return period earthquake for the range of structural periods for the pedestals in Table 5.2

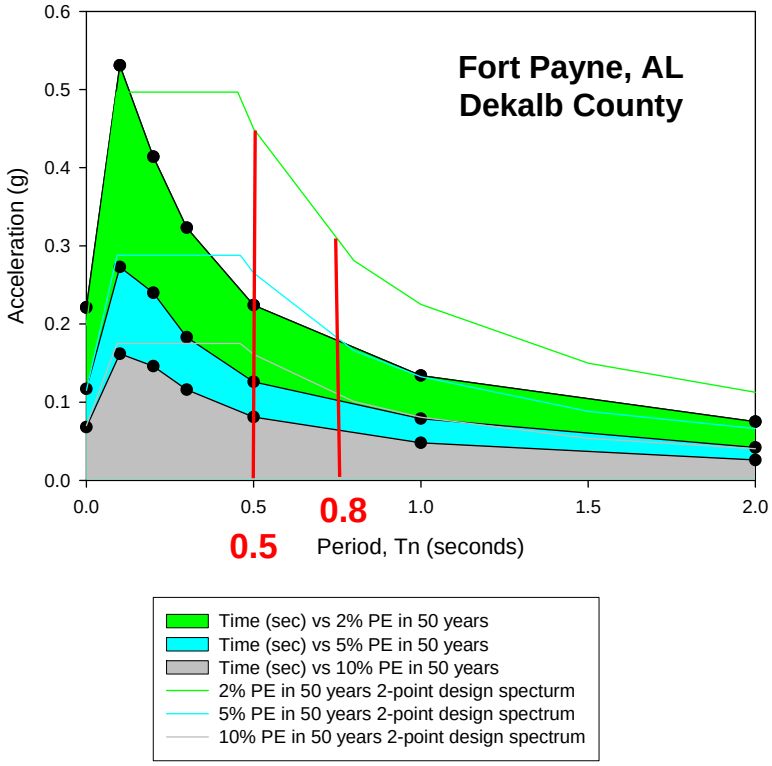

Figure 5.20: UHRS for Fort Payne for 2475, 975, and 475-year return period earthquake for the range of structural periods for the pedestals in Table 5.2

5.5 Comparison of Response Spectra from NTHA to Simplified Analysis

The response spectra generated from the nonlinear time history analyses that account for site-specific soil conditions show larger expected displacements than the displacements determined from the uniform hazard response spectra of an effective SDOF bridge model analyzed in *Section 5.4.3.* This difference is attributed to the inclusion of site-specific soil conditions. The site-specific soil conditions defined for the time histories better represent the existing physical conditions, which greatly influence the structural response. The design spectra shown based on a 2-point procedure (FHWA) for which site coefficients are applied also provide a simple means to approximate the elastic displacements based for an effective SDOF model.

5.6 Discussion of Results

The capacity of the steel pedestals, represented by a 3DOF bridge model in this study, exceeds the demand with an exception of the synthetic ground motion for Allenhurst, Georgia in Liberty County for the 2475-year return period earthquake for tests P1-1 and P2-1. A demand/capacity (D/C) ratio can be computed and compared to the peak displacement obtained for testing for assessing bridge vulnerability. The demand to capacity ratio is computed by dividing the inelastic deformation in the spring by the peak displacement obtained experimentally. For this abbreviated analyses, a bridge may be deemed "okay" if the demand to capacity ratio (D/C) is less than 1 (<1 is okay). If D/C > 1, a re-design of the pedestals shall be performed, considering the various pedestal types and configurations with their respective stiffness values. The analysis also shows the importance of including site-specific soil conditions to account

for regional geological effects, which may greatly change the demand of the structural response. Tables 5.4 and 5.5 show a comparison of the elastic deck displacements computed from the NTHA to the displacements computed from the spectral accelerations obtained from the UHRS and design spectra at 5% damping for a simplified analysis. The simplified analysis involves idealizing the 3DOF bridge model into an effective SDOF such that the displacements computed from the accelerations shown in the response spectra are displacements of the SDOF bridge model. The effective structural period of the idealized SDOF bridge model is used for comparison in Tables 5.3 and 5.4 is T_n = 0.5 seconds for the 475-year and 2475-year design earthquake, respectively. The 2-point design spectra have more built-in conservatism that provide a closer approximation to the displacements produced from the NTHA when comparing the displacements computed from the UHRS.

Table 5.4: Comparison of displacements from UHRS, 2-point Design Spectra, and NTHA for the 475-year design earthquake

Synthetic Ground Motion	**UHRS Demand** (inches)	**Design Spectrum Demand** (inches)	**NTHA Demand** (inches)
Cartersville, Georgia (Bartow County)	0.2	0.5	0.6
Allenhurst, Georgia (Liberty County)	0.2	0.3	0.7
Fort Payne, Alabama (Dekalb County)	0.2	0.4	0.6

Table 5.5: Comparison of displacements from UHRS, 2-point Design Spectra, and NTHA for the 2475-year design earthquake

Synthetic Ground Motion	**UHRS Demand** (inches)	**Design Spectrum Demand** (inches)	**NTHA Demand** (inches)
Cartersville, Georgia (Bartow County)	0.5	1.0	1.7
Allenhurst, Georgia (Liberty County)	0.5	0.8	1.7
Fort Payne, Alabama (Dekalb County)	0.5	1.1	1.2

CHAPTER 6

RECOMMENDATIONS

6.1 Overview

In assessing the performance of bridge steel pedestals, both experimentally and analytically, critical factors are identified and recommended as best practices and design guidelines for the performance of bridge steel pedestals. The recommendations for bridge steel pedestals are based on a series of six full-scale reversed cyclic quasi-static experimental tests that were conducted on a two-girder 40' simply-supported bridge span at the Structures Laboratory at the Georgia Institute of Technology (Figures 3.8 and 3.9). However, the effect of bridge skew and horizontal curvature is beyond the scope of this research in providing recommendations since transverse movement may become significant for skew angles greater than 20° in which the bearings are not aligned parallel to the movement of the structure; in that case, designers shall abide by the appropriate requirements and codes for quality bridge performance.

6.2 Best Practices

6.2.1 Construction tolerances to reduce effect of loading eccentricities

Best practice #1: *The centerlines of the girders shall be properly aligned within 0.25" of the centerlines of steel pedestals to minimize the effect of loading eccentricities.*

Reference: AASHTO LRFD Bridge Design Specifications, Article 2.5.3 "Constructability" (AASHTO LRFD, 2004)

Construction misalignments often contribute to loading eccentricities. Loading eccentricities may result in limiting the ultimate strength and deformation of the system and may cause a mechanism leading to a mode of failure. Therefore, it is imperative that the centerlines of the girders and steel pedestals are properly aligned and level. Axial compression tests of the steel pedestals were conducted to study the effect of loading eccentricities, which showed the importance of proper alignment as the pedestals are sensitive to very slight eccentricities. A recommended construction tolerance of less than 0.25" is suggested to minimize critical eccentricities over the web and at the centerlines. According to AASHTO LRFD Article 2.5.3, "Bridges should be designed in a manner such that fabrication and erection can be performed without undue difficulty or distress and that locked-in construction force effects are within tolerable limits."

6.2.2 Minimum concrete edge distance

Best practice #2: *The minimum concrete edge distance shall be taken as $6d_o$, where d_o is the bolt diameter at the concrete surface.*

Reference: ACI 318-05, Appendix D, Code D.8.3 (ACI 2005)

Minimum concrete edge distance is critical in the placement of the post-installed stud anchor bolts to fully develop the capacity of the bolts and minimize the concrete damage. Concrete breakout occurs when the concrete fractures before the load-carrying capacity of the steel is reached. For test P2-1, the tall pedestal was loaded along the plane of its strong-axis, where weld fracture occurred due to flexural bending of the weld during cyclic loading. The concrete breakout essentially consisted of unconfined concrete as a result of the anchor bolt being close to the edge of the concrete pier. The surface failure occurred at the predicted angle of 35° as shown in Figure 6.1. Past studies have shown anchor bolts to result in concrete damage during seismic loading similar to the concrete breakout that was observed in test P2-1. (More details of test P2-1 can be found in the Appendices). In cases where the specified minimum concrete edge distance is not satisfied, measures shall be taken to provide additional reinforcement. For instance, the reinforced concrete bent cap could be wrapped with fiber-reinforced polymers (FRP) or steel plates could be attached to provide confinement of the concrete.

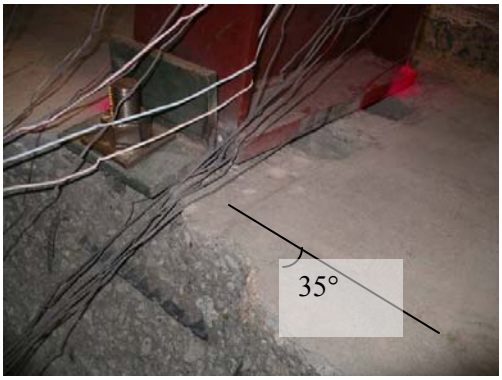

Figure 6.1: Concrete breakout at 35° on reinforced concrete pier due to insufficient concrete edge distance of the bolts

6.2.3 Minimum seat width

Best practice #3: *The minimum seat width shall be established based on the following:*

$$N = \left[100 + 1.7L + 7.0H + 50\sqrt{1 + (2\frac{B}{L})^2} \right] (\frac{1 + 1.25F_v S_1}{\cos\alpha}),$$

where N is in mm, L, B, and H are in meters and α *is in degrees.*

Reference: AASHTO, NCHRP Project 12-49, and FHWA/MCEER *Seismic Retrofitting Workshop Manual for Highway Structures: Part 1-Bridges* (FHWA 2006)

The determination of minimum seat width is critical since the steel pedestals may undergo considerable movement due to kinematic motion during cyclic loading, where both sliding and rocking occur on the abutment seat. The minimum seat width shall be established to avoid unseating of the bridge deck. Since the prediction of relative movement is often difficult to determine, the minimum support length can be calculated by:

$$N = \left[100 + 1.7L + 7.0H + 50\sqrt{1 + (2\frac{B}{L})^2} \right] (\frac{1 + 1.25F_v S_1}{\cos\alpha})$$

where the FHWA/MCEER *Seismic Retrofitting Workshop Manual for Highway Structures: Part 1-Bridges* (2006) defines the input variables as follows:

- N is the recommended support length measured from the normal to the face of an abutment or pier (mm)
- L is the length of the bridge deck from the seat to the adjacent expansion joint, or to the end of the bridge deck (m). For hinges or expansion joints within a span, L is the sum of the distances on either side of the hinge (m); for single-span bridges, L is the length of the bridge deck (m)
- H is the height. For abutment seats, H is the average height of piers or columns supporting the bridge deck between the abutment and the next expansion joint (m). For pier seats, H is the height of the pier (m); for hinge seats within a span,

H is the average height of the two adjacent piers (m); for single-span bridges, H=0.

- B is the width of the deck (m); NOTE: the ratio B/L shall not be greater than 3/8
- α is the angle of skew (0° for a right bridge)
- $S_{D1} = F_V S_1$ is the product of the long-period soil factor (F_V) and the 1.0 second spectral acceleration (S_1)

In cases where the specified minimum seat width is not satisfied, measures shall be taken to provide additional seat width. Seat extensions could be used to provide additional seat width. The extensions shall be anchored to the vertical face of the concrete abutment or pier with dowels or anchor bolts. These dowels or anchor bolts shall be designed to carry large vertical and horizontal forces due to the loads imposed by the superstructure if the bearings were to fail. Post-tensioning the seat extensions to the substructure is recommended when feasible.

6.3 Design Guidelines

6.3.1 Stud anchor bolt design strength

Guideline #1: The swedged stainless steel stud anchor bolts shall be covered with a minimum of Grade 36, thereby providing a minimum yield strength of 36 ksi instead of 30 ksi as indicated by the manufacturer's readings for the swedged stainless steel stud anchor bolts used in the experimental testing.

Reference: Steel Anchor Bolts AASHTO Designation: M 314-90 (1996)

The stud anchor bolts connected to the steel pedestals shall consist of swedged stainless steel and conform to the standard specifications for steel anchor bolts as prescribed in the AASHTO Designation M 314-90. The mechanical properties of the swedged stainless steel post-installed stud anchor bolts from the manufacturer (Craddock 2006) used for the experimental investigation are shown in Table 6.1. However, based on the AASHTO Designation M 314-90 Article 4, the anchor bolts shall be covered with a minimum of Grade 36, thereby providing a yield strength of 36 ksi instead of 30 ksi.

The steel pedestal stud anchor bolts shall be designed such that the anchor bolt resistance is "governed by a ductile steel element or the yield capacity of a ductile steel attachment to which the anchors are connected (Eligehausen et al. 2006)." Forcing this mechanism ensures some measure of ductile response although the aforementioned guideline cannot be expected to be "earthquake proof."

Table 6.1: Stainless steel anchor bolts manufacturer's "Mill Test Analysis Certificate" readings 1/31/2006

Specified Values	Yield Strength (ksi)	Tensile Strength (ksi)
Minimum	30	75
Results	57.6	92.8

6.3.2 Anchorage and grouting

Guideline #2: Stud anchor bolts shall be embedded a minimum of [12", $12d_b$], not to exceed 2/3 of the member thickness, and shall be anchored in a non-shrink grout that conforms to ASTM C1107 and the Corps of Engineers Specification: CRD-C 621.

Guideline #3: A minimum edge distance twice the maximum aggregate size shall be used as to not cause microcracking when drilling the holes for the post-installed stud anchor bolts.

Reference: ASTM C 1107, Grades A, B, and C; Core of Engineers Specification, and ACI Appendix D

Proper anchorage of the stud anchor bolts is important for the development of the bolt capacity. The stud anchor bolts shall be embedded no deeper than 2/3 of the member thickness and shall be anchored in a non-shrink grout that conforms to ASTM C 1107 and the Corps of Engineers Specification: CRD-C 621. Two types of grout were used: 1) Horn non-corrosive, non-shrink grout provided by Highway Materials conforming to ASTM C 827 and CRD-C 621 and 2) 588 Precision Grout from W. R. Meadows conforming to ASTM C 1107, Grades A, B, and C and CRD-C 621. Tests P1-1 through P2-1 were conducted using the Horn grout and tests P2-2 through P3-1 used the 588

Precision Grout. Tests P2-2 and P3-1 revealed better performance of the grout. In fact, test P2-2 showed the highest peak displacement of ±3.5" (see Appendix A for more details). Therefore, grouts conforming to CRD-C 621 and ASTM C 1107, Grades A, B, and C are recommended as guidelines for the bridge steel pedestals.

From RD.8.3 in the Commentary of Appendix D (318-05), it is important to note that "drilling holes for the post-installed stud anchor bolts can cause microcracking. The requirement for a minimum edge distance twice the maximum aggregate size is to minimize the effects of such microcracking." Although microcracking was not observed during the experimental investigation, the possibility for this occurrence shall be duly noted. Also, from RD.8.5, "post-installed anchors should not be embedded deeper than 2/3 of the member thickness." Both of these guidelines should help with quality control and development of the bolt capacity.

6.3.3 Slots of L-shaped angles to allow for sliding

Guideline #4: L-shaped angles with slotted holes are preferred to allow for sliding of the pedestals.

Sliding of the pedestals on the elastomeric (neoprene) pad is beneficial and critical for dissipating energy. The slotted holes allow for the pedestals to slide on the ⅛" elastomeric (neoprene) pad before engaging the anchor bolts when subjected to shear loads. When sliding is permitted, the steel pedestals can be thought to act as isolators. Larger slots provide a means for a larger tolerance for sliding and therefore dissipation of energy. For the case when the anchor bolts are drilled with the cross-section of the pedestals, slotted holes can also be utilized to allow for more sliding in the system.

6.3.4 Expected spectral accelerations and seismic design categories for Georgia

Guideline #5: Dade, Catoosa, Walker and Chattooga Counties shall also be considered as Seismic Design Category B in Section II of GDOT's *Bridge General* specification based on expected spectral accelerations for that region.

Reference: United States Geological Survey (Frankel and Leyendecker 2006)

Based on the U. S. Geological Survey Probabilistic Hazard 3.10 software, Dade, Catoosa, Walker and Chattooga Counties in Georgia should also be included as Seismic Category B given the expected spectral accelerations for the earthquake return periods of 475, 975 and 2475 years for the state of Georgia. Since the spectral accelerations for Dade, Catoosa, Walker and Chattooga Counties exceed that of the expected spectral accelerations for Bartow County which is considered a seismic category B, Section II of GDOT's *Bridge General* specification shall also consider these four counties as seismic category B as shown in Figure 6.2.

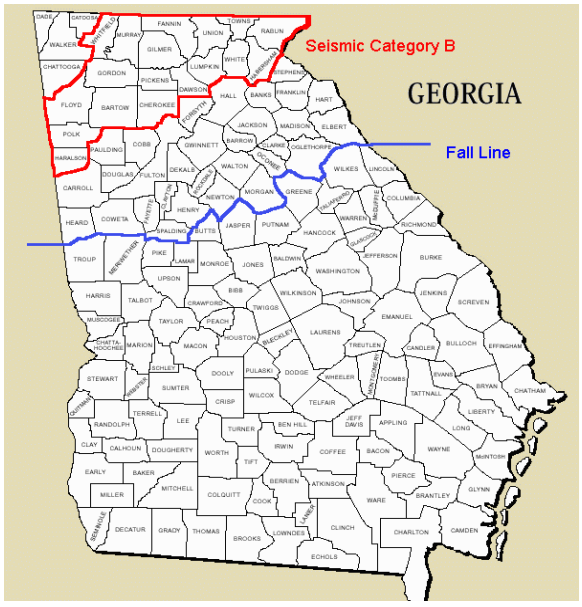

Figure 6.2: 2475-year seismic hazard design map for the state of Georgia (GDOT 2004)

6.4 Inspection and Maintenance

The steel pedestals should be inspected routinely to ensure that the ⅛" elastomeric (neoprene) pad has not "walked out" from under the steel pedestal and that the pedestals themselves are protected from corrosion. Based on AASHTO (2004), "all exposed steel parts of bearings not made from stainless steel shall be protected against corrosion by zinc metallization, hot-dip galvanizing, or a paint system approved by the Engineer. Additionally, the steel pedestals should be carefully inspected for the presence of dirt or other debris that may prohibit movement of the pedestal. The use of stainless steel anchor bolts is the most reliable protection against corrosion because coatings of any sort are subject to damage by wear or mechanical impact." Therefore, a formally adopted, consistent maintenance inspection of the steel pedestals shall take place, where the elastomeric (neoprene) pad is inspected for proper seating and that the steel pedestals are protected from corrosion. Prioritization for inspection and maintenance can be based on the results from the bridge vulnerability discussed in the previous section. Table 6.2 shows a list of more than 50 bridges in Georgia that Bellamy Brothers (contractors) have elevated with steel pedestals.

Table 6.2: Bridges in Georgia that have been elevated with steel pedestals (Myers 2005)

Georgia County Name	Existing GDOT Bridges Elevated with Steel Pedestals									
Bibb-Monroe	Estes Rd Over I-475	Zebulon Rd over I-475	I-475 over Tobeso Pkee Creek	I-475 over Tobeso Pke Crk Ovrflo	Eisenhower SR 80 over I-475	SR 74 Mercer Rd over I-475	SR 22 Clmbus Rd over I-475	I-475 over Rocky Creek	Peake Rd over I-475
Bartow	Pleasant Valley Rd I-75		Cassville White Rd over I-75						
Camden	St. Mary's Rd I-95		MLK over I-95	Harriett Bluff over I-95					
Cherokee	Woodstock Rd over I-75								
Cobb	Six Flags Rd I-20	Factory Shoals I-20	All Good Rd I-75	Chastain Rd I-75	Hikry Grve Rd I-75	Wade Gren Rd I-			
Crisp-Turner	Begood Rd I-75	Hwpond Rd over I-75	Mussel White I-75	Old Hatley over I-75	Rock Wenona over I-75	Wardlow Rd over I-75			
Dekalb	Fairington Rd over I-20		Panthersville Rd over I-285						
Fulton	Conley over I-285								
Henry	Locust Grove over I-25		Indian Crk over I-75	Bethlehem over I-75					
Jackson	SR 82 Spur over I-85		SR 88 over I-75		Maysville Rd	SR 98 I-85	SR 60 I-85		
Liberty	Isle of Wight Rd I-85		SR 84 I-95	Retreat Rd over I-95					
Lowndes	Shiloh Rd over I-75		SR 22 I-75						
Peach-Hudson	SR 26 I-75	Firetower Rd over I-75		Gaines Dr. I-75	Todd Rd I-75	Thompson Rd over I-75			
Richmond	Wheeler Rd over I-520		Wngntsboro Rd over I-520		SR 278 I-520	Milledgeville Rd I-520			
Tift	Chula Brookfield Rd I-75		Willis Stills I-75	Bnghton Rd I-75	Westley Riddon Rd I-75				
Troup	Old West Point over I-20								

CHAPTER 7

CONCLUSIONS

7.1 Summary

Six reversed cyclic, quasi-static large-scale experimental tests are conducted on a two-span girder 40' bridge specimen rehabilitated with both 19" and 33½" pedestals used to boost bridges in Georgia. The six tests show varying deformation (1.75" to 3.5") and strength capacity (25.8 kips to 96.4 kips) of the pedestals for two loading directions (strong- and weak-axis) and two configurations for the placement of the anchor bolts. Tests from this study reveal the pedestals to be elastic, flexible components, where peak displacements reached are limited by a deformation mode rather than permanent deformation or instability of the pedestals themselves. The three modes of deformation observed are prying-action, bolts yielding, and concrete breakout. Prying-action of the anchor bolts embedded in the reinforced concrete bent cap is the predominant mode as the anchor bolts pullout from the concrete with increased cycling due to sliding (anchor bolts subjected to shear loading) and rocking of the pedestals (anchor bolts subjected to tensile loads).

Large-scale experimental testing of the system validates the load transfer mechanisms and provides realistic force-displacement relationships. The force-displacement relationships capture the rigid body kinematics (sliding and rocking) of the system while also showing the inherent hysteretic nature of the pedestals. From all six hysteresis loops, 7-17% of energy is dissipated by equivalent viscous damping of the pedestals, which is a necessary characteristic for the seismic performance of connection elements during an earthquake. The displacement ductility ratio, μ, ranges from 2.8 to 13

for all six tests, where ductility ratios from 4 to 6 may be expected in extreme seismic events. From the force-displacement hysteretic relationships, other response parameters such as the effective stiffness and equivalent viscous damping of the pedestals are computed and compared. The force-displacement hysteretic relationships, in turn, are used to calibrate an analytical bridge model to determine the displacement demands.

A GDOT candidate bridge with steel pedestals is idealized as a 3DOF system to determine the bridge displacement demands using two approaches:

(1) by calculating the peak displacement from accelerations generated by uniform hazard spectra based on USGS (2002) maps for the range of structural periods from all six tests represented by the 3DOF system, and

(2) by calculating the peak displacements from response spectra generated from a suite of site-specific synthetic ground motions developed by Fernandez and Rix (2006); time history analyses are conducted on the 3DOF model developed in OpenSees to also determine the inelastic force-deformation behavior in the spring based on force-displacement hysteretic relationships defined by from experimental tests results.

A hysteretic material using the force-displacement hysteretic relationships that encompass the rigid body kinematics, deformation capacity, and strength capacity of the pedestals is defined for the pedestal material. The hysteretic material is modeled in parallel with the properties of the steel pedestal sections and yield strength of 50 ksi for the steel material. The inelastic deformations in the spring, which represent the displacement demands on the pedestals, do not exceed the capacity of the pedestals for the respective tests with the exception of one of the ground motions developed for the

2475 design earthquake for Liberty County. The elastic displacements computed from the response spectra of the site-specific synthetic ground motions developed by Fernandez and Rix (2006) for levels expected in Georgia and Fort Payne, Alabama exceed the elastic displacements computed using the uniform hazard response spectra from the USGS (2002) national seismic hazard maps adjusted for site class C soil conditions. Consequently, this demonstrates the importance of accounting for regional geological effects such as deep profiles of unconsolidated sediments that can significantly affect the response. For this simple 3DOF model of a candidate bridge in Georgia, the inelastic behavior defined for the pedestals reveal satisfactory performance for low seismic loads where the deformation and strength capacity are adequate as long as a mode of deformation leading to a mechanism of failure does not occur. Best practices and design guidelines are recommended to reduce the likelihood for potential modes of deformation that may affect the response and lead to a failure mechanism, thereby limiting the performance of the steel pedestals.

7.2 Impact of Research

The impact of this research directly affects the sponsor of this research, the Georgia Department of Transportation (GDOT), but also can be extend to other states interested in using steel pedestals as an effective means to elevate bridges while also providing structural resiliency for low seismic loads. The significant impact of this research includes:

- a better understanding of the deformation and strength capacity of steel pedestals, effective stiffness, behavior of the steel pedestals (i.e.,

undergoing rigid body kinematics), and modes of deformation leading to failure mechanisms

- design recommendations to GDOT on best practices for steel pedestal in GA (design, construction, connectivity) based on the results from the experimental testing and analytical studies
- a simple methodology to conduct a vulnerability assessment of the steel pedestals existing on bridges in Georgia using an idealized 3DOF bridge model
- a methodology to assess the seismic performance of bridges that use similar supports such as high-type rocker bearings
- an understanding the performance of these steel pedestals under low-to-moderate seismic loads for others states besides Georgia

7.3 Recommendations for Future Work

The research presented herein can be extended to include the following:

- development of a 2- or 3-dimensional bridge model that includes more refined elements to model the plastic hinges in the columns, modeling of the abutments, translational springs to include the effects of deck pounding, translational and rotational springs to model the foundation, and pile-soil interaction
- parametric studies of the 2- or 3-dimensional model for sensitivity analyses

- time history analyses of the 2- or 3-dimensional model subjected to a suite of synthetic ground motions representative of moderate-to-high seismic loads

APPENDIX A

DETAILS OF EXPERIMENTAL TEST RESULTS

A.1 P1-1 short pedestals, loading about its strong-axis

The first test consisted of the short pedestals, where the L-shaped angles were welded to the base plate of the pedestals and placed perpendicular to the plane of loading (Figure A.1). The pedestals, consisting of W8x31 sections, are oriented such that the in-plane loading results in bending along the strong-axis of the pedestal. The swedged stainless steel stud anchor bolts are positioned perpendicular to the loading direction and are embedded 12" into the reinforced concrete pier. The bridge specimen is loaded in displacement control using an MTS 243.45 actuator, where target displacements are defined for a set number of cycles. Loading occurs as the bridge specimen is pushed away from the structural wall. The specimen is unloaded and then reloading occurs such that the specimen is pulled toward the structural wall.

Figure A.1: Photograph of as-built specimen with 19" pedestals loaded about its strong-axis (P1-1)

Initially, the hysteretic relation of the pedestals results in a linear, elastic response at 0.3" displacements and smaller. Friction in the system results in a small amount of energy being dissipated as shown in the force-displacement hysteretic relationships at small, shakedown displacements (Figure A.2). The amount of energy dissipated is quantified by calculating the area within the hysteresis loop shown in the force-displacement relation. The load corresponding to 0.3" displacement ramped up to approximately 17,141 lbs. Residual strain is revealed as the specimen is loaded and unloaded. At 0.5" displacement, the force-displacement behavior begins to show more nonlinear qualities with loads corresponding to 13,859 lbs. With increased cycling, strength degradation occurs and the hysteretic loops soften. From the strain gauges, the steel pedestals do not exceed the yielding strain of steel and therefore do not yield. The nonlinear behavior shown in the force-displacement relationships are due consequently to the energy released during cycling.

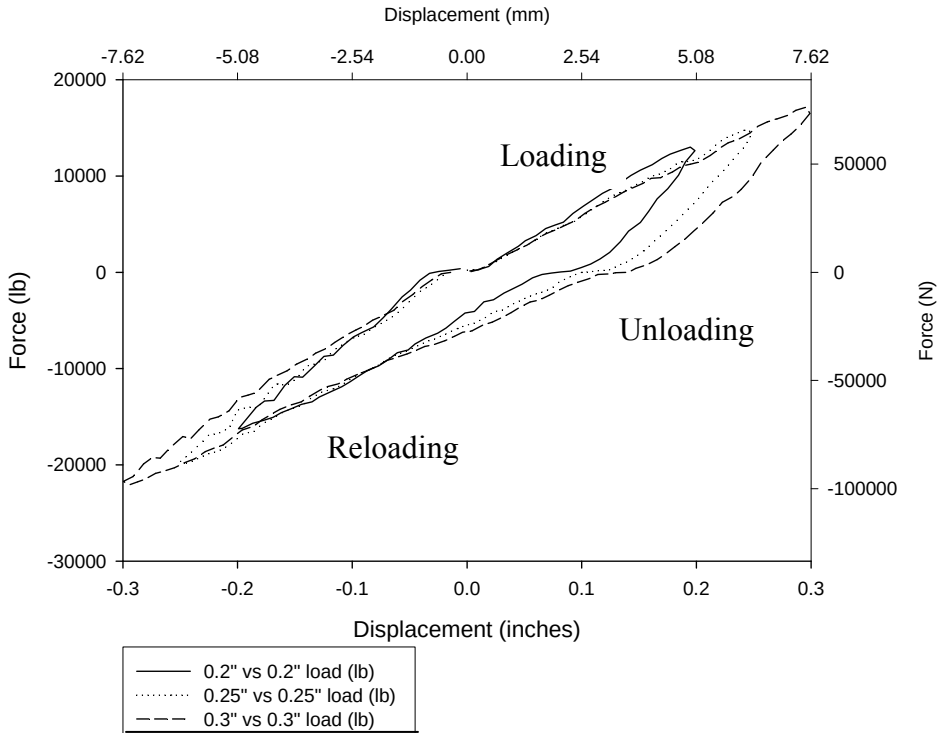

Figure A.2: Shakedown force-displacement relationships of 19" pedestals, strong-axis loading (P1-1)

However, beginning at 0.65" displacement, the pedestals begin to slide as shown by the increase in displacement with the load remaining relatively constant around 10,000 lbs (Figure A.3). With increased cycling, there is a decrease in the load or strength capacity. As the pedestals slide on the elastomeric (neoprene) pad, more residual displacement is apparent and the bolts begin to be engaged as the pedestals slide and then begin to rock as seen by the pinching phenomenon in the hysteresis loops. The pedestals slide and realign themselves such that the neutral axis of bending shifts, thereby changing the center of rotation. The effect results in unsymmetric loading of the specimen, where the loads resisted in compression (reloading specimen) are almost twice that of the loads resisted in tension (loading specimen) to compensate for the force balance in the system. Suddenly at 0.75", there is a stiffening of the system as the specimen is displaced more, thereby

engaging the anchor bolts as load-carrying elements. This behavior is repeated as cycling continues. Eventually, a peak displacement of 1.75" is reached and the test is stopped when a diagonal crack initiated from the stud anchor bolt propagates from the surface of the pier cap down the side of the pier cap.

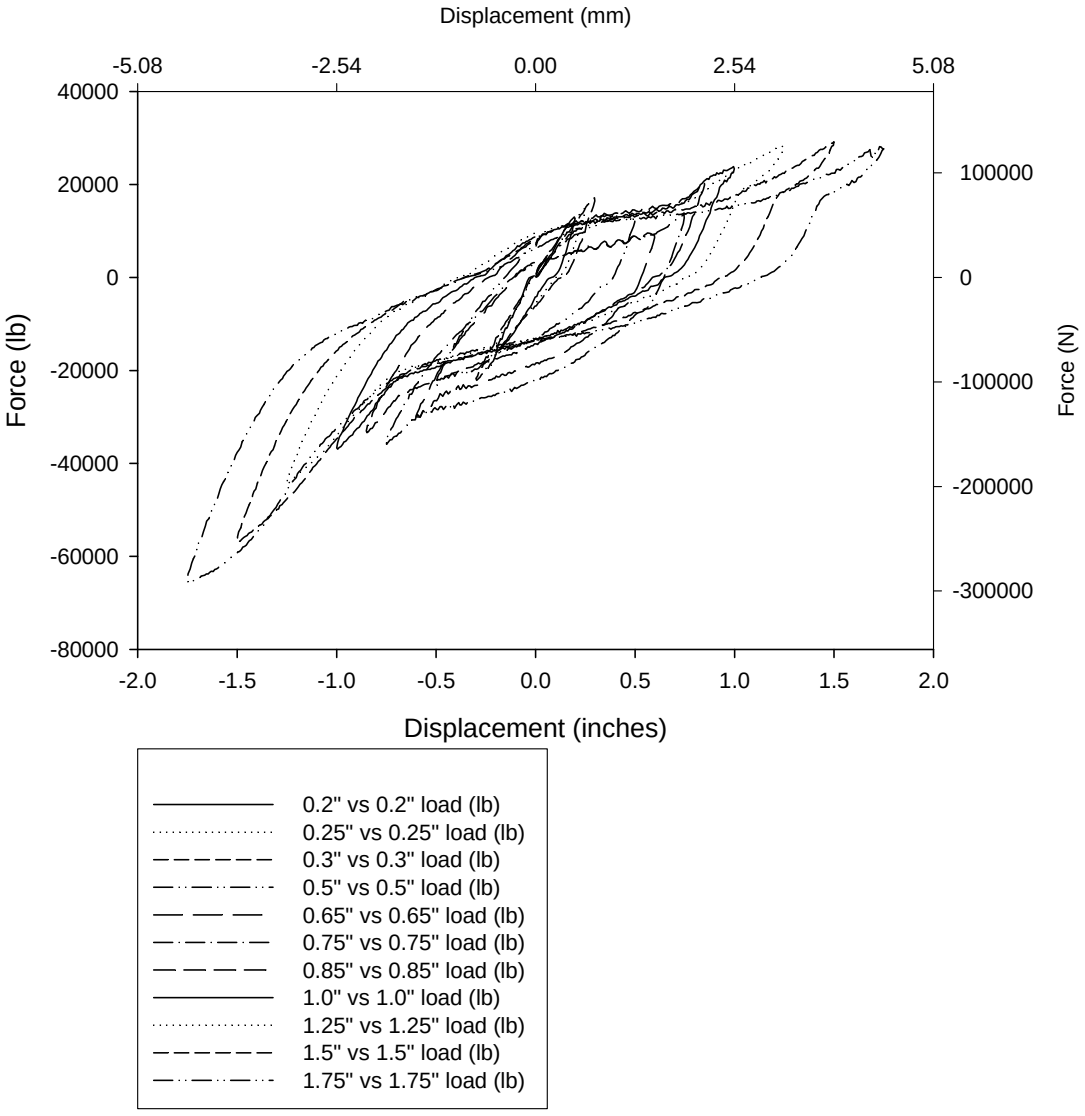

Figure A.3: Force-displacement relationships of 19" pedestals, strong-axis loading tests (P1-1)

A.2 P1-2 short pedestals, loading about its weak-axis

New holes are drilled into the reinforced concrete pier to set the bolts for placement such that the short pedestals are loaded about its weak-axis for test P1-2 (Figure A.4). The set of short pedestals are rotated 90° from test P1-2 to study the behavior in the hysteretic response of the pedestals when loaded about its weak-axis. For the short pedestals loaded about its weak-axis, nonlinear behavior in the hysteretic response is similar to the results obtained from P1-1.

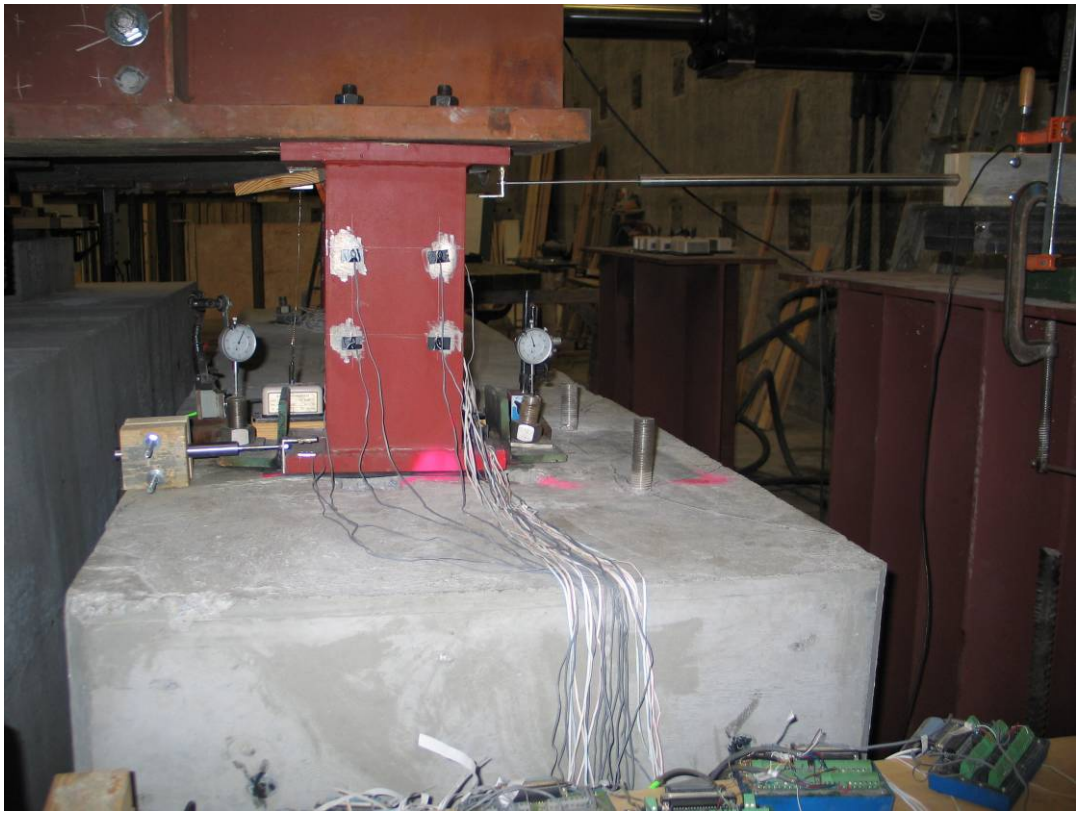

Figure A.4: Photograph of as-built specimen with 19" pedestals loaded about its weak-axis (P1-2)

However, the deformation and strength capacity of the results produced from test P1-2 is almost twice that of the results obtained from P1-1. Shakedown tests are conducted at +/- 0.1" displacements to observe the initial linear, elastic response of the system (Figure

A.5). Next, a target displacement of 0.25" is set to characterize the response, where an initial yield is observed at 0.25". Cycling continues as the target displacements are increased incrementally, similar to the loading protocol for P1-1. More sliding of this orientation is allowed due to the slots in the L-shaped angles that allow more space for the pedestals to slide before the anchor bolts are engaged. Sliding is evident at approximately +/- 15,000 lbs as there is an increase in displacement but relatively little increase in load.

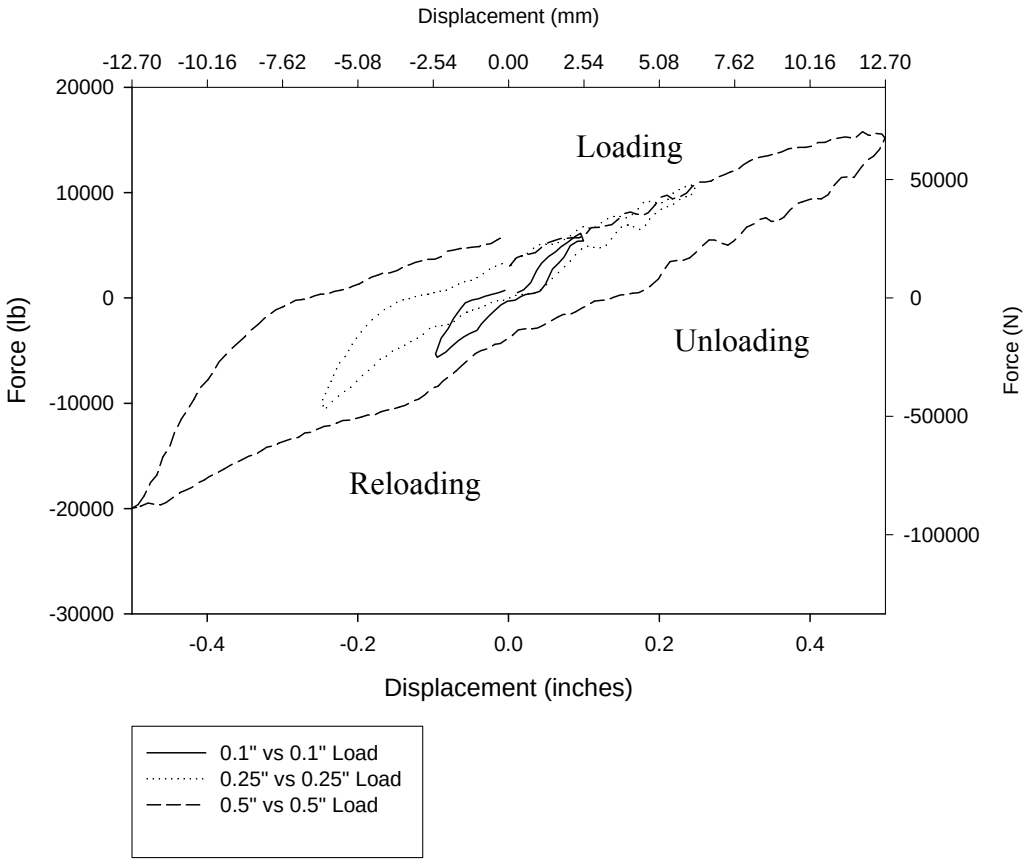

Figure A.5: Shakedown force-displacement relationships of 19" pedestals, weak-axis loading (P1-2)

Sliding continues until the anchor bolts are engaged as load-carrying elements where rocking of the pedestals occurs and pinching of the hysteresis is observed at peak loads. The pedestals slide for almost 2" as the specimen is loaded and reloaded. The configuration of the slot holes within the L-shaped angles provide more allowance for sliding, and therefore seem to allow for larger loads to be reached once the pedestals slide and then engage the bolts as load-carrying elements. The amount of sliding and rocking is captured by the instrumentation and is explained in more detail in *Section 4.2, Response Assessment of Steel Pedestals*. A peak displacement of 3.25" is reached when the test is stopped. The deformation capacity of 3.25" is almost twice that of P1-1, where a peak displacement of 1.75" as reached. Peak loads of almost 80,000 lbs (tension loading) and 100,000 lbs (compression reloading) are reached, nearly tripling the strength capacity compared to test P1-1 (Figure A.6).

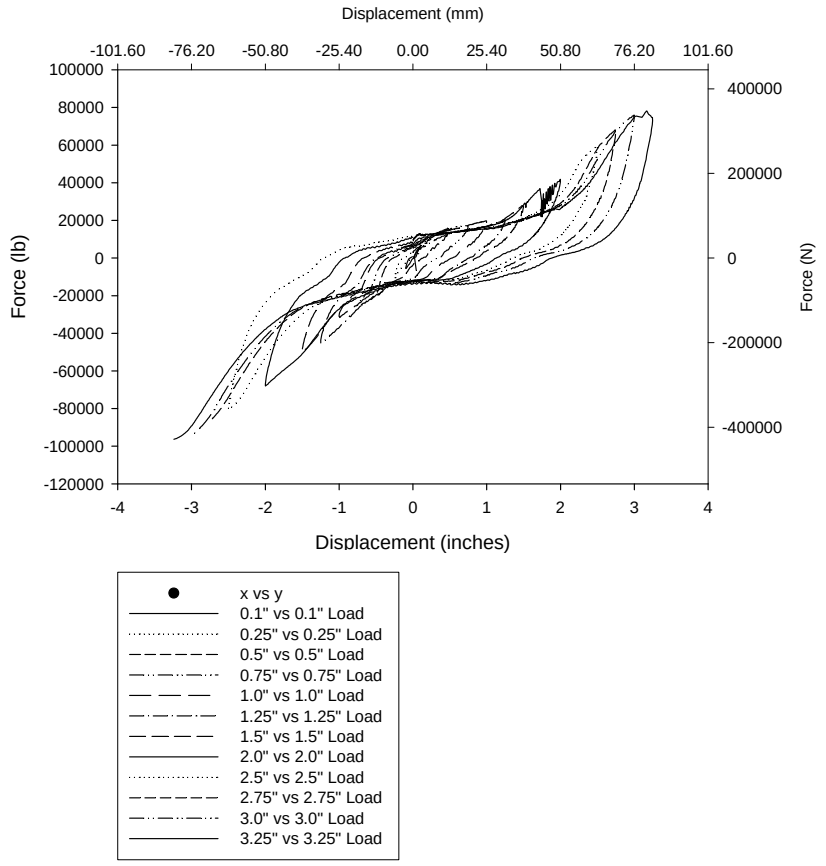

Figure A.6: Force-displacement relationships of 19" pedestals, weak-axis loading tests (P1-2)

A.3 P2-1 tall pedestals, loading about its strong-axis with welded angles

Phase II of the testing consists of testing the tall pedestals but with two different bolt configurations per different configurations observed on GDOT bridge plans and in the field. The arrangement of the anchor bolts for test P2-1 is similar to Phase I of testing the short pedestals, where the anchor bolts are engaged via L-shaped angles that are welded to the base plate of the pedestals and have slots within the angles for the bolts to be set. Test P2-2 consists of having the anchor bolts set within the cross-section. To this end, holes are pre-drilled into the base plate of the pedestals as to be aligned with the

anchor bolts once they have set in a grout that is placed into the holes of the reinforced concrete pier (Figure A.7).

Figure A.7: Photograph of as-built specimen for 33½" pedestals with welded angles, strong-axis loading (P2-1)

Results from the strong-axis bending tests of the tall pedestals loaded about its strong-axis revealed the pedestals to be quite flexible and stable members despite one of the potential vulnerabilities initially hypothesized with testing these taller sections under lateral loads. The tall pedestals are 33½" in height and consist of built-up steel members. For P2-1, the tall pedestals are oriented such that in-plane loading of the bridge specimen results in strong-axis bending of the pedestals. Shakedown, cyclic tests at +/- 0.1" are conducted and produce a linear, elastic response in the force-displacement relation

(Figure A.8). Very little energy is dissipated at +/- 0.1" displacement, where some of the energy dissipated can be attributed to friction in the system.

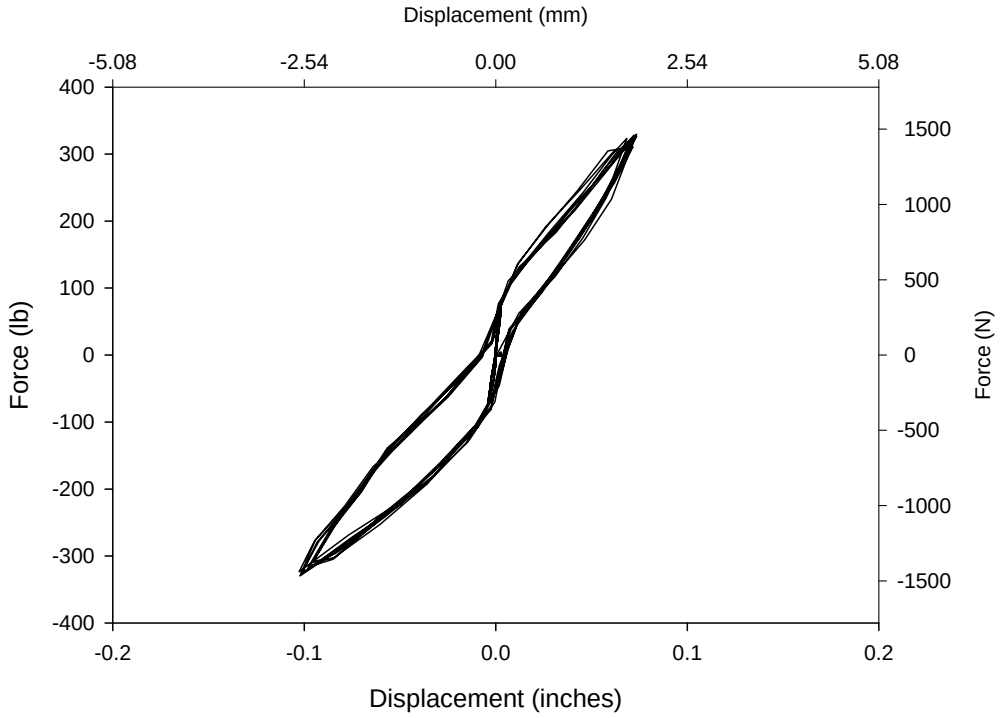

Figure A.8: Shakedown force-displacement relationship of 33½" pedestals with welded angles, strong-axis loading (P2-1)

With increased cycling, however, an increase in the stiffness degradation of the system is observed and reflected in the force-displacement relationships at +/- 0.5" and 0.8" displacements (Figure A.9). Since data is not captured for cycles between 0.1" and 0.5" displacements, the exact yield strain cannot be fully determined. However, strain hardening of the system is evident at 0.5" displacements as shown in the force-displacement hysteretic relationships. A nonlinear response of the pedestals is observed from 0.5" displacement until the peak displacement of 1.4" is executed. At +/- 0.5" displacements, approximately 18,500 lbs and -22,000 lbs are reached respectively. Sliding of the pedestals on the elastomeric (neoprene) pad is also observed and quantified

by the instrumentation as discussed in *Section 3.7*. Due to effects of sliding, the neutral axis and therefore center of rotation are changing. It can be said that the effects of this shift result in unsymmetric loading. Because of the force imbalance in the system, the pedestals are not rocking about its center of rotation and engaging the anchor bolts as load-carrying elements more so in compression loading (reloading) than in tension loading (initial direction of loading). With continued loading, the bolts seem to shift from resisting shear loads to resisting combined shear and tension loading as the anchor bolts are engaged when the pedestals lift-off the reinforced concrete pier during rocking. At +/- 0.8" displacements, loads of approximately 24,300 lbs and -28,000 lbs are reached. For cycling loading at 0.8" displacement, the hysteretic loop appears to be more symmetric about the tension and compression loading as if the bending about its neutral axis was restored. When the system is unloaded from the reloading cycle, in which data is captured in the compression region, a sudden increase in load at -0.4" displacements is observed. This effect can be attributed to the system trying to overcome forces of friction, perhaps from a region of crushed concrete had accumulated underneath the pedestals during loading. The peak loads of approximately 36, 800 lbs and 30,000 lbs occurred at +/- 1.4" displacements due to concrete breakout of unconfined concrete near the bolt edge of the reinforced concrete pier. The kink shown in the compression region at -1.4" displacement is evident of the loss of strength in the system during the concrete breakout. More details about the mechanisms that can lead to modes of failure in the system are discussed in *Section 4.2 Response Assessment of Bridge Steel Pedestals.*

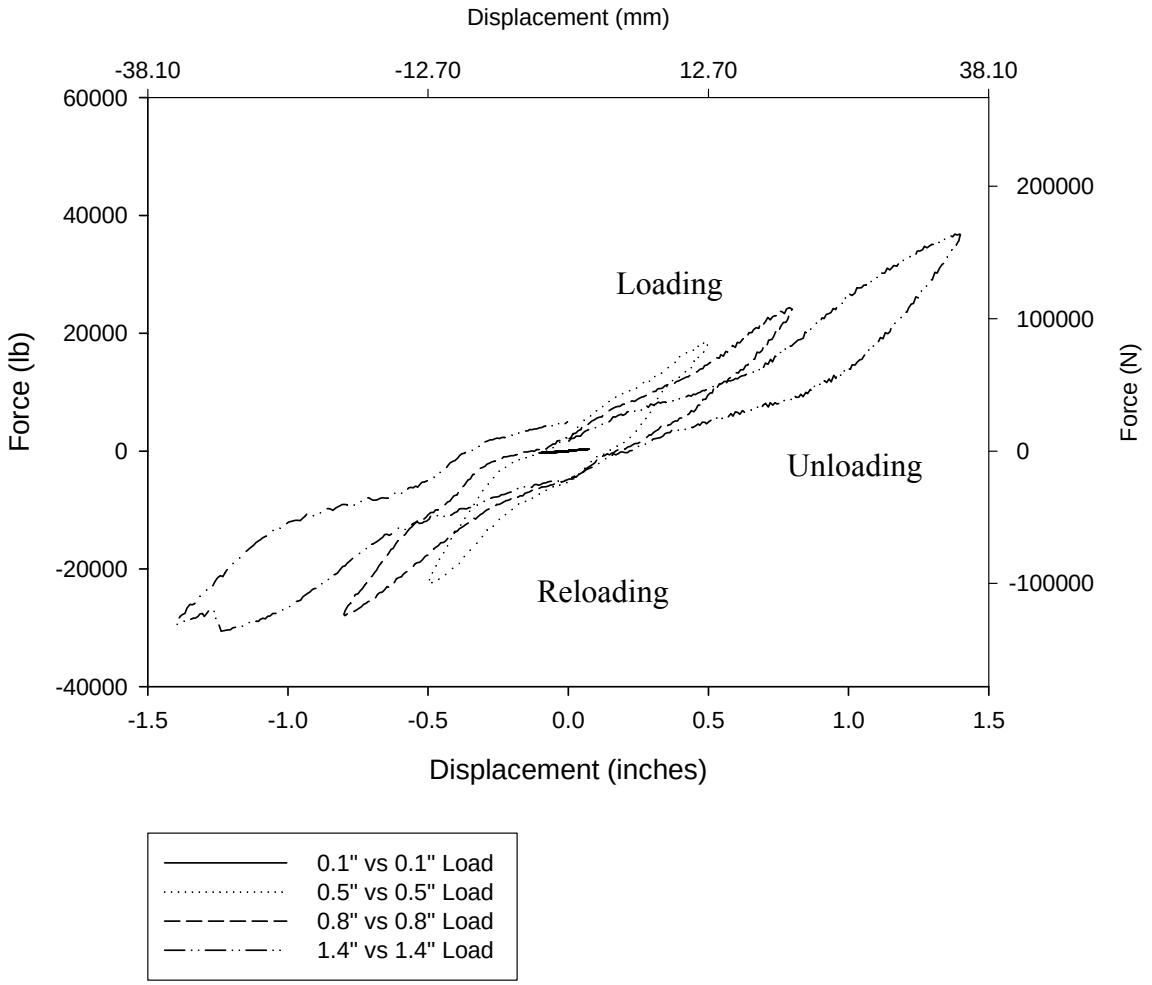

Figure A.9: Force-displacement relationships of 33½" pedestals with welded angles, strong-axis loading tests (P2-1)

A.4 P2-2 tall pedestals, loading about its strong-axis (bolts within pedestal base plate)

The second test within Phase II, referred to as P2-2, consists of loading the tall pedestals along its strong-axis but with the anchor bolts aligned with holes that are drilled into the pedestal base plate and set within the cross-section of the pedestals per field observations of pedestals installed on the George W. Thompson Sr. Memorial Bridge on Thornton Road over I-20 in Austell, Georgia (Figure A.10).

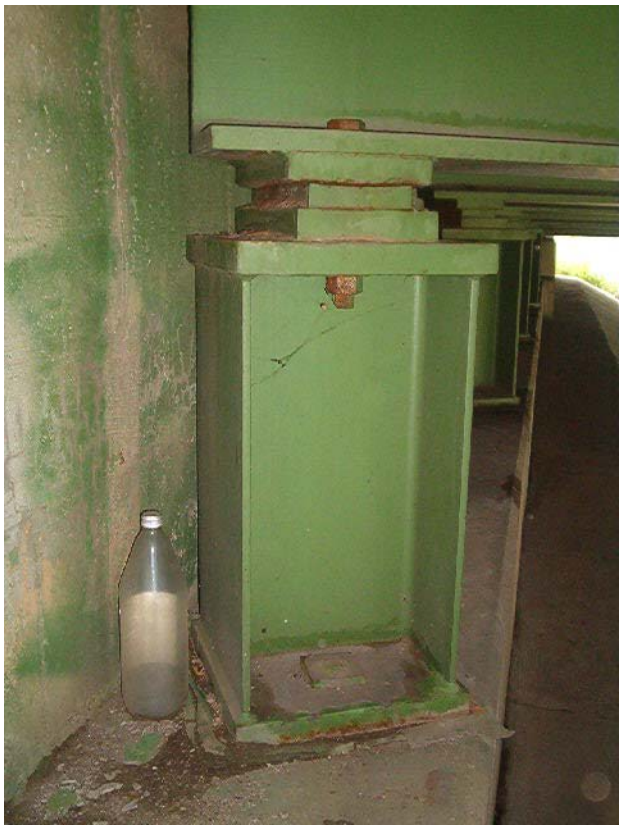

Figure A.10: George W. Thompson Sr. Memorial Bridge on Thornton Road over I-20 in Austell, Georgia rehabilitated with steel pedestals with bolts located within the cross-section

A photograph of the setup is shown in Figure A.11 with the tall pedestals connected to the bridge girders and reinforced concrete pier. Similar to all of the other tests, the 16" swedged stainless steel anchor bolts are embedded 12" into the reinforced concrete pier in a high-strength grout. The instrumentation used is the same as the previous tests, where the actuator is commanded in displacement-control. Having the anchor bolts located at the center of rotation of the pedestals provides better fixity of the system such that less sliding occurs at the onset of loading. In turn, the pedestals are able to rotate about the center of rotation and provide more deformation capacity within the

system. The force-displacement relationships are indicative of this behavior and are captured within the hysteretic loops at the prescribed target displacements.

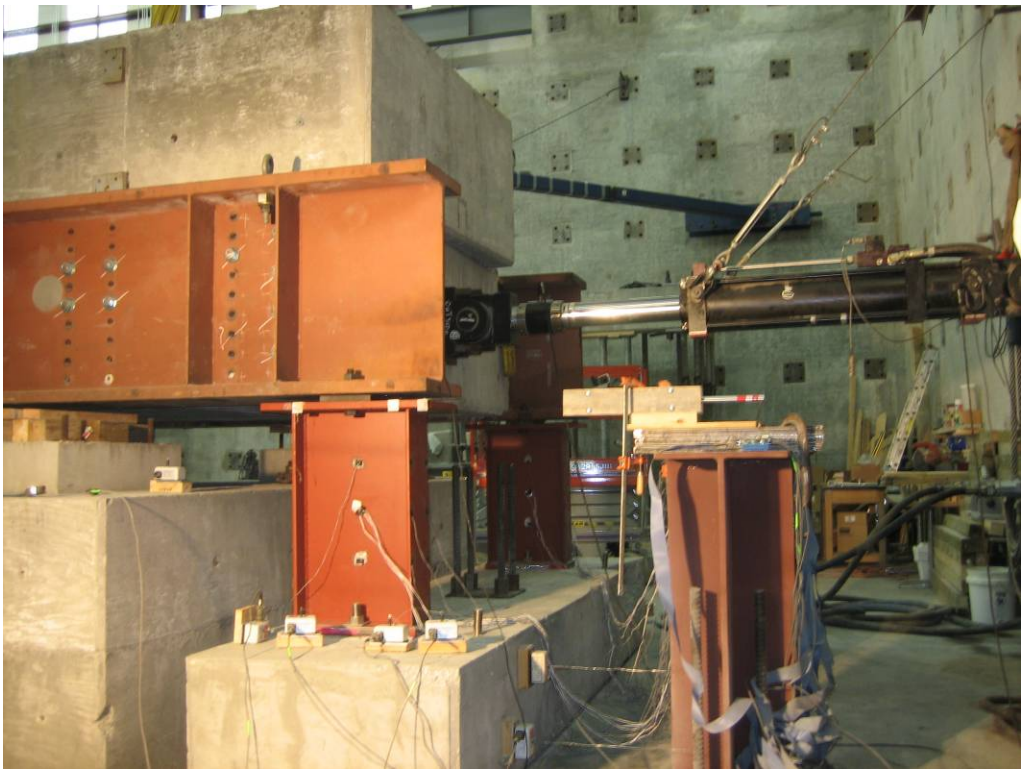

Figure A.11: Photograph of 33½" pedestals with bolts located within the pedestal base plate, strong-axis loading (P2-2)

Shakedown tests are conducted at 0.3" displacement to validate the linear, elastic response of the system. Friction can be attributed to the slight energy dissipated in the system at 0.3" displacement as shown in Figure A-12.

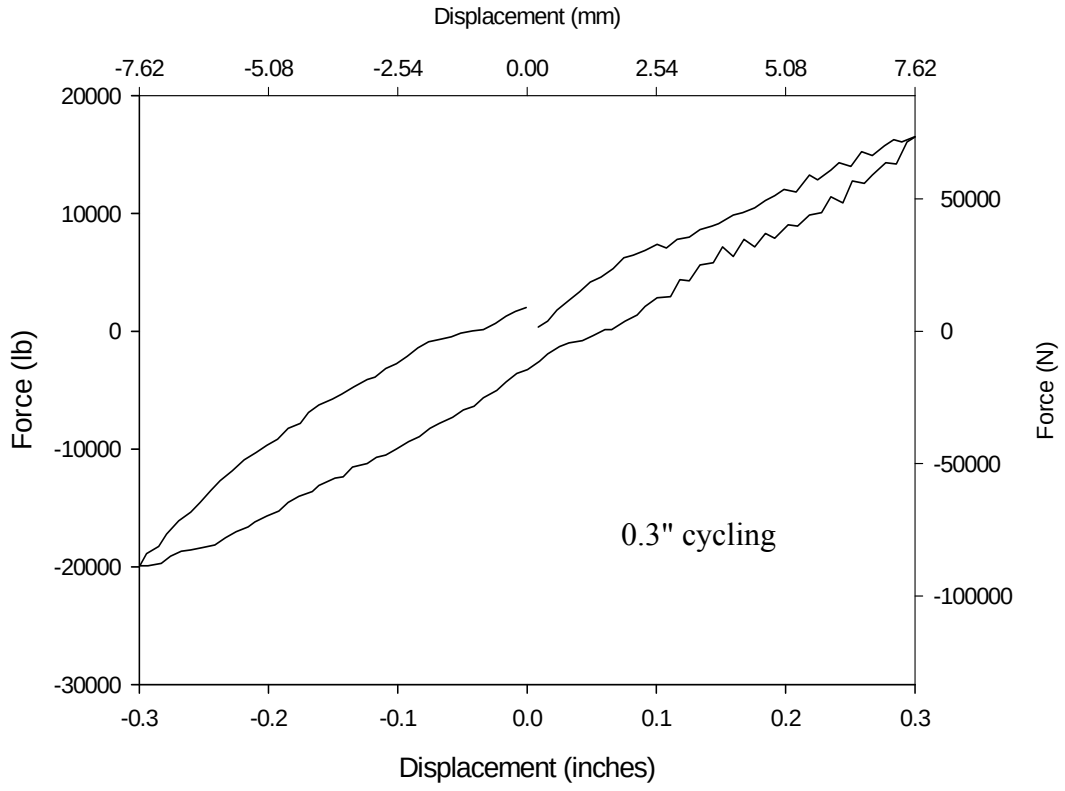

Figure A.12: Shakedown force-displacement relationships of 33½" pedestals with bolts located within the pedestal base plate, strong-axis loading (P2-2)

Additional cycling is continued at +/- 0.4" and 0.5" displacements. An initial yield occurs between +/- 0.5" and 0.75" cycling, where the response becomes nonlinear. Because the anchor bolts serve as a pivot point for the center of rotation, the hysteretic loops seem to rotate about a central point. The tension loading jumps from 16,577 lbs at 0.3" displacement to 21,436 lbs at 0.4" displacement. Stiffness degradation occurs with increased cycling, thereby revealing the nonlinear response. The deformation and load capacity continue to increase nonlinearly as the system continues to rock about is center

of rotation. The nuts of the bolts loosen with increased cycling. Starting at +/- 2.5" displacement, a noticeable amount of sliding is observed. It is believed to occur as a result of the shear resistance provided by the anchor bolts that resist load and also prying action of the bolt from within the reinforced concrete pier. The peak displacements of P1-1, P1-2 and P2-1 were exceeded even at the target displacement for 2.5" for test P2-2. At 2.5" displacement, the tension loading is approximately 50,380 lbs. Cycling continues until a peak displacement of 3.5" is reached when the top plate of the pedestal rotates such it almost touches the underside of the girder (Figure A.13). Loads of nearly 55,000 lbs in tension loading and 60,000 lbs in compression loading are reached at the peak displacement of 3.5" (Figure A.14). As a result, test P2-2 allowed for the maximum angle of rotation in all of the tests conducted (more details found in *Section 4.2 Response Assessment of Bridge Steel Pedestals*). The bolt arrangement along the neutral axis supports the notions that more flexibility can be achieved when the bolts are configured in this manner. Along with the increased flexibility, there is an increase in the deformation and load capacity of the specimen as peak displacements of +/- 3.5" and loads of almost 60,000 lbs.

Figure A.13: Bolts located at neutral axis and center of rotation

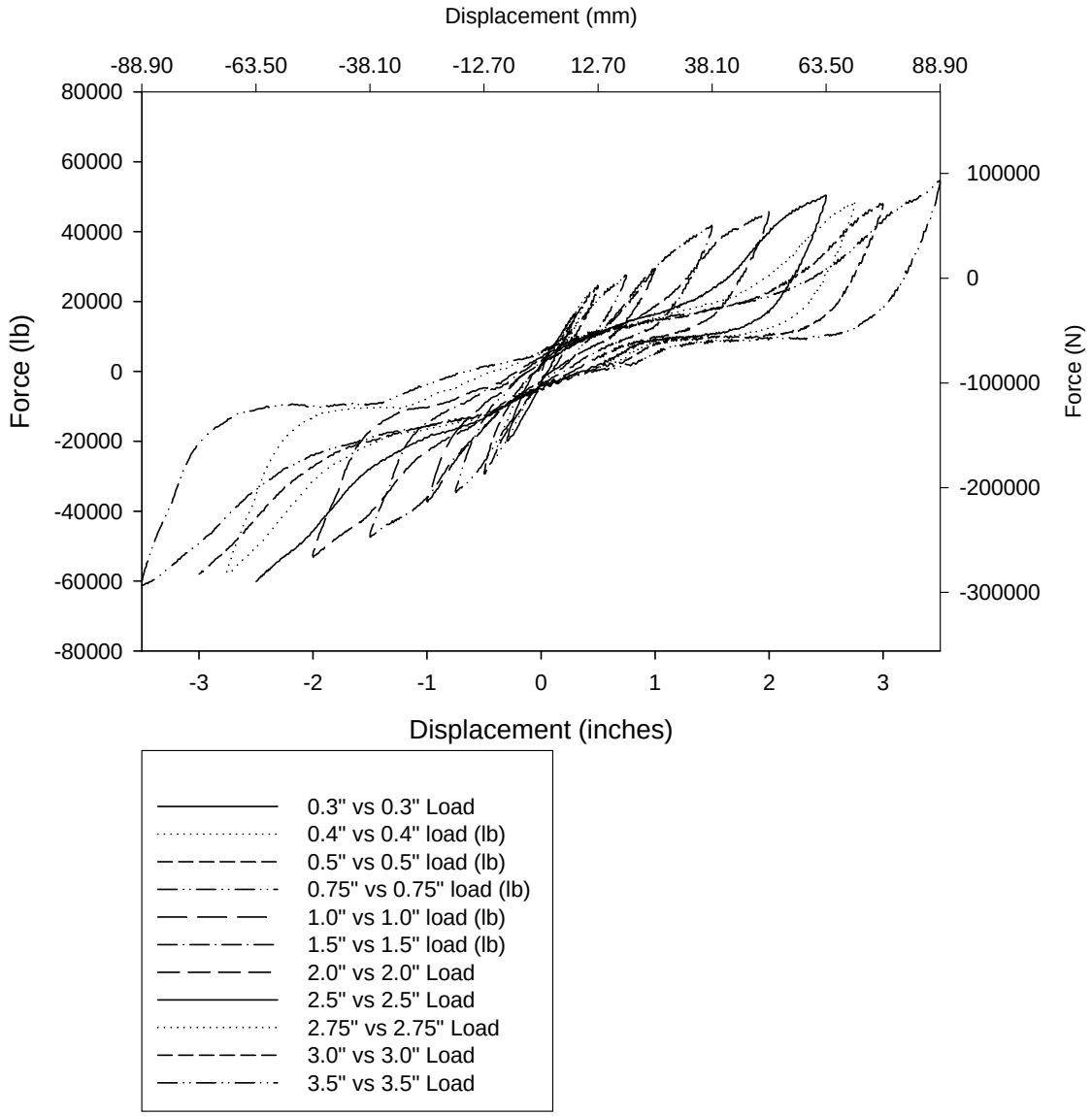

Figure A.14: Force-displacement relationships of 33½" pedestals with bolts within the pedestal base plate, strong-axis loading (P2-2)

A.5 P3-1 tall pedestals, loading about its weak-axis with welded angles

Similar to Phase II, Phase III consists of testing the tall pedestals with two different bolt configurations but loaded along its weak-axis. For the weak-axis testing, four (4) A490 ¾"-diameter bolts were used to connect each pedestal to the girders. Finger shims were used between the pedestals and anchor bolts for better contact. Intermediate plates were not used between the pedestals and girders in this phase of testing. Without these intermediate plates, a "stiffer" connection was established to minimize the slip and provide better contact for transmitting the forces from the superstructure to the pedestals. An MTS 243.35 85-kip capacity hydraulic actuator was used for Phase III compared to the MTS 243.45 150-kip actuator used for Phases I and II.

As stated in Phase II of testing, the two different bolt configurations used for testing are based on various configurations observed in the field on bridges that GDOT has rehabilitated with steel pedestals. The arrangement of the anchor bolts for test P3-1 is similar to test P1-1 and P2-1, where L-shaped angles with slot holes for the anchor bolts are welded to the base plate of the pedestal. As such, results from test P3-2 show how the tall pedestals loaded along its weak-axis behave when the anchor bolts are positioned within the cross-section of the pedestal. The construction procedures in for test 3-2 are similar to that of test 2-2, where the holes within the base plate of the pedestal are pre-drilled. Careful measurements are taken to position the anchor bolts for proper alignment on the pier and between the centerlines of the girders.

A small W24x80 spreader beam shown in Figure A.15 is attached to the concrete block wedged between the girders to adapt the dimensions of the smaller swivel head of the actuator to the setup. This is a minor adaptation to the setup with the actuator still

providing adequate capacity for testing. Testing in Phase III occurs at a slower loading rate of 1 inch per minute due to some tuning issues experienced with the 85-kip actuator. Loading about the weak-axis and therefore, much smaller moment of inertia, may result in potential instabilities of the system. However, the force-displacement hysteretic relationships acquired from quasi-static tests show the response and magnitude of forces that are resisted by the system given the configuration.

Figure A.15: Photograph of as-built specimen with 33½" pedestals with welded angles, weak-axis loading (P3-1)

Shakedown tests for P3-1 are conducted at 0.1" displacement. Some noise is observed in the force-displacement relations at 0.1" cycling, although the hysteretic loop reveals a linear, elastic response. An initial yield occurs between 0.1" and 0.5"

displacement, where the response becomes nonlinear. From the force-displacement relationships, it can be inferred that the response seems to dissipate a seemingly constant amount of energy throughout the cycling. At 0.5" displacement, loads of almost 22,500 lbs are resisted by the system (Figure A.16). Cycling continues where strain hardening occurs around 0.5" displacement and increases until peak displacement of 2.0" is reached. At -1.5" displacement (compression loading or reloading of the specimen) and approximately -40,000 lbs, there is a breakout of the concrete (Figure A-17). A kink in the force-displacement reflects this observation at -1.5" displacement (Figure A-18). Testing is stopped because the actuator began to resonate due to some tuning related issues. However, the pedestals did reveal to be stable elements during loading. With increased cycling, prying action of the bolts occurs. Since the anchor bolts are aligned with the neutral axis of the pedestals, symmetric loading of the system is enabled and peak loads of approximately 53,000 lbs are reached.

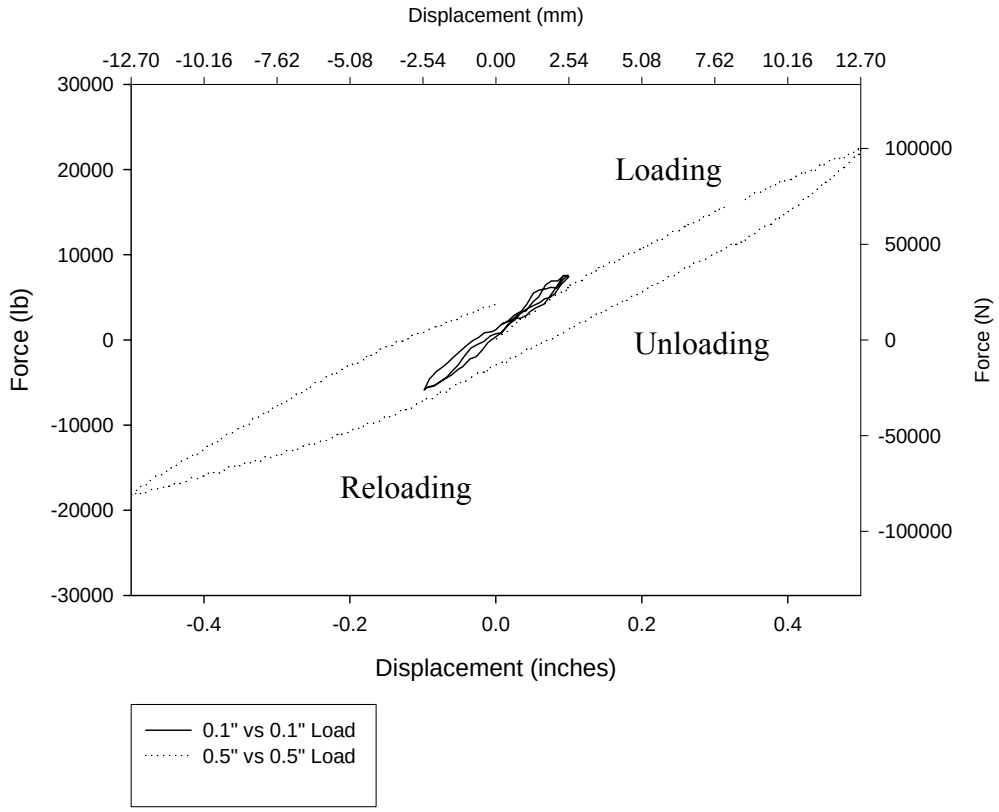

Figure A.16: Shakedown force-displacement relationships of 33½" pedestals with welded angles, weak-axis loading (P3-1)

Figure A.17: Surface spalling of the concrete during compression loading for test P3-1

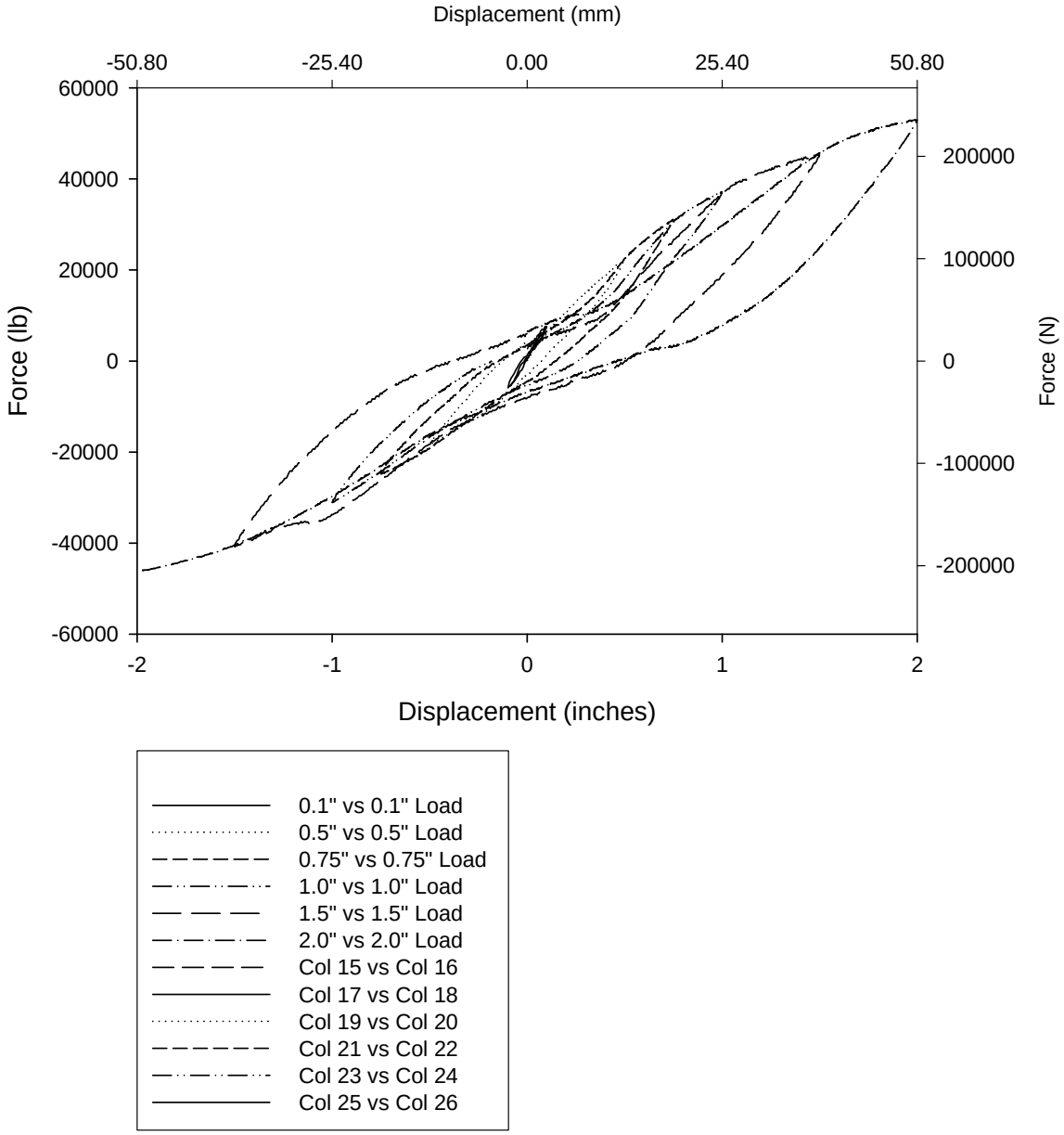

Figure A.18: Force-displacement relationships of 33½" pedestals with welded angles, weak-axis loading tests (P3-1)

A.6 P3-2 short pedestals, loading about its weak-axis (with bolts within the pedestal base plate)

The sixth and final test of the testing series, P3-2, is conducted on the tall pedestals with the anchor bolts positioned within the pedestal cross-section like test P2-2 (Figure A.19). Construction procedures are similar to that expressed in test P2-2. The bolts are aligned at the neutral axis, which also happens to be in line with the center of rotation. Shakedown tests are conducted at 0.2" displacements to reveal the linear, elastic response at small displacements (Figure A.20). The specimen is loaded with the MTS 243.35 actuator in displacement-control at a rate of 1" per minute.

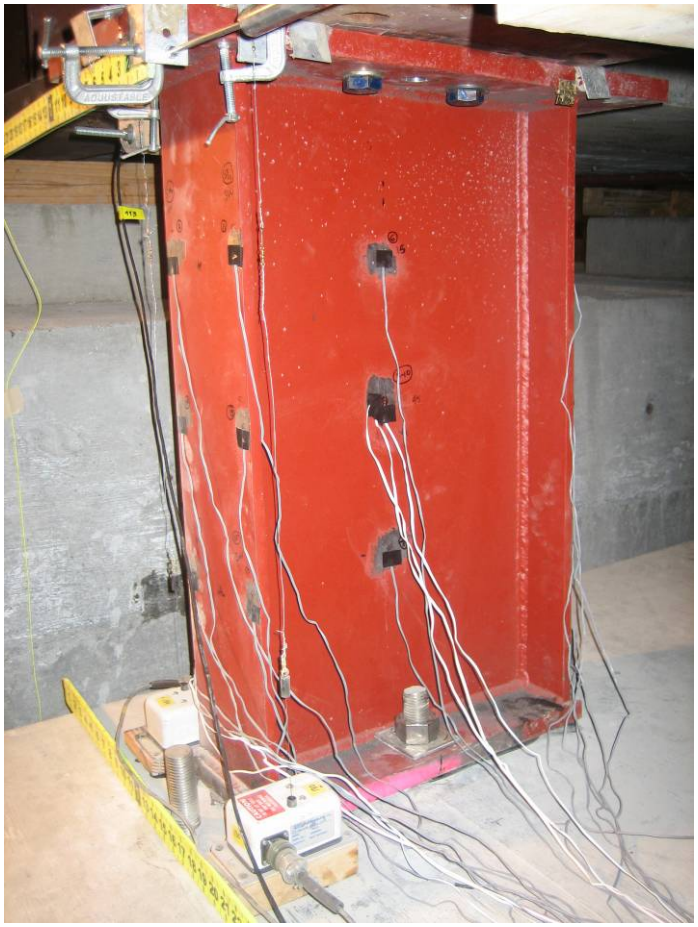

Figure A.19: Photograph of as-built specimen with 33½" pedestals with bolts located within the pedestal base plate, weak-axis loading (P3-2)

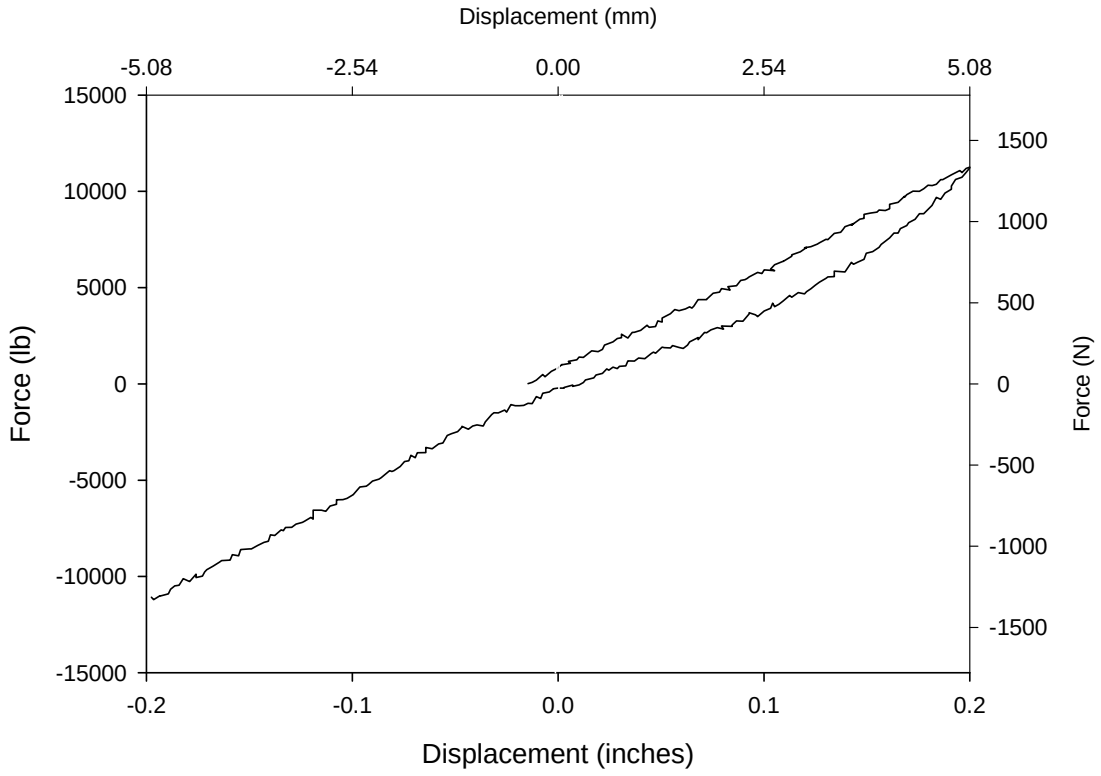

Figure A.20: Shakedown force-displacement relationships of 33½" pedestals with bolts located within the pedestal base plate, weak-axis loading (P3-2)

At 0.2" displacement, the load is quite large, yet still resulting in a linear response even around 10,000 lbs. After the shakedown tests are conducted at 0.2" displacement, the specimen is loaded to reach displacements of +/- 0.5". An initial yield occurs between 0.2" and 0.5" displacement. The hysteretic behavior of test P3-2 is quite similar to test P3-1 with similar peaks reached for the deformation and load capacity of the specimen (Figure A.21). With increased cycling, stiffness of the system response degrades. Sliding of the pedestals is not apparent. Again, with having the bolts close to the center of rigidity, the specimen is stiffer thereby really only allowing the pedestals to rotate about its center of rotation. Consequently, a symmetric loading response in tension and compression is also reflected in the hysteresis loops. The anchor bolts undergo prying

action as the pedestals rock back and forth given the loading, unloading, and reloading of the specimen. At -1.5" displacement, surface spalling of the concrete due to large compression loads is experienced by the specimen and shown in Figure A.22. Slight stiffness of the system response is lost and revealed by the kink around -1" displacement during the -1.5" displacement loading cycle.

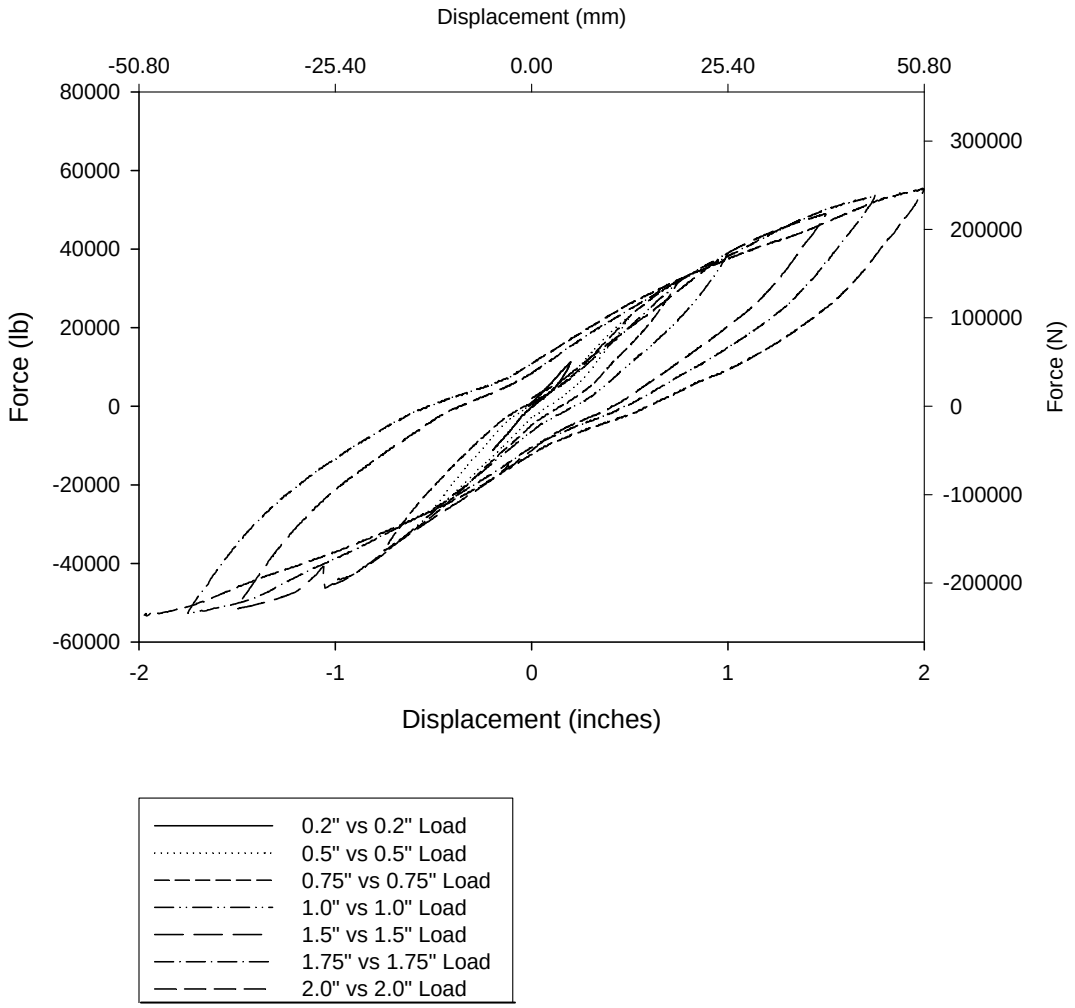

Figure A.21: Force-displacement relationships of 33½" pedestals with bolts located within the pedestal base plate, weak-axis loading (P3-2)

A.7 Comparison of Shear Forces in System

Basic mechanics are used to compute the horizontal loads in the system so that the shear in the pedestals can be directly compared to the load recorded from the actuator. Figures A.22 through A.27 compare the horizontal loads inferred from the strain gauges to the applied loads from the actuator. Ideally, the two loads should be approximately equal to each other. Slightly better approximations exist when the bridge specimen is loaded in tension compared to compression loading.

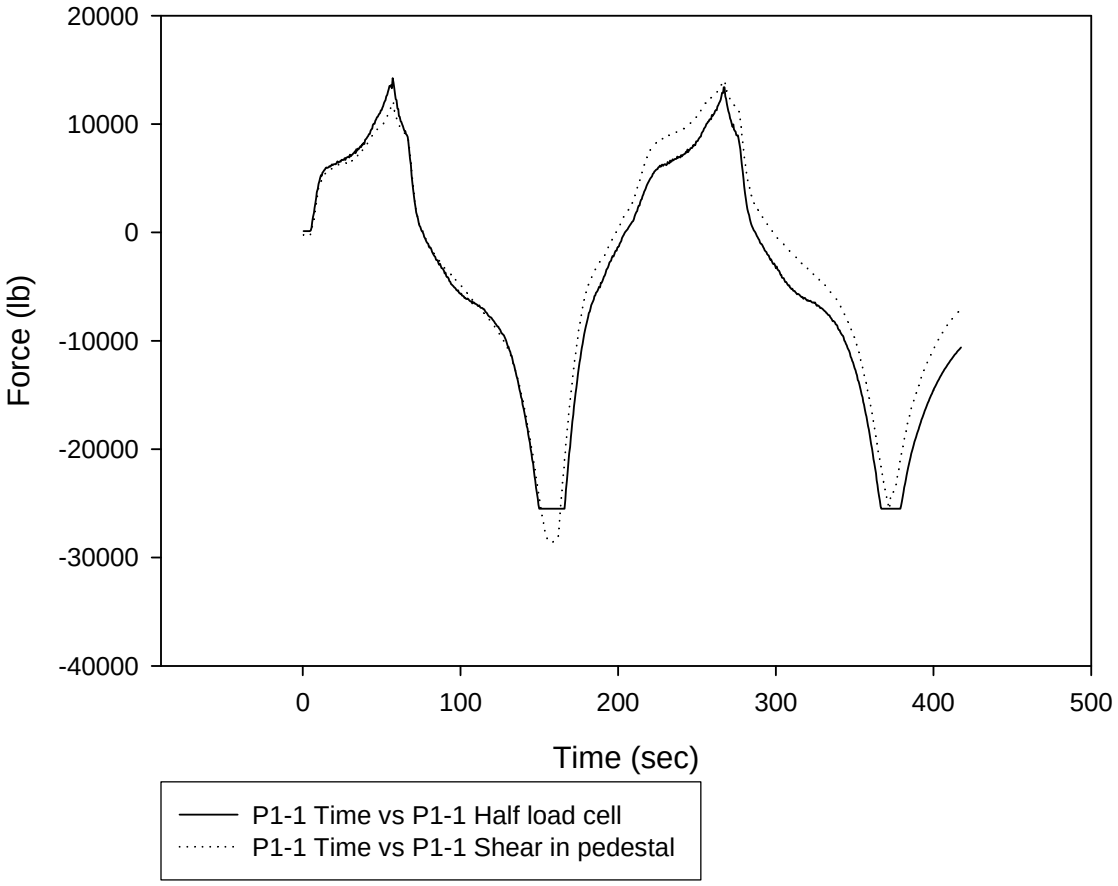

Figure A.22: Comparison of horizontal loads in bridge system for test P1-1

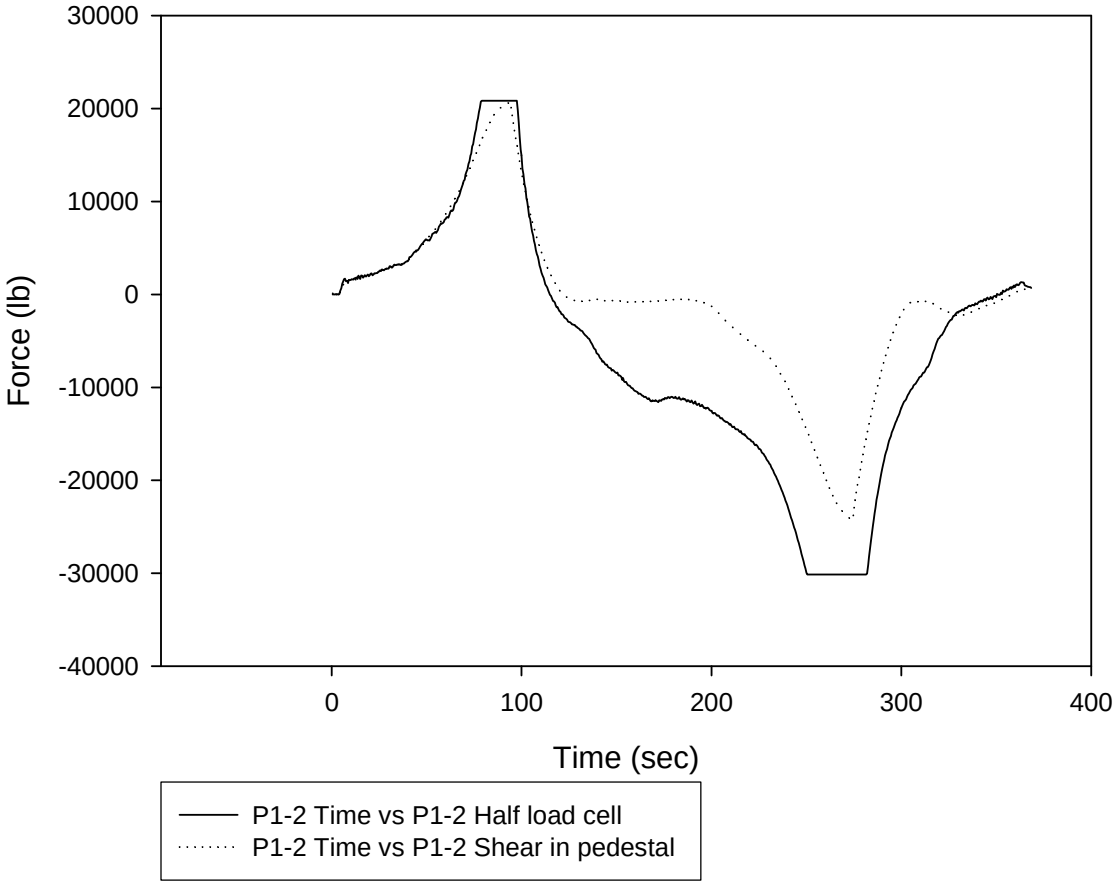

Figure A.23: Comparison of horizontal loads in bridge system for test P1-2

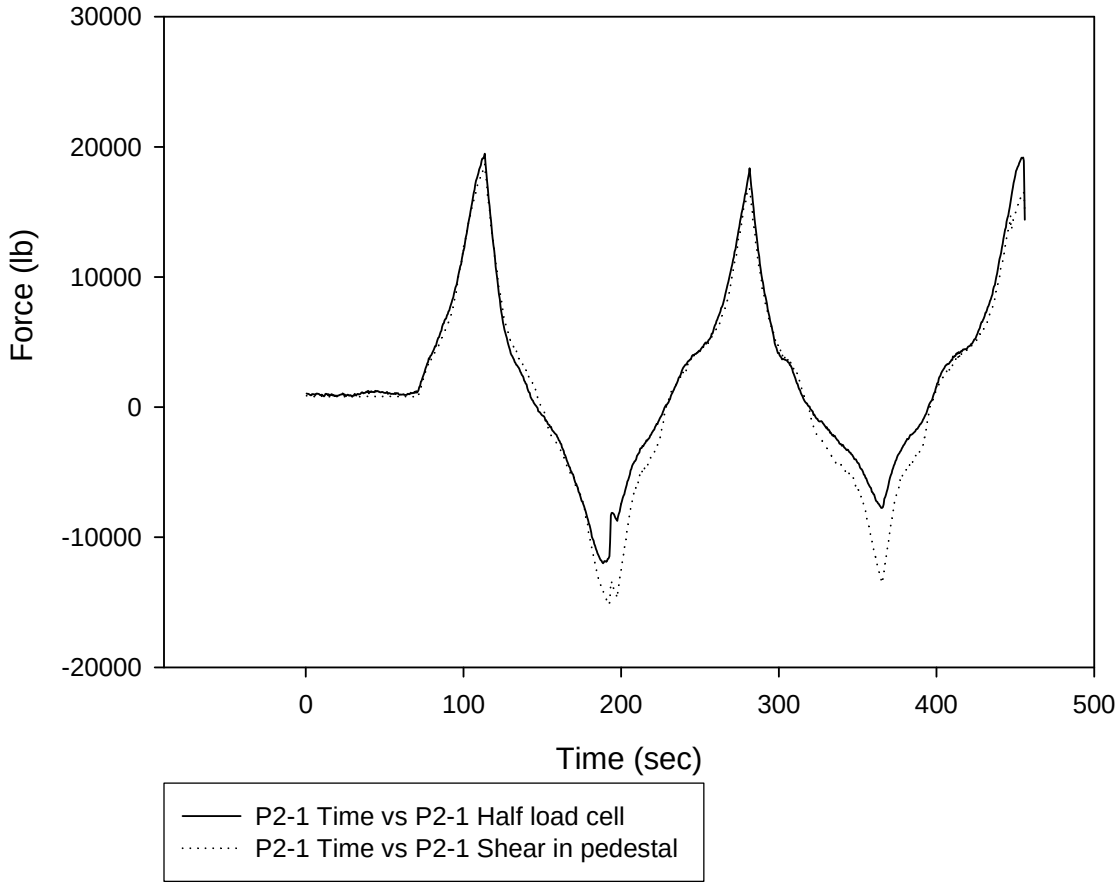

Figure A.24: Comparison of horizontal loads in bridge system for test P2-1

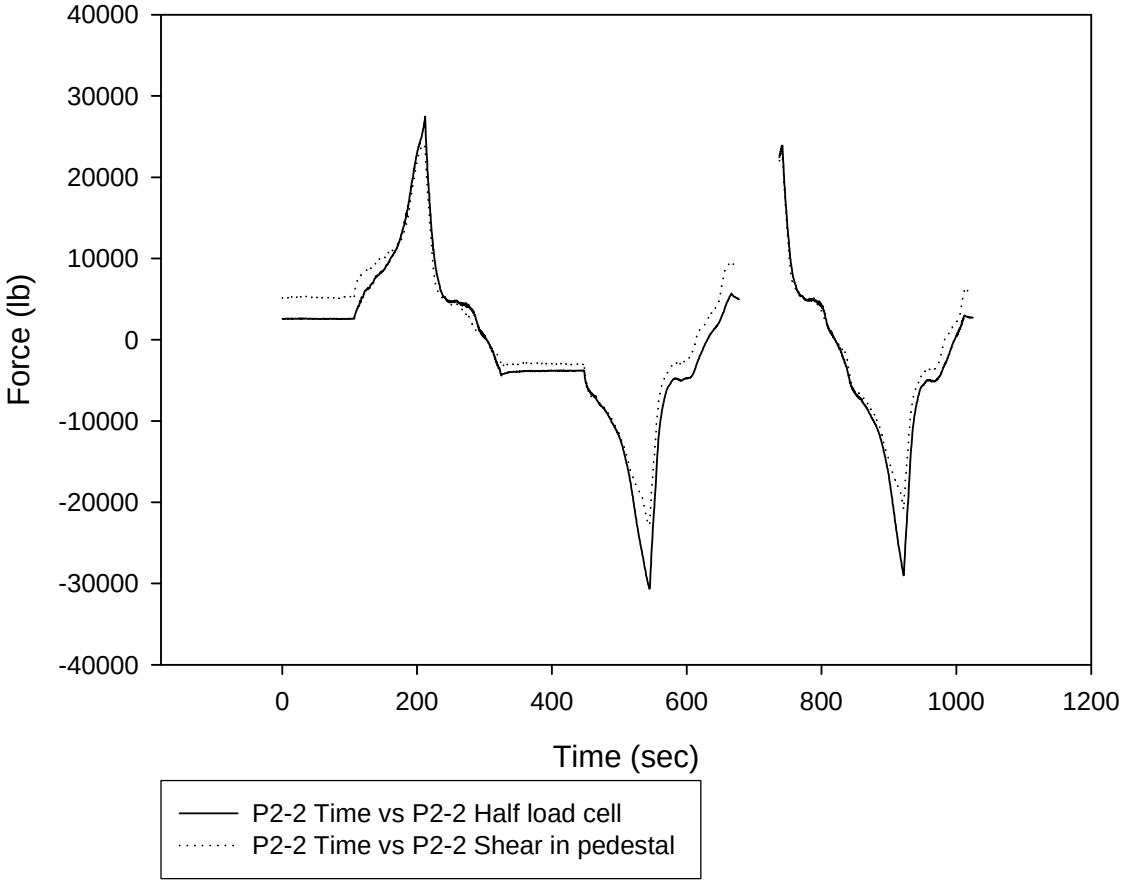

Figure A.25: Comparison of horizontal loads in bridge system for test P2-2

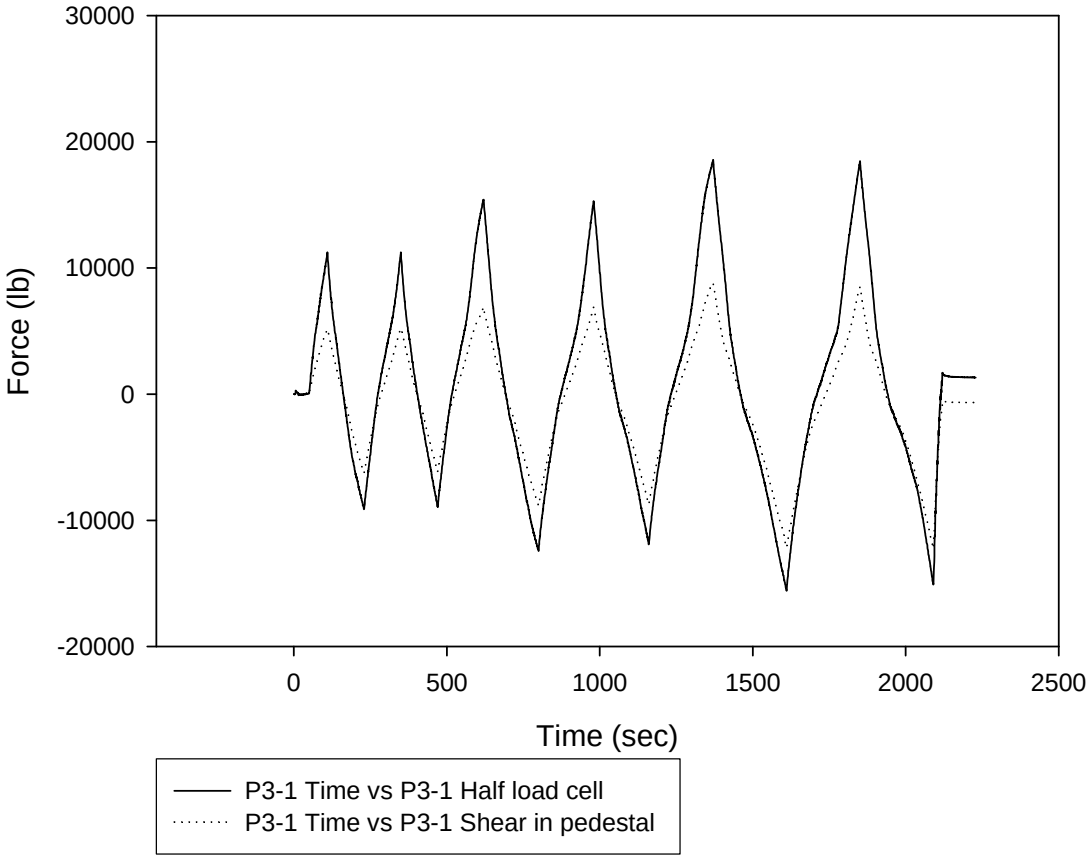

Figure A.26: Comparison of horizontal loads in bridge system for test P3-1

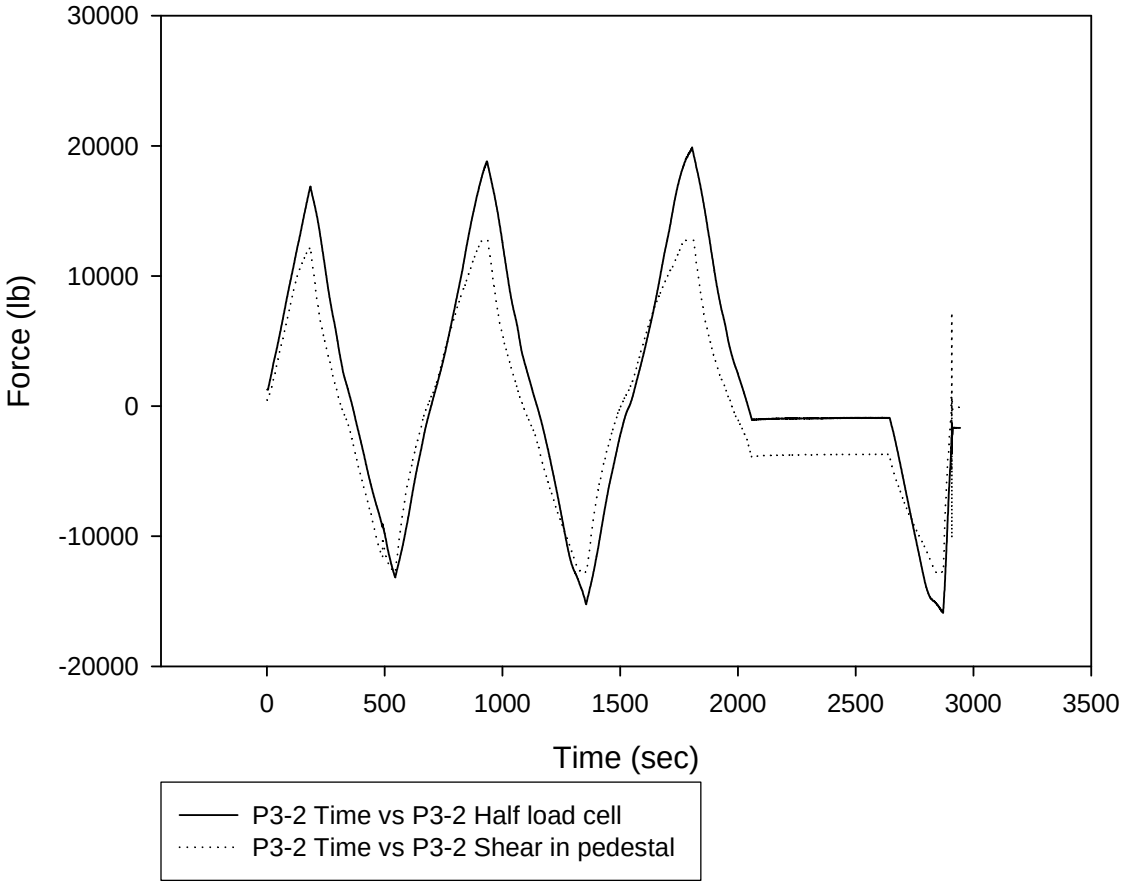

Figure A.27: Comparison of horizontal loads in bridge system for test P3-2

A.8 Effective Stiffness of Steel Pedestals

The test data is also compared in terms of its effective stiffness, amount of energy dissipated, equivalent viscous damping, and residual and relative displacement of the first cycle. The effective stiffness resulting from the force-deformation hysteresis is computed from the coordinates of the peak load and corresponding displacement as shown in Eq. A.1.

$$K_{eff} = \frac{Force_{\max} - Force_{\min}}{\Delta_{@\,Force_{\max}} - \Delta_{@\,Force_{\min}}} \tag{A.1}$$

A.9 Energy Dissipation of Steel Pedestals

From the force-displacement relationships (*Section 4.1*), the hysteresis loops show how much energy is dissipated by the pedestal compared to the input energy. The amount of energy dissipated can be computed by calculating the area under the hysteresis curve and dividing it by the total area of an assumed rigid-plastic force-deformation behavior or rectangular area. The percent of the energy dissipated is calculated by multiplying the ratio by 100 for the first cycle of each target displacement as shown in Eq. A.2. In general, less energy is dissipated with increased cycling. However, from the experimental test results, a mechanism (overcoming friction forces, etc.) must have been encountered such that there is an increase in the amount of energy dissipated with increased cycling. At the peak displacements for test P1-1 and P1-2 for the short pedestals, both tests dissipated about the same amount of energy between 18-20%. For the tall pedestals loaded about its strong-axis, about 12% of energy is dissipated at the peak displacements for test P2-1 and P2-2 despite the -150% difference in peak displacements reached for those tests.

$$E_D(\%) = \frac{\int_{\Delta_{min}}^{\Delta_{max}} P(\delta)d\delta}{Area} 100\% \qquad \text{(A.2)}$$

4.10 Equivalent Viscous Damping of Steel Pedestals

The equivalent viscous damping, ς_{eq}, shown in Eq. A.3 is a function of the maximum strain energy and the amount of energy dissipated as calculated in Eq. A.2, assuming the forcing frequency equals the natural frequency of the system ($\omega = \omega_n$). For this series of testing, Eq. A.2 is a satisfactory approximation of the equivalent viscous damping for the steel pedestals (Chopra, 2001). The upper bound of the range of values, 5-22%, for the estimated equivalent viscous damping shows the pedestals to be seemingly effective energy dissipation devices.

$$\zeta_{eq} = \frac{1}{4\pi}\frac{E_D}{E_{so}} \quad \text{, where} \quad E_{so} = \frac{1}{2}k\Delta_{max}^{\ 2} \qquad \text{(A.3)}$$

A.11 Residual Displacements of Steel Pedestals

The residual displacements are computed to show how much permanent strain is apparent in the system as a result of the force-deformation behavior. The residual displacement is calculated by locating the zero crossing when the specimen is transitioning from loading to unloading as part of the reversed, cyclic unidirectional loading that is applied via the MTS actuator. A physical representation of residual displacement is defined in Figure A.28. Table A.1 shows the residual displacements for the first cycle for all test data at the target displacements. In test P1-1 and P1-2, the

residual displacements are quite significant relative to the overall displacement and sliding that occurs in the system.

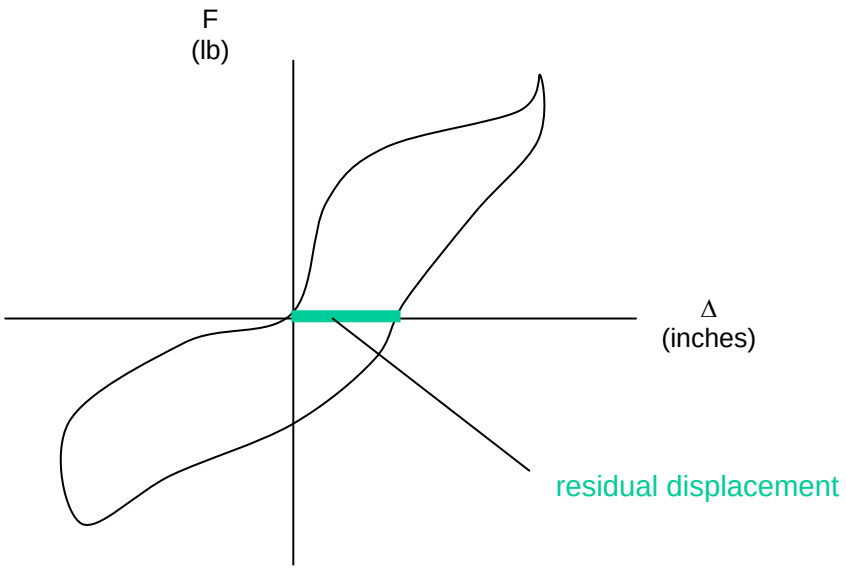

Figure A-28: Residual displacement apparent in hysteresis

Table A.1: Comparison of residual displacements for all test data at the target displacements

Target Δ (inches)	P1-1 6-6-2005 150k actuator (strong-axis)	P1-2 6-11-2005 150k actuator (weak-axis)	P2-1 11-21-2005 150k actuator (strong-axis)	P2-2 12-7-2005 150k actuator (strong-axis)	P3-1 5-3-2006 85k actuator (weak-axis)	P3-2 5-5-2006 85k actuator (weak-axis)
0.2	0.0796					
0.4						
0.5	0.3949	0.1375	0.13542	0.085803	0.0755	0.081659
0.75	0.6471	0.3432			0.1478	0.14471
0.8			0.16747			
1.0	0.6544	0.5355			0.2574	0.21810
1.4			0.22433			
1.5	0.9197	0.8673		0.20779	0.504427	0.41449
1.75	1.1276					0.4858
2.0		1.1351		0.28222	0.47445	0.5923
2.5		1.3594		0.38353		
2.75		1.4917		0.37113		
3.0		1.6468		0.43005		
3.25		1.8835				
3.5				0.48381		

A.12 Relative Displacements of Steel Pedestals

Lastly, the relative displacements are computed to show how much residual displacement exists compared to the maximum or target displacement. The relative displacement is calculated by dividing the residual displacement by the maximum or target displacement, and then multiplying by 100 to yield the relative displacement expressed as a percentage. Table A-6 shows the relative displacements for the first cycle for all test data at the target displacements (Eq. A.4).

$$\Delta_{relative}(\%) = \frac{\Delta_{residual}}{\Delta_{\max}} 100\% \tag{A.4}$$

Table A.2: Comparison of relative displacement percentages for all test data at the target displacements

Target Δ (inches)	P1-1 6-6-2005 150k actuator (strong-axis)	P1-2 6-11-2005 150k actuator (weak-axis)	P2-1 11-21-2005 150k actuator (strong-axis)	P2-2 12-7-2005 150k actuator (strong-axis)	P3-1 5-3-2006 85k actuator (weak-axis)	P3-2 5-5-2006 85k actuator (weak-axis)
0.2	40.036					
0.4				17.343		
0.5	79.035	27.518	27.048	17.173	15.087	16.327
0.75	86.425	45.709		0	19.728	19.2877
0.8			20.948			
1.0	65.506	53.605		9.3976	25.727	21.801
1.4			16.035			
1.5	61.3	57.849		13.84	33.635	27.658
1.75	64.429					27.764
2.0		56.764		14.099	23.722	29.615
2.5		54.376		15.341		
2.75		54.221		13.49		
3.0		54.887		14.328		
3.25		57.964				
3.5				13.82		

A.13 Sliding and Rocking (rigid body kinematics)

The sliding and rocking from the short and tall pedestal test results are normalized to the overall displacement in based on the peak displacement for each test. Time history plots of the sliding and rocking as a function of time are shown in Figures A.29 to A.40. The LVDT contracts at the onset of loading such that the pedestal is being pushed in the direction of loading as it slides on the elastomeric (neoprene) pad.

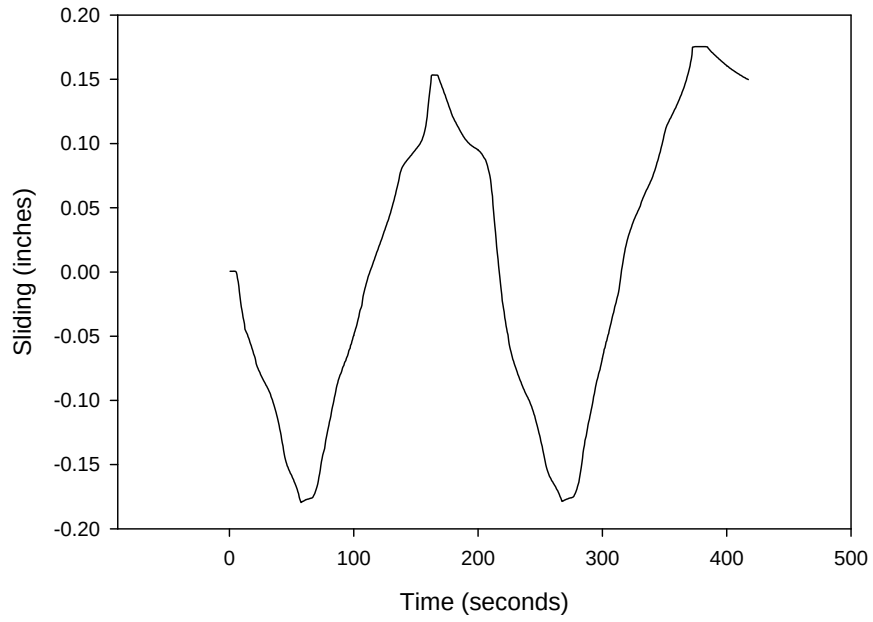

Figure A.29: Normalized relative movement (sliding) between the pedestal base plate and cap beam in test P1-1

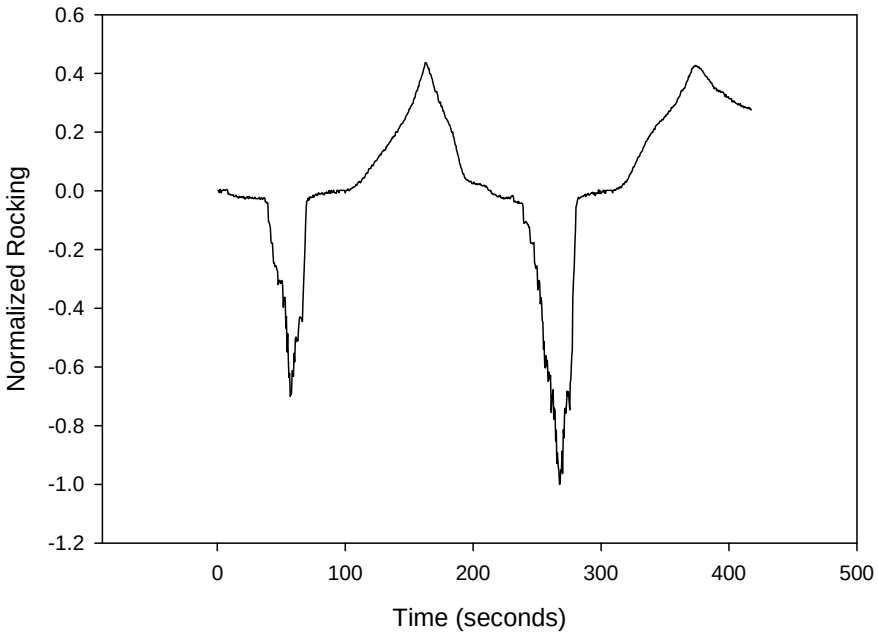

Figure A.30: Normalized rocking of pedestal in test P1-1

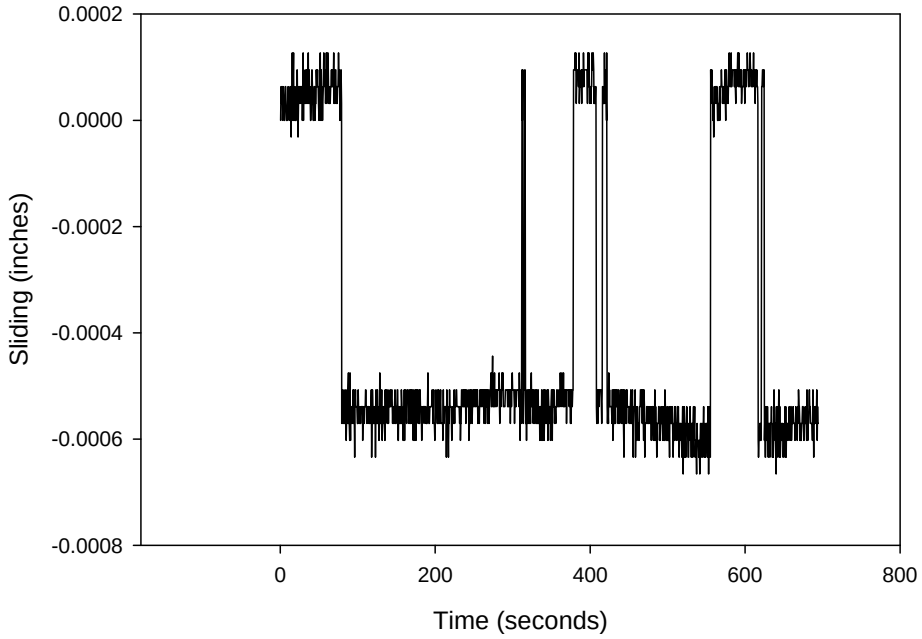

Figure A.31: Normalized relative movement (sliding) between the pedestal base plate and cap beam in test P1-2 (LVDT began out of range so no quantifiable data captured)

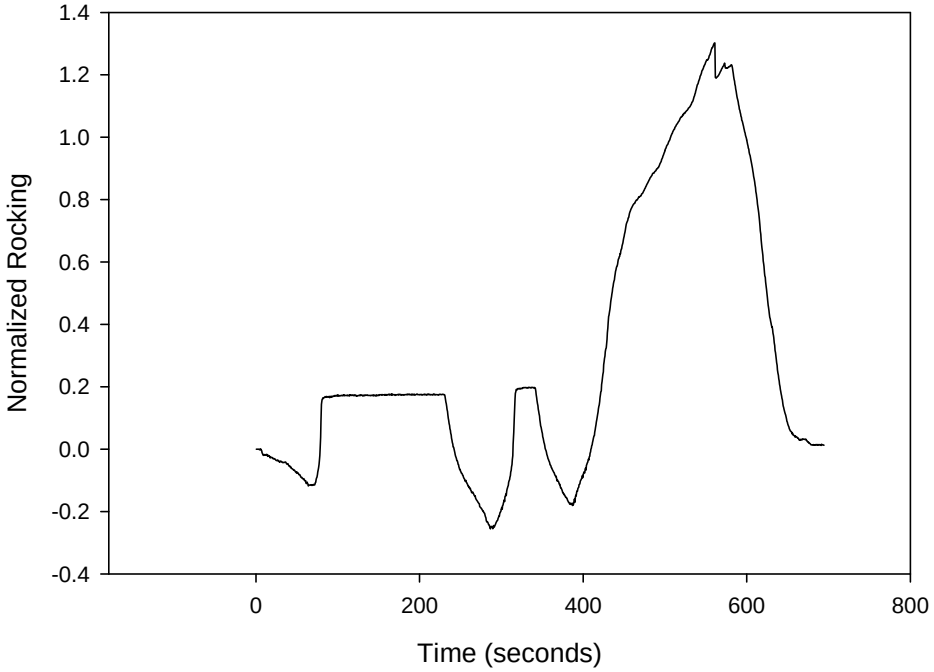

Figure A,32: Normalized rocking of pedestal in test P1-2

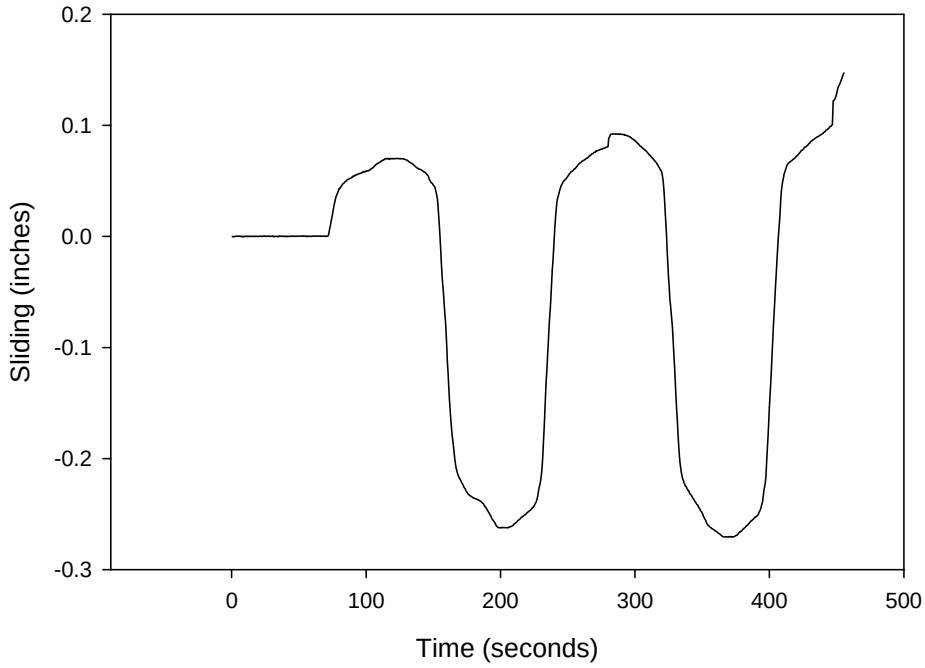

Figure A.33: Normalized relative movement (sliding) between the pedestal base plate and cap beam in test P2-1

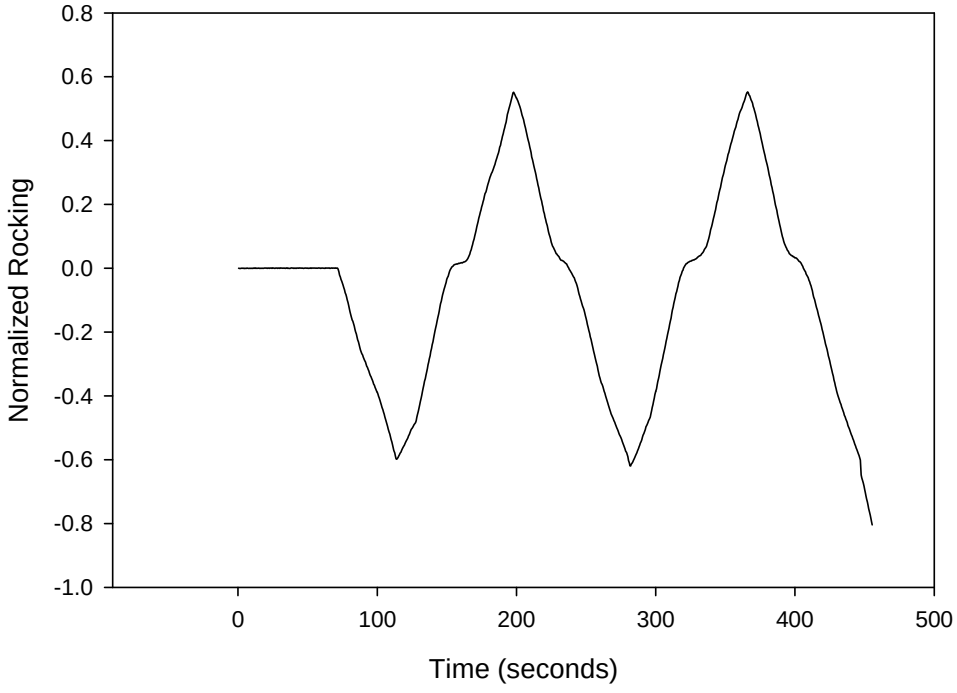

Figure A.34: Normalized rocking of pedestal in test P2-1

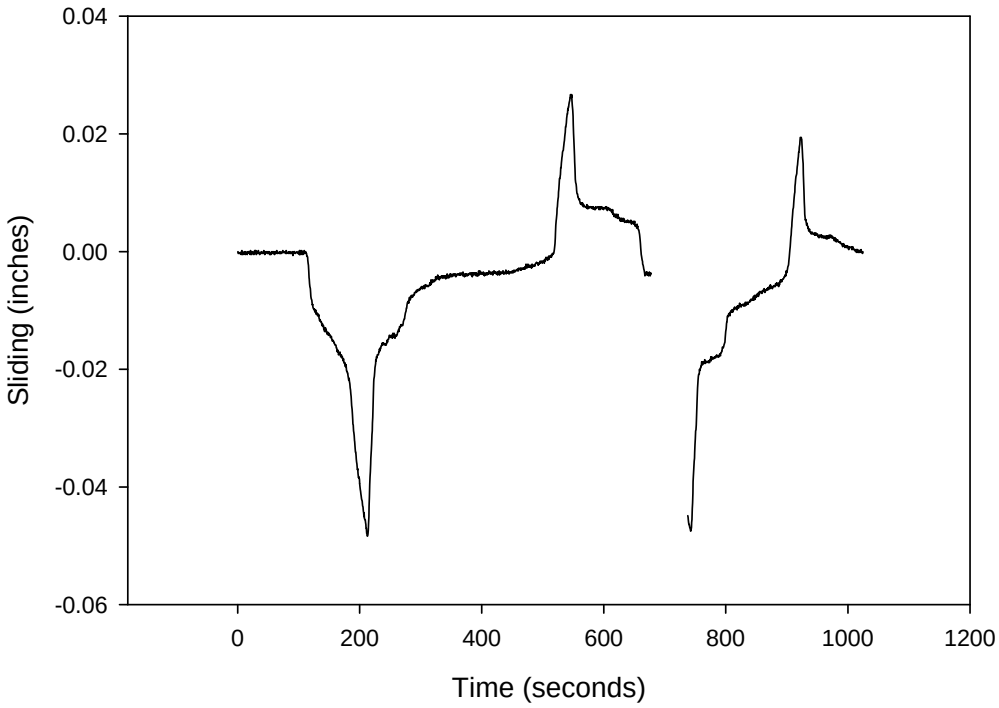

Figure A.35: Normalized relative movement (sliding) between the pedestal base plate and cap beam in test P2-2

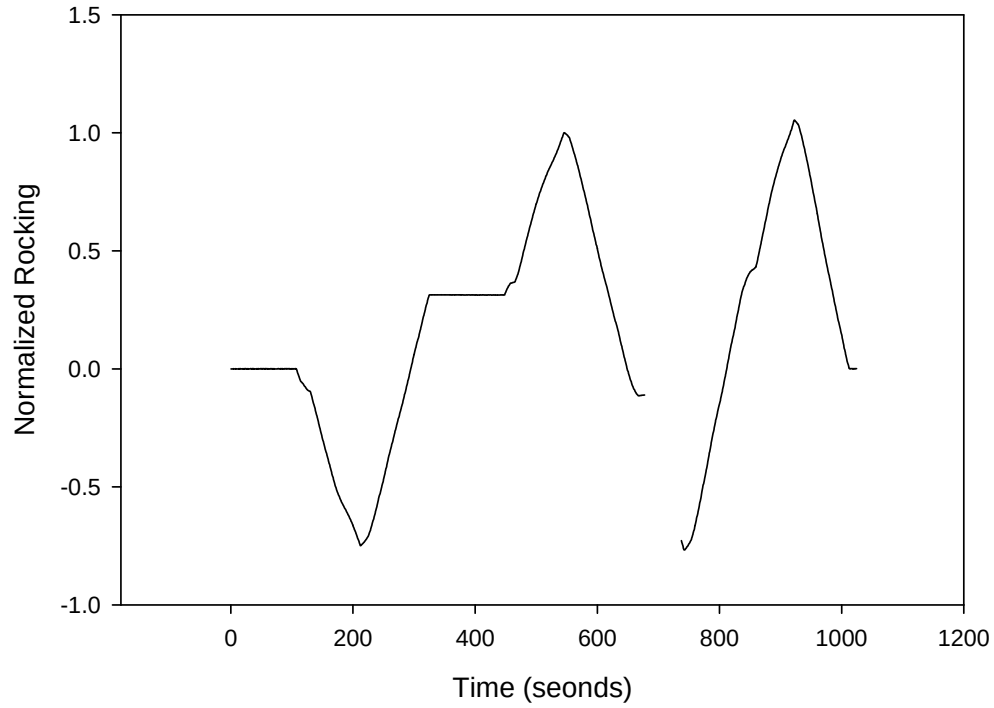

Figure A.36: Normalized rocking of pedestal in test P2-2

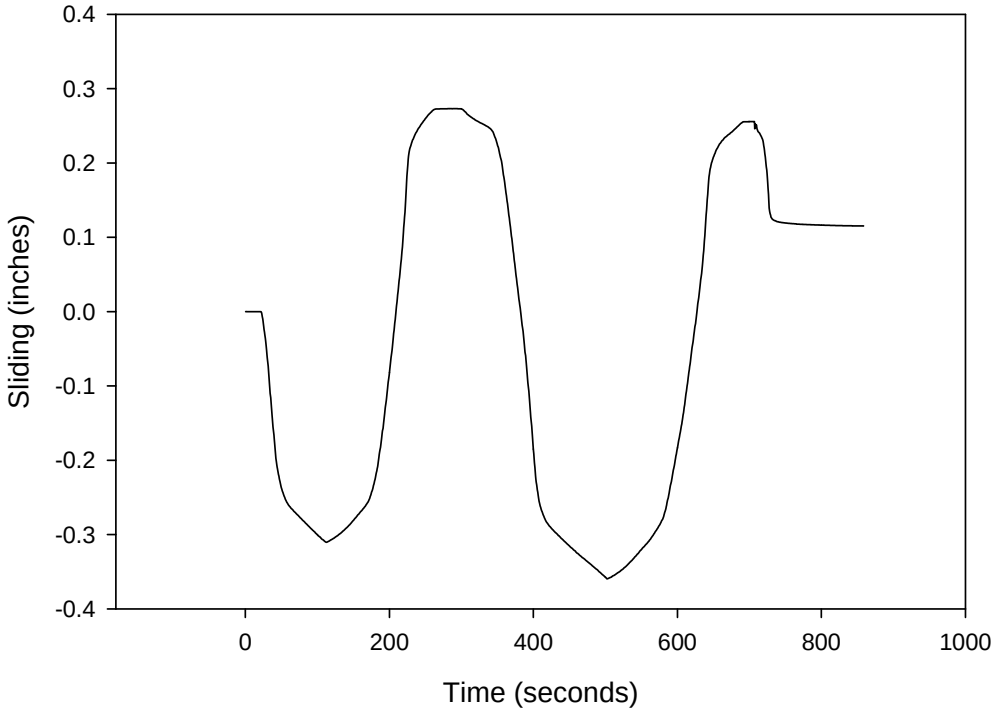

Figure A.37: Normalized relative movement (sliding) between the pedestal base plate and cap beam in test P3-1

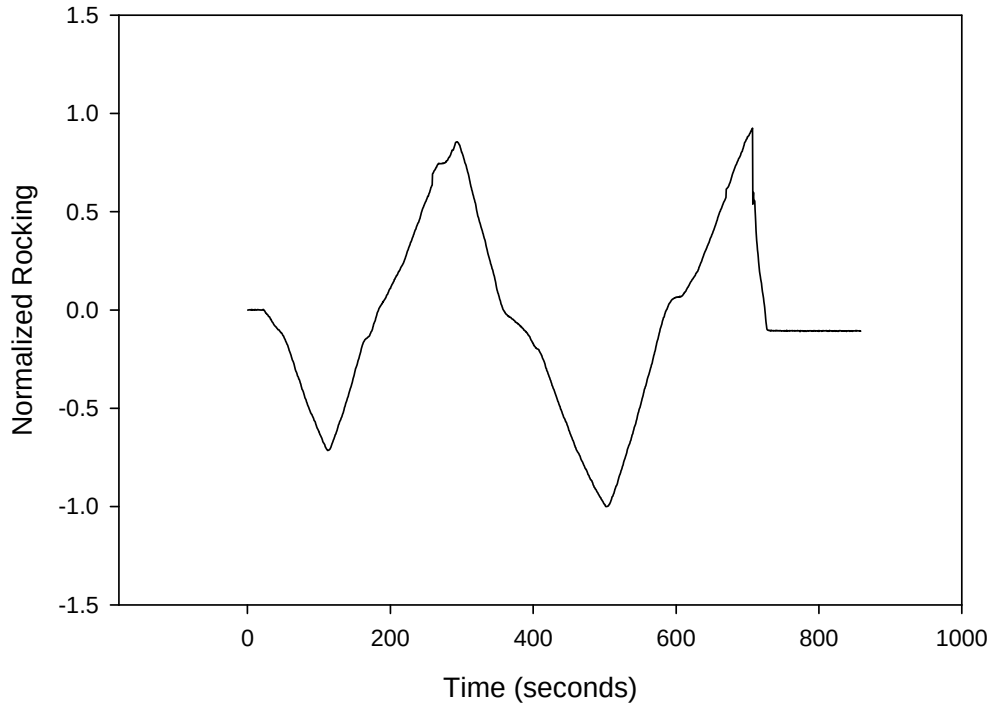

Figure A.38: Normalized rocking of pedestal in test P3-1

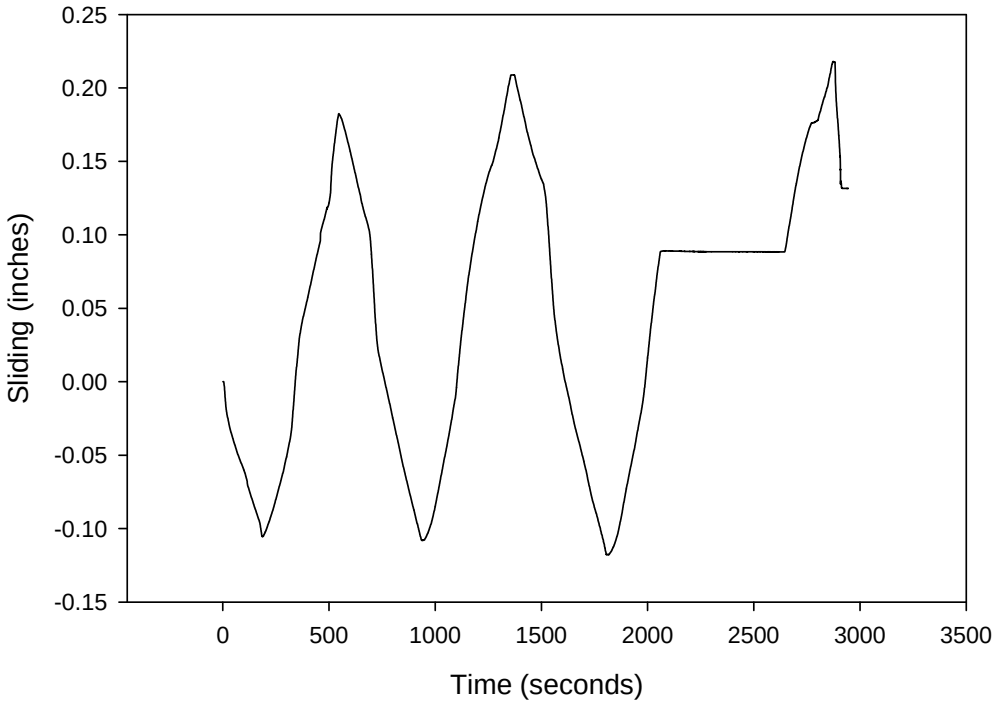

Figure A.39: Normalized relative movement (sliding) between the pedestal base plate and cap beam in test P3-2

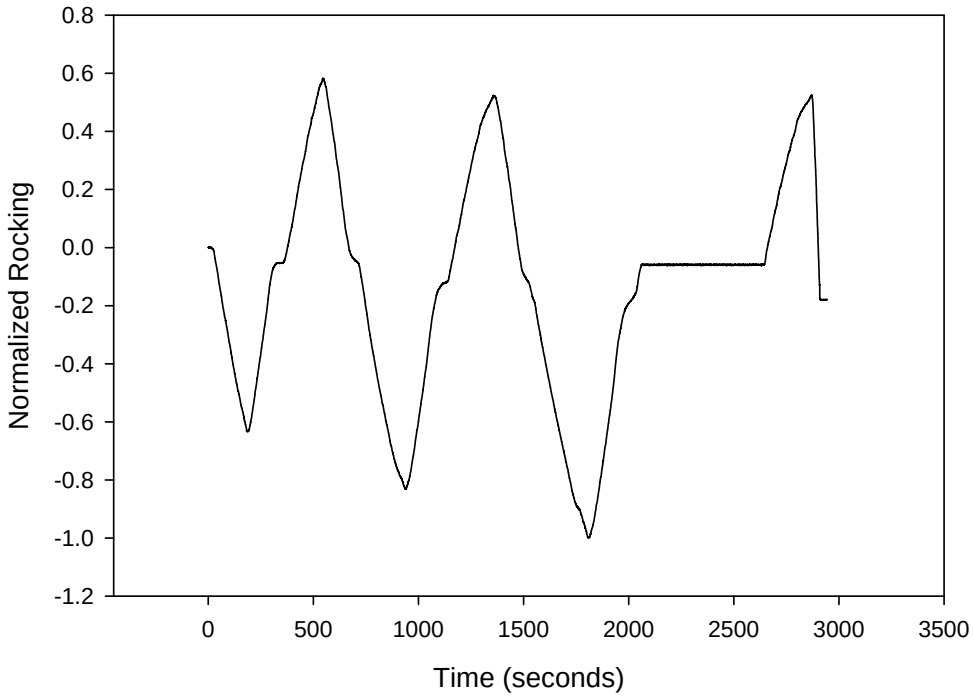

Figure A.40: Normalized rocking of pedestal in test P3-2

A.14 Steel Pedestal Component Tests

From the last set of data reviewed from the 33½" (tall) pedestals tests, the strain gauges on the pedestals captured responses that were of noteworthy attention to understanding the mechanical behavior of the pedestals. These issues will become important factors for the recommendations on best practices of steel pedestals stated in Chapter 6.

1. The strain gauges respond as a function of the applied load. Any eccentricity of the load due to construction tolerances (imperfections in specimen, alignment, etc.) and support conditions (load bearing on neoprene pad, perfect contact, performance of anchor bolts etc.) can greatly affect the response.

2. The 33½" (tall) pedestals performed as flexible components, therefore making the comparison to theoretical values of strain given both axial and lateral load a more complex analysis.

To better understand the load distribution of the pedestals as revealed by the strain gauges, data are collected for both the 19" (short) and 33½" (tall) pedestals to capture the response of the pedestals given axial (compression) load. The objectives of this set of testing are two-fold: (1) to serve as a "proof of concept" in that plane sections remain plane and (2) to show the structural behavior of the pedestals subjected to axial (compression) load. Testing was conducted on two different machines to verify results. Data are collected for cases with and without a plate on top of the pedestals to observe the distribution of the load on the cross-section. The pedestals are placed directly in the test machine without a neoprene pad underneath.

A.14.1 Setup for the 19" (short) pedestal component tests

The first set of tests was conducted on the 19" (short) pedestals using an Instron Satec machine having a capacity of 22 kips (Figures A.41 and A.42). This machine connected to a computer provided accurate loadings especially when the data was collected in between load steps.

Figures A.41: Instron Satec machine used for compression tests on 19" (short) pedestal

Figures A.42: Instron Satec machine used for compression tests on 19" (short) pedestal with computer (data logger)

The original strain gauges of the 19" pedestal were still in tact, and were connected to Wheatstone bridge circuits provided by a Measurements Group model SB10 Switch and Balance Unit. To supply the voltage to terminals of the bridge circuits and read the strain from the terminals, the SB10 is connected to a Measurements Group model P-3500 Strain Indicator (Figure A.43). The black knob on the left-hand side of the SB10 controls of the bridge circuits is switched to actually read the strain in each of the 10 terminals such that the strain is displayed on the box.

Figure A-43: SB10 and P-3500 strain indicator used to collect data from 10 strain gauges

A.14.2 Interpretation of data from the 19" (short) pedestal component tests

The loading history is shown in Figure A.44 where the steel pedestal was incrementally loaded at various loads where corresponding strains were captured. A maximum load of 15,990 lb was achieved.

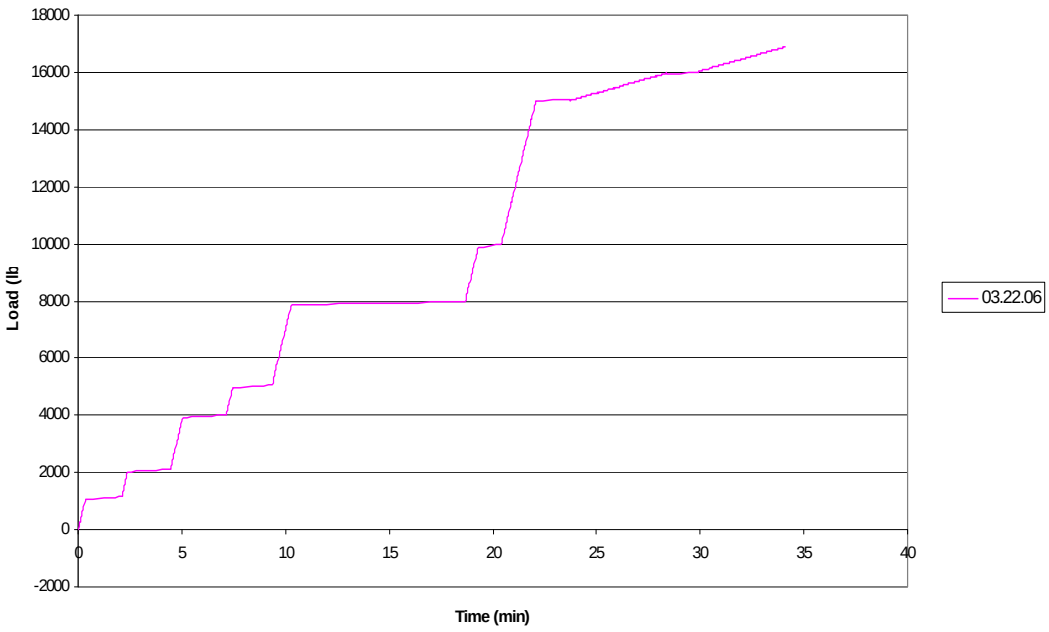

Figure A.44: Load history of Satec machine for the 19" (short) pedestal in compression

The results of the values read in the 10 strain gauges are shown in Figure A.45 in a plot of the calculated stress (psi) versus measured strain (in/in). The theoretical value for the given load is shown in the green line. Although the loading is concentric, the data show how much each strain gauge deviated from the theoretical value. This helps to understand the load distribution in the pedestal, where the strain gauges at the bottom better correlate to the theoretical values. The data also show that there were slight loading imperfections as the strain gauges in the web show larger strains as a result of bending that is also taking place. For the most part, the strain gauges appear to show a linear response such that we can assume that the pedestal is behaving elastically.

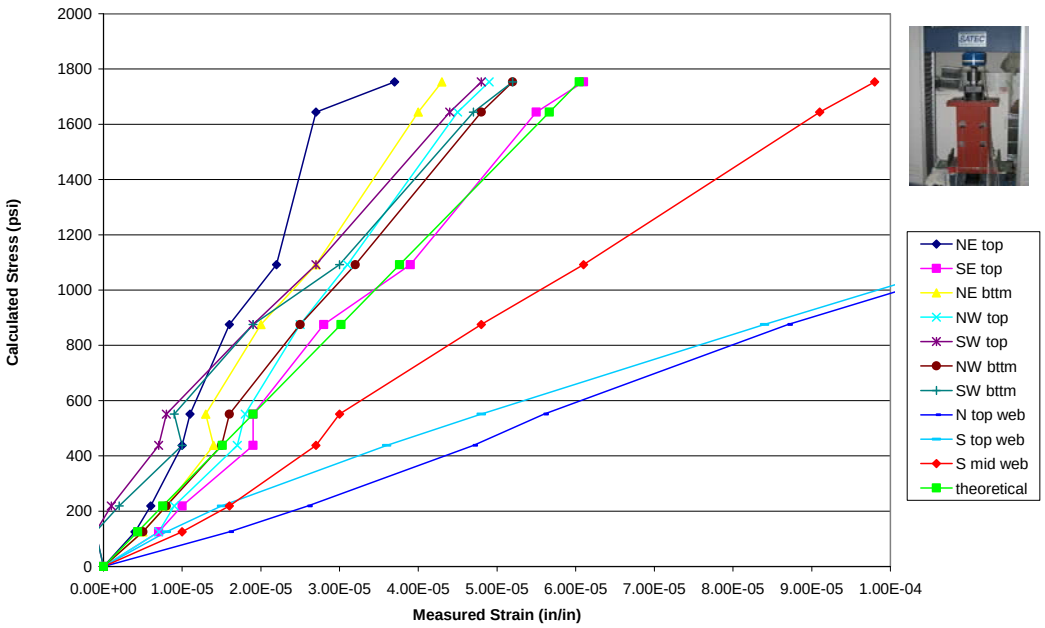

Figure A.45: Stress vs strain plot of compression test of 19" (short) pedestal

Due to the limitations of capacity with the Instron Satec machine, more tests were conducted using a Baldwin 400 kip capacity machine in the Structures Laboratory (Figures A.46 through A.48). So the setup was moved and data was collected with respect to loadings more representative for pedestals installed on a bridge. The stress versus strain plots are shown in Figures A-49 and A-50.

Figure A.46: Compression component test setup using a Baldwin 400 kip capacity machine and strain indicator box

Figure A.47: Compression component test setup using a Baldwin 400 kip capacity machine with spreader plate on top of steel pedestal

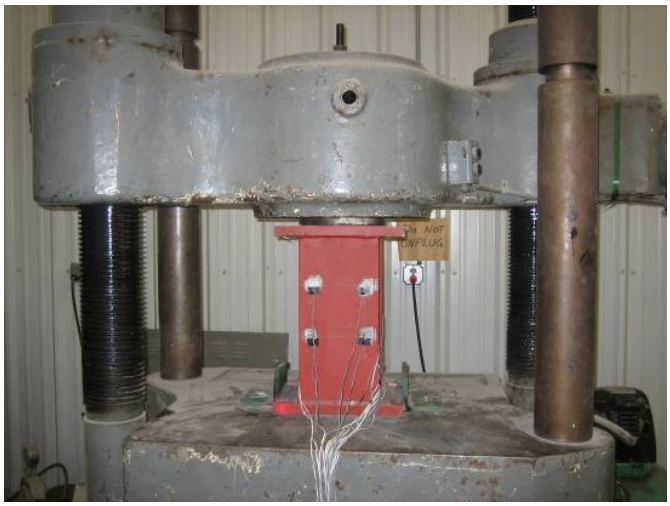

Figure A.48: Compression component test setup using a Baldwin 400 kip capacity machine without spreader plate on top of steel pedestal

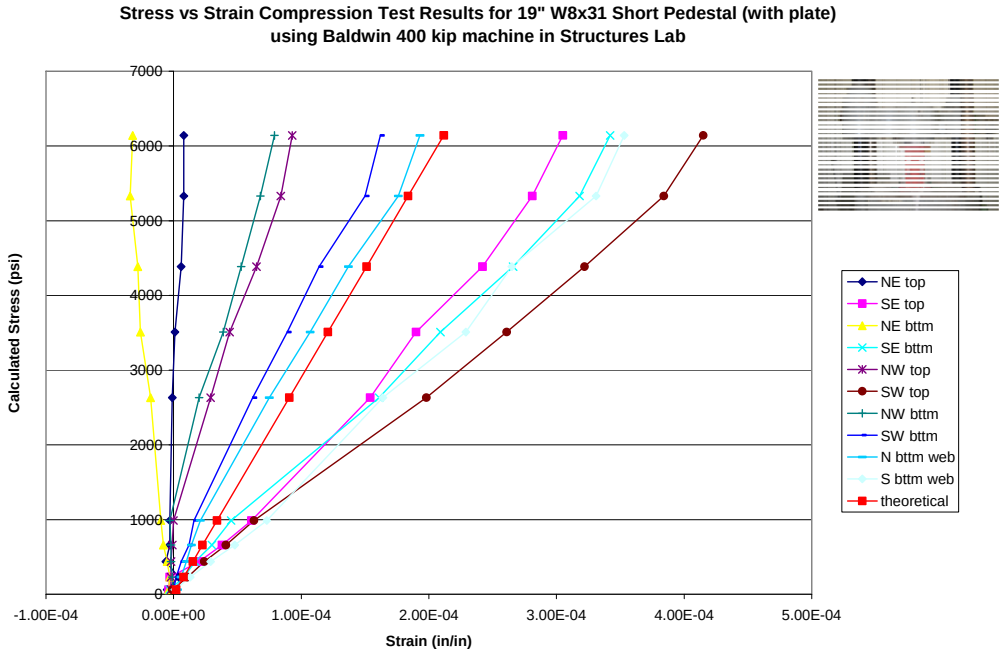

Figure A.49: Stress vs strain compression test results for 19" (short) pedestal with spreader plate

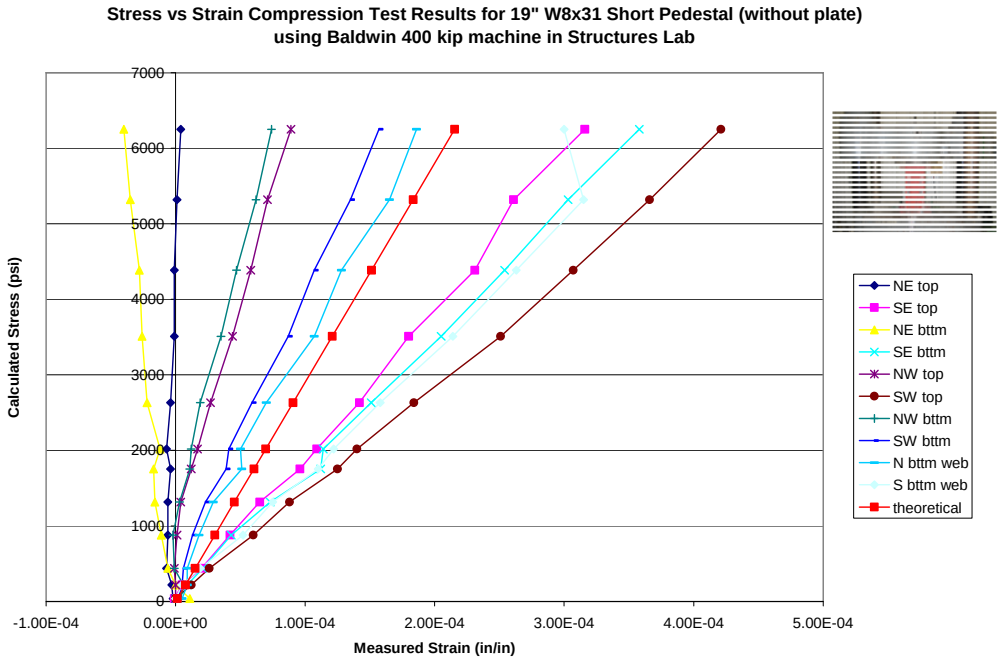

Figure A.50: Stress vs strain compression test results for 19" (short) pedestal without spreader plate

For the most part, the two sets of data show close correlation to one another. However, it is important to note the vast separation within the data. Although the slope of the lines is linearly increasing at a constant rate (taking into consideration experimental systematic error), the bottom strain gauges show closer approximation to the theoretical strains than the strain gauges located at the top portion of the pedestal. This data supports the observations regarding load distribution as noted by the last set of testing of the 33½" (tall) pedestals.

A.14.3 Setup for the 33½" (tall) pedestal component tests

The Baldwin 400 kip capacity test machine was also used to conduct compression tests on the 33½" (tall) pedestals. Some of the original strain gauges were replaced due to them ripping off in transition or during the lateral tests from Phase II. The same methodology and data retrieval process with the SB100 and P-3500 as in the 19" (short) pedestal component tests were applied. The 33½" (tall) pedestals were axially compressed to 57,000 lb (Figure A.51).

Figure A.51: 33½" (tall) pedestal in Baldwin 400-kip capacity machine for compression tests

A.14.4 Interpretation of data from the 33½" (tall) pedestal component tests

The data captured for the 33½" (tall) pedestal component tests are presented in Figure A.52. Given a longer distance to disperse the load due to the longer length of the 33½" (tall) pedestals, better correlation of the independent strain gauges on the flanges exists closer to the theoretical approximation. From the strain gauges in the web, the higher strains shown in one of the strain gauges appears to reveal additional strains as a result of bending of the upper portion of the pedestal. As seen in the 19" (short) pedestal tests, the bottom strain gauges do a much better job of matching the theoretical strain for a given load. Based on this information, a more in-depth review of the data from the 33½" (tall) pedestal tests will occur to determine how the centroid of the section is moving with respect to the loading given such flexible structural behavior exhibited by the 33½" (tall) pedestals. This will be done for both of data sets from the different types of bolt configurations in Phase II of testing.

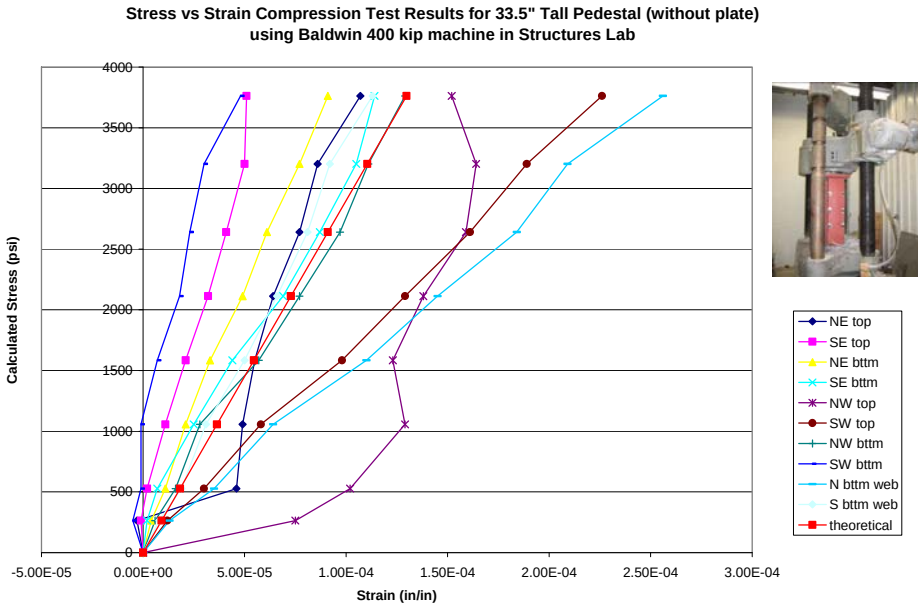

Figure A.52: Stress vs strain compression test results for 33½" (tall) pedestal without spreader plate

APPENDIX B

DEVELOPMENT OF SYNTHETIC GROUND MOTIONS FOR THE NONLINEAR TIME HISTORY ANALYSES (NTHA)

B.1 Soil Conditions for Three Locations used in this Study

The soil conditions for Cartersville, Georgia (Bartow County) and Fort Payne, Alabama (Dekalb County) are assumed to the be same; the soil conditions and profile for Allenhurst, Georgia (Liberty County) are uniquely defined based on soil type, shear wave velocity, plasticity index, and modulus reduction and damping curves. The deepest part of each layer profile is considered to behave linearly and has no dynamic properties associated with that layer. A total of three soil profiles and conditions are shown in Tables B.1 and B.2. The output from SHAKE91 is a suite of ground motions that are as input files to conduct time history analyses for the 3DOF bridge model.

Table B.1: Soil profile and conditions for Cartersville, Georgia (Bartow County) and Fort Payne, Alabama (Dekalb County) by Fernandez and Rix (2006)

Layer	Soil Layer Thickness (ft)	Soil Type	Shear Wave Velocity (ft/sec)	Plasticity Index
1	6.4	Poorly graded sands	1150	n/a
2	20.8	Silty sand	1658	n/a
3	1.1	Clayey Sands	1368	n/a
4	25.6	Inorganic clay with medium plasticity	1022	15
5	2.7	Inorganic silt with high plasticity	907	30
6	3.7	Inorganic clay with medium plasticity	2739	15
7	8.5	Inorganic silt with high plasticity	2520	30
8	3.7	Inorganic clay with medium plasticity	2098	15
9	3.2	Inorganic silt with high plasticity	2489	30
10	24.3	Inorganic silt with high plasticity	1560	30
11	109.4	Inorganic silt with high plasticity	1500	30
12	61.0	Inorganic silt with high plasticity	2161	30
13	2364	Inorganic silt with high plasticity	2517	30
14	Infinite	Site B Bedrock	11800	30

Table B.2: Soil profile and conditions for Allenhurst, Georgia (Liberty County) by Fernandez and Rix (2006)

Layer	Soil Layer Thickness (ft)	Soil Type	Shear Wave Velocity (ft/sec)	Plasticity Index
1	1.2	Inorganic clay with medium plasticity		15
2	5	Inorganic clay with medium plasticity	795	15
3	5	Inorganic clay with medium plasticity	795	15
4	Infinite	Clayey Limestone	2500	n/a

B.2 Plots of Time Histories used in this Study

The following time histories are used as input files for the synthetic ground motions used in the OpenSees analysis. The acceleration time histories shown below report the acceleration in units of in/s^2 and time in seconds.

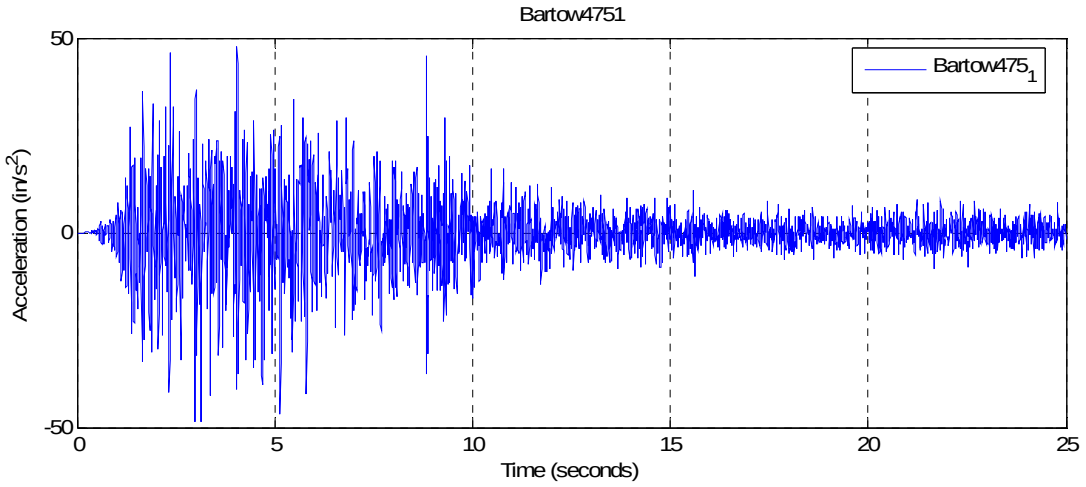

Figure B.1: Synthetic ground motion for Bartow475_1 (Cartersville, Georgia)

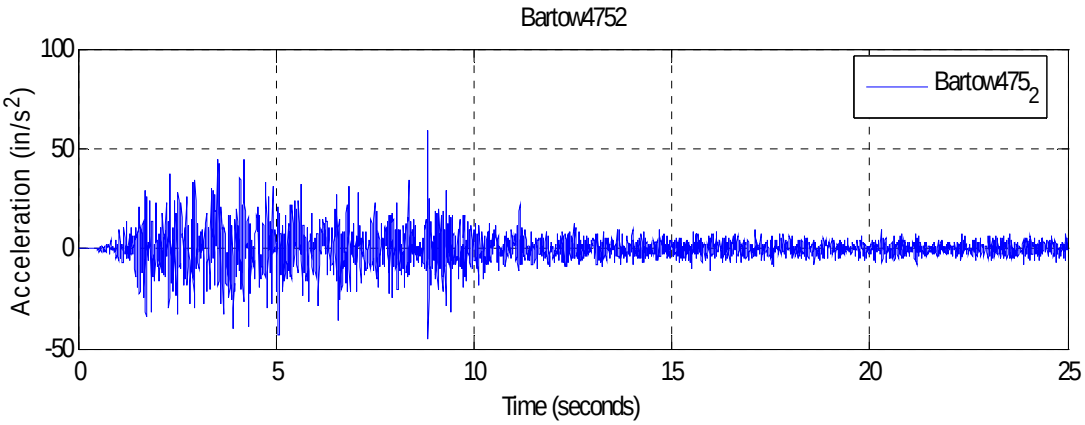

Figure B.2: Synthetic ground motion for Bartow475_2 (Cartersville, Georgia)

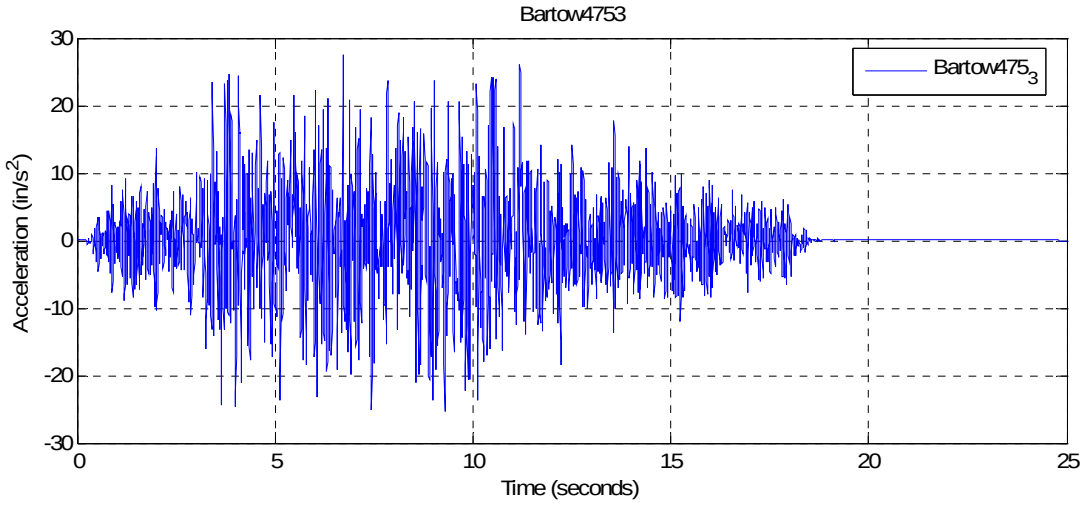

Figure B.3: Synthetic ground motion for Bartow475_3 (Cartersville, Georgia)

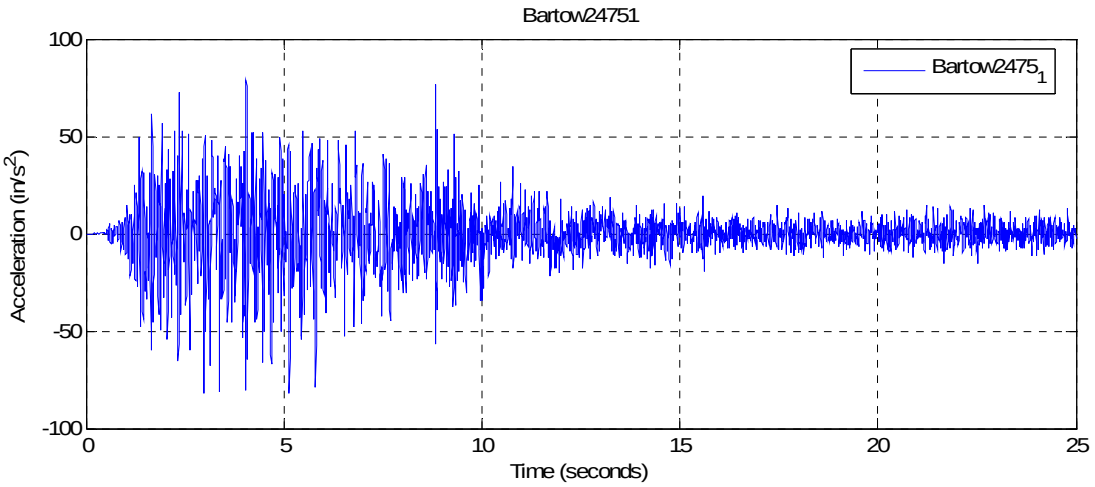

Figure B.4: Synthetic ground motion for Bartow2475_1 (Cartersville, Georgia)

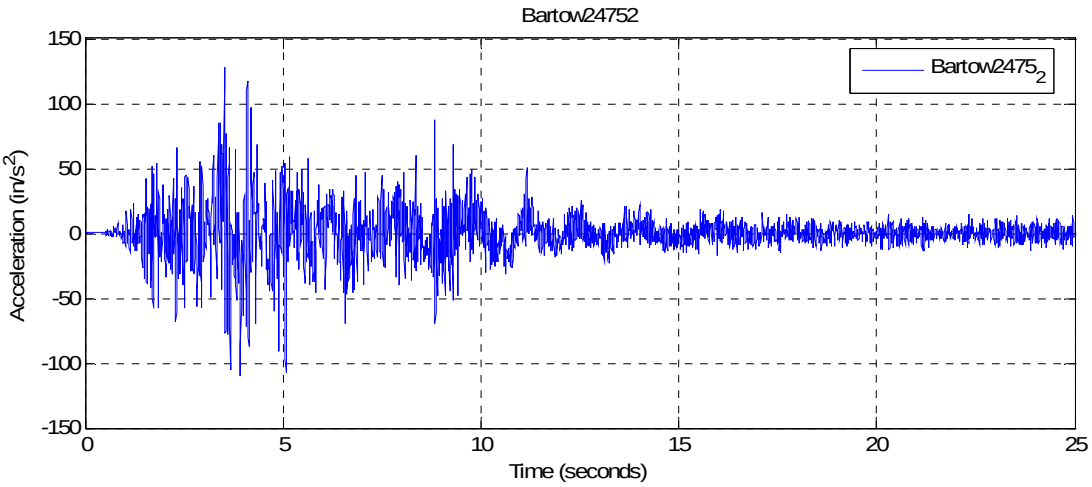

Figure B.5: Synthetic ground motion for Bartow2475_2 (Cartersville, Georgia)

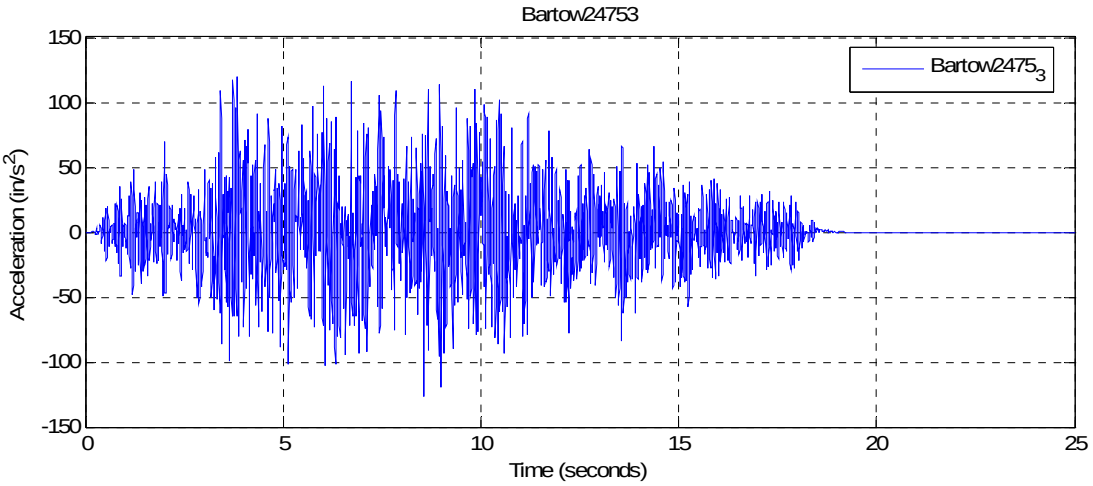

Figure B.6: Synthetic ground motion for Bartow2475_3 (Cartersville, Georgia)

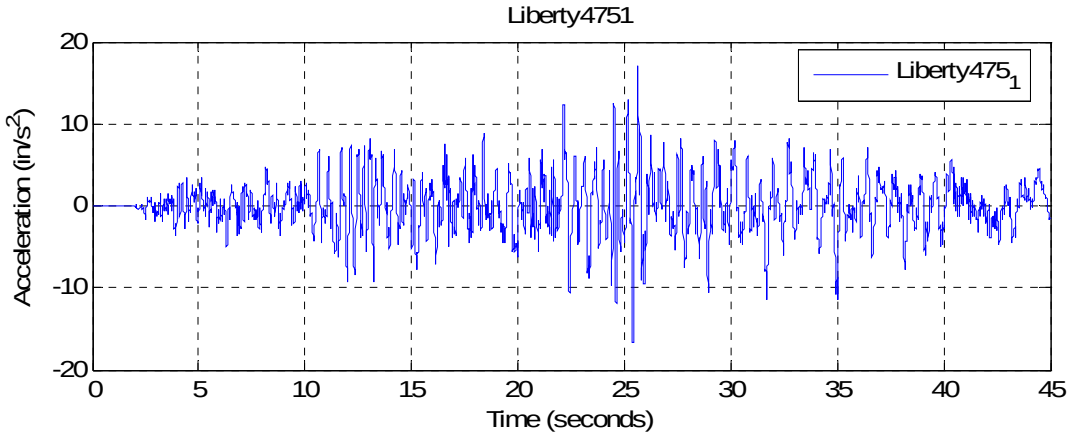

Figure B.7: Synthetic ground motion for Liberty475_1 (Allenhurst, Georgia)

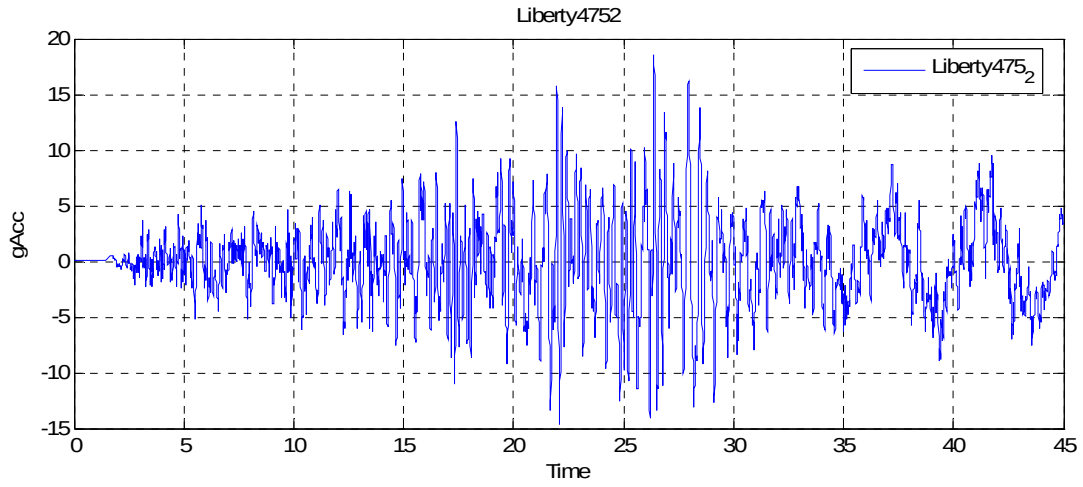

Figure B.8: Synthetic ground motion for Liberty475_2 (Allenhurst, Georgia)

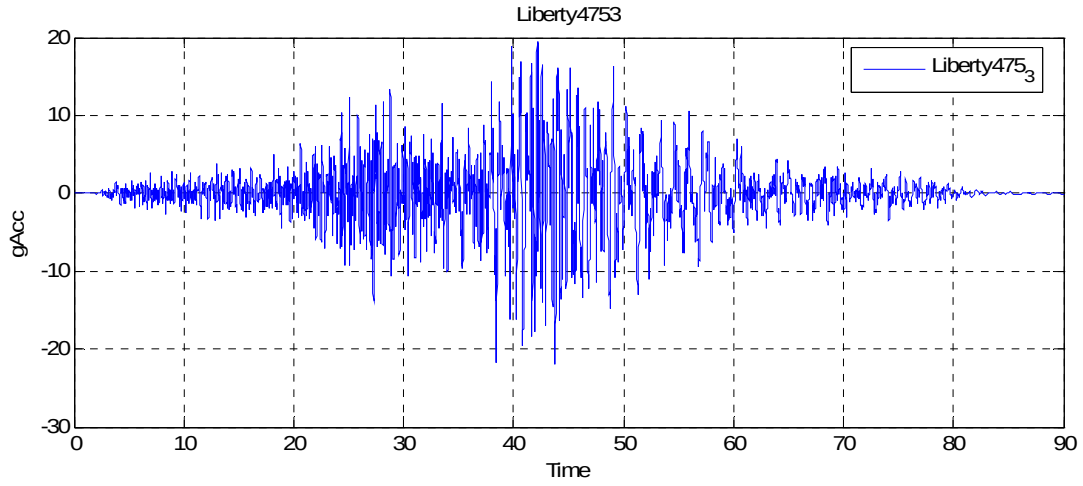

Figure B.9: Synthetic ground motion for Liberty475_3 (Allenhurst, Georgia)

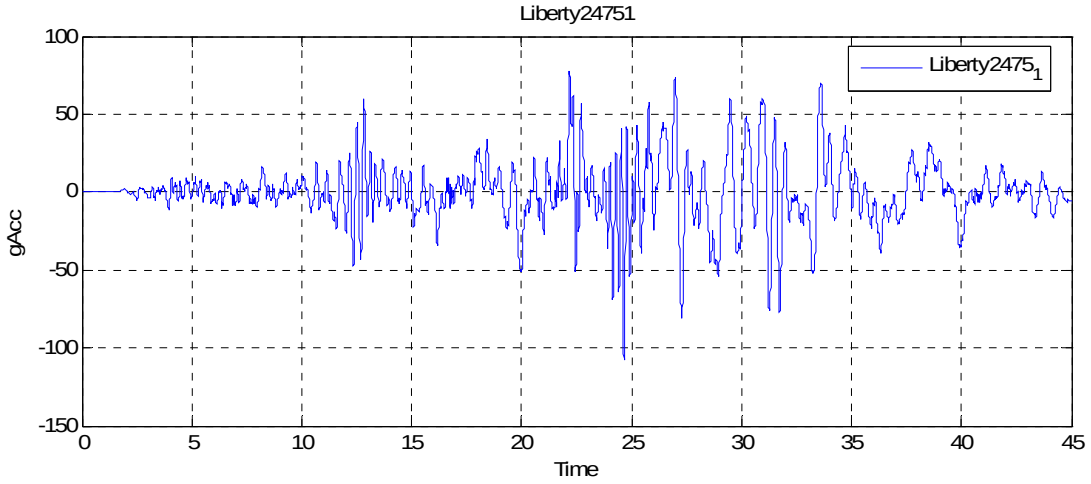

Figure B.10: Synthetic ground motion for Liberty2475_1 (Allenhurst, Georgia)

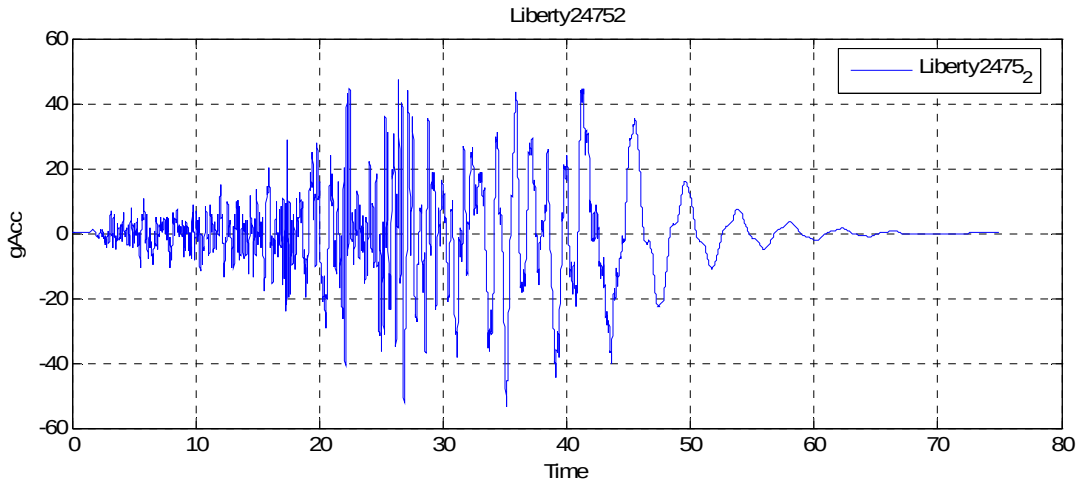

Figure B.11: Synthetic ground motion for Liberty2475_2 (Allenhurst, Georgia)

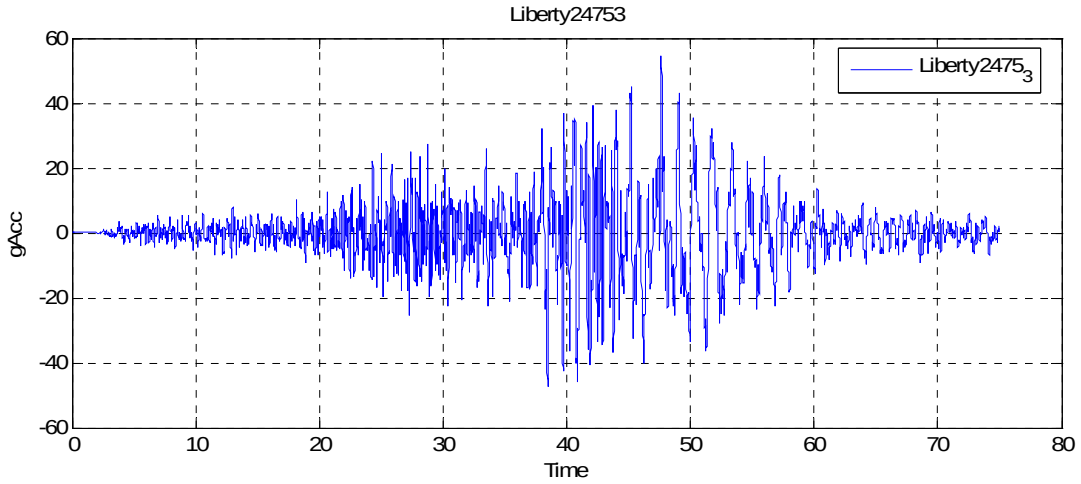

Figure B.12: Synthetic ground motion for Liberty2475_3 (Allenhurst, Georgia)

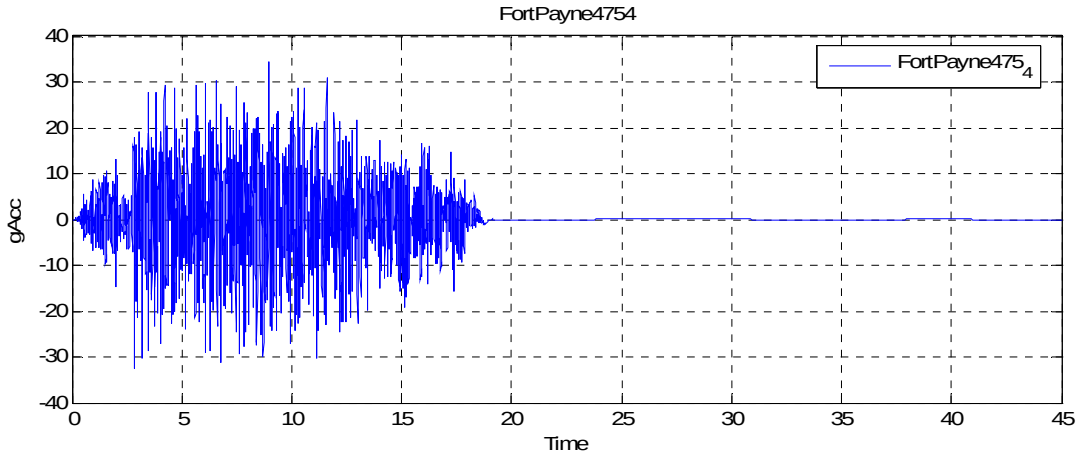

Figure B.13: Synthetic ground motion for FortPayne475_4 (Dekalb County, Alabama)

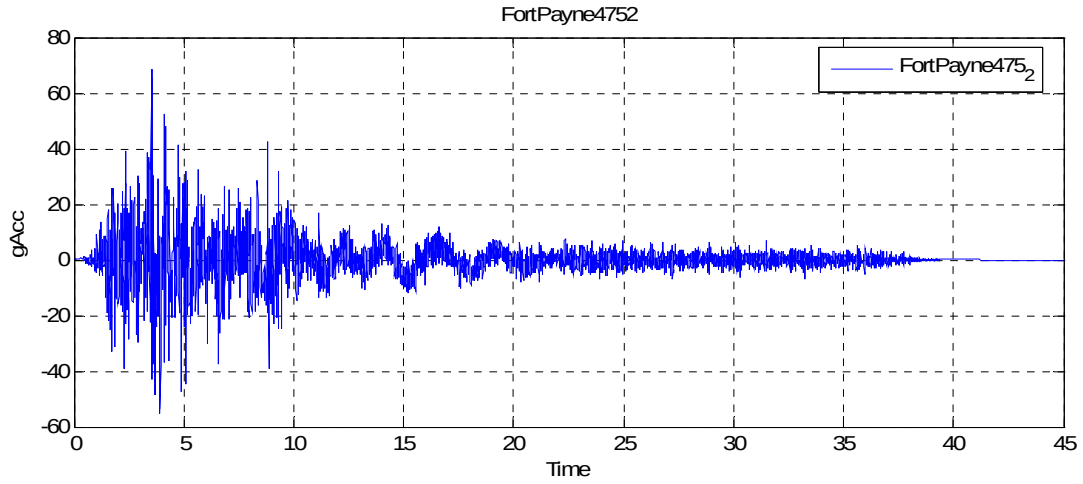

Figure B.14: Synthetic ground motion for FortPayne475_2 (Dekalb County, Alabama)

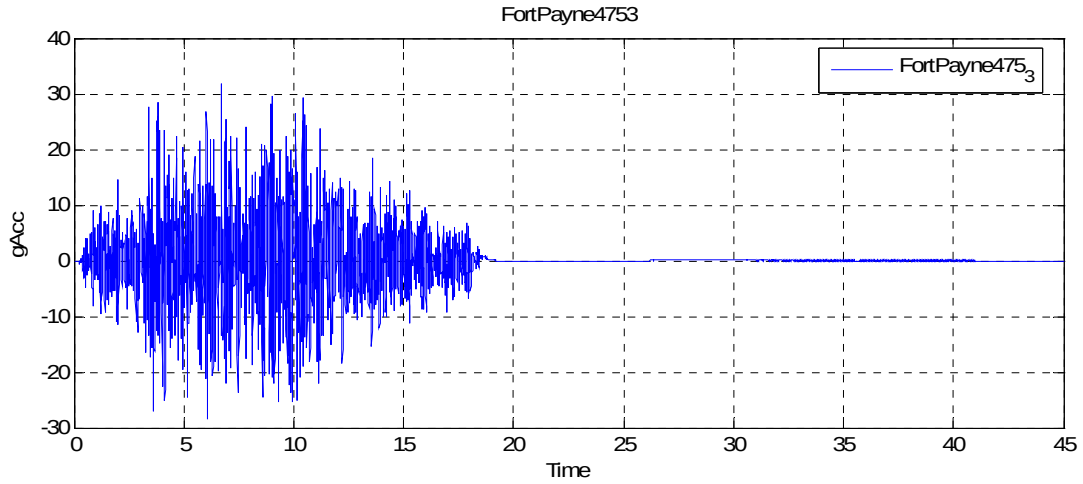

Figure B.15: Synthetic ground motion for FortPayne475_3 (Dekalb County, Alabama)

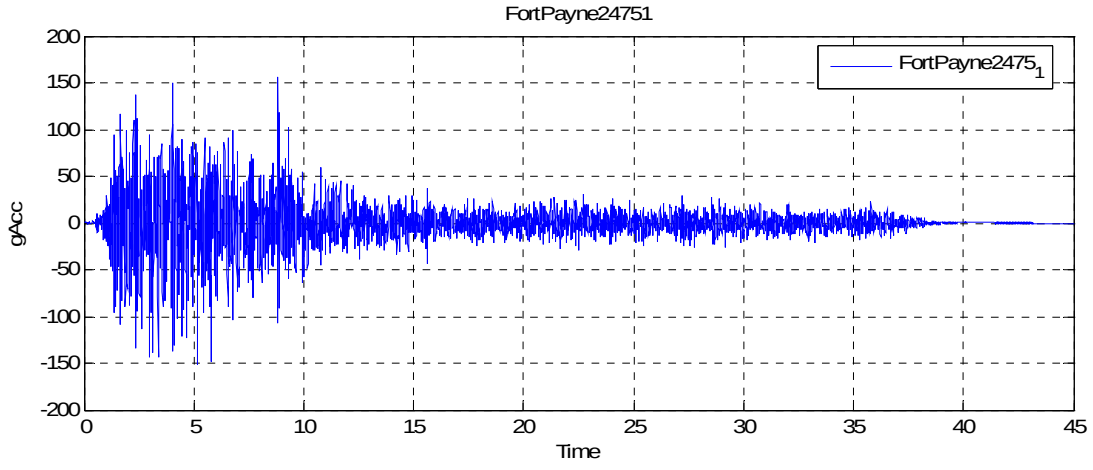

Figure B.16: Synthetic ground motion for FortPayne2475_1 (Dekalb County, Alabama)

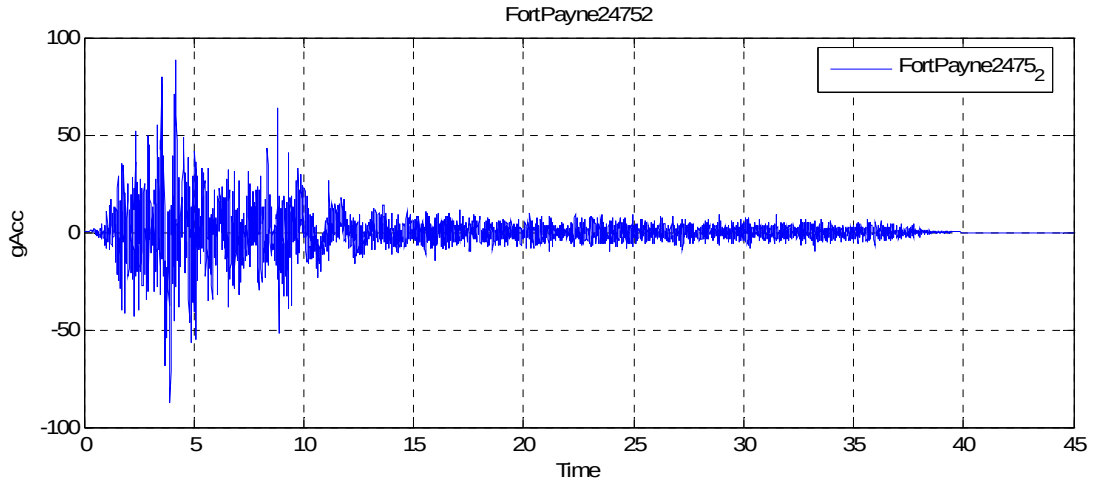

Figure B.17: Synthetic ground motion for FortPayne2475_2 (Dekalb County, Alabama)

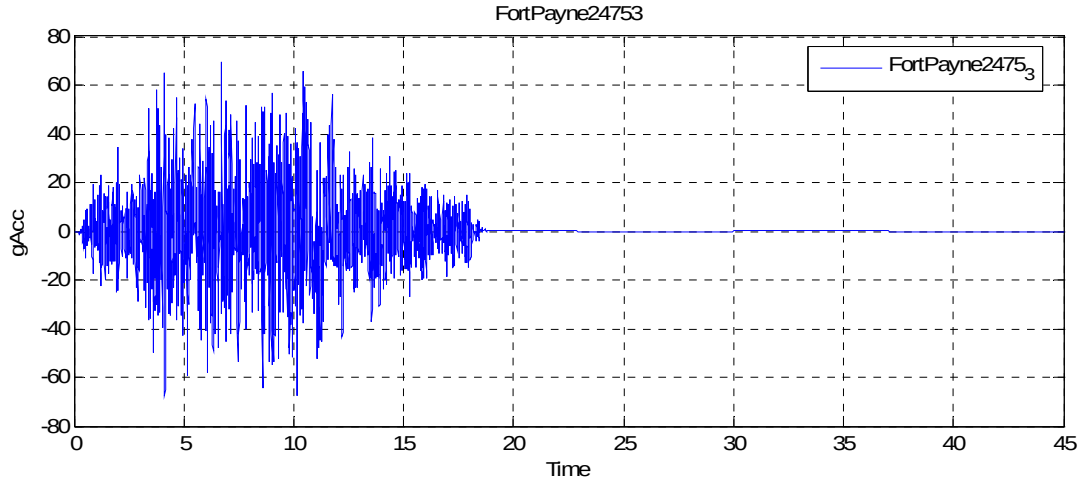

Figure B.18: Synthetic ground motion for FortPayne2475_3 (Dekalb County, Alabama)

REFERENCES

AASHTO LRFD (2004). American Association of State Highway and Transportation Officials (AASHTO) Bridge Design Specifications, Section 2: General Design and Location Features.

ACI Committee 318 (2005). Building Code Requirements for Structural Concrete (ACI 318-05) and Commentary (ACI 318R-05).

ACI Committee 355 (2004). Qualification of Post-Installed Mechanical Anchors in Concrete (ACI 322.2-04) and Commentary (ACI 3355.2R-04).

Atkinson, G. M., and Boore, D. M. (1995). "Ground Motion Relations for Eastern North America." *Bulletin of the Seismological Society of America*, 85(1), 17 - 30.

Berry, R., MDOT Special Projects Engineer, Bridge Division (2004). Increasing Bridge Vertical Clearance Heights. M. C. Hite. Mississippi.

Campbell, K. W. (2003). "Prediction of Strong Ground Motion Using the Hybrid Empirical Method and Its Use in the Development of Ground-Motion (Attenuation) Relations in Eastern North America." *Bulletin of the Seismological Society of America*, 93(3), 1012 - 1033.

Chopra, A. K. (2001). Dynamics of Structures. Upper Saddle River, NJ, Prentice-Hall.

Craddock, Bill (2006). "Atlanta Rod & Manufacturing Ping Tai Stainless Works Mill Test Analysis Certificate," Highway Materials, Georgia.

Decker, M. (2001). 299-day loss of interstate overpass proves disruptive, inconvenient for city. The Lebanon Daily Record. Lebanon.

DesRoches, R., R. T. Leon, et al. (2000). Response Evaluation and Modification of Typical Bridges in the Central and Southeastern United States. 12 WCEE 2000, Auckland, New Zealand.

DesRoches, R., T. Pfeifer, et al. (2003). "Full-scale tests of seismic cable restrainer retrofits for simply supported bridges." Journal of Bridge Engineering **8**(4): 191.

Dicleli, M. and M. Bruneau (1995). "An Energy Approach to Sliding of Single-span Simply Supported Slab-on-girder Steel Highway Bridges with Damaged Bearings." Earthquake Engineering and Structural Dynamics **24**: 395-409.

Dutta, A. (1999). On Energy Based Seismic Analysis and Design of Highway Bridges. Buffalo, State University of New York at Buffalo. **PhD**.

Eligehausen, R., R. Mallee, et al. (2006). Anchorage in Concrete Construction. Berlin, Ernst & Sohn.

El-Tawil, S., E. Severino, et al. (2005). "Vehicle collision with bridge piers." Journal of Bridge Engineering **10**(3): 345.

FHWA and MCEER (2006). Federal Highway Administration (FHWA) and MCEER Seismic Retrofitting Manual for Highway Structures: Part 1-Bridges.

Frankel, A., Mueller, C., Barnhard, T., Perkins, D., Leyendecker, E. V., Dickman, N., Hanson, S., and Hopper, M. (1996). "National Seismic Hazard Maps: Documentation." *OFR 96-532*, U.S. Geological Survey.

Frankel, A., Petersen, M., Mueller, C., Haller, K., Wheeler, R., Leyendecker, E. V., Wesson, R., Harmsen, S., Cramer, C., Perkins, D., and Rukstales, K. (2002). "Documentation for the 2002 Update of the National Seismic Hazard Maps." *OFR 02-420*, U.S. Geological Survey.

Frankel, A.D. and E.V. Leyendecker (2006).*Seismic Hazard Curves and Uniform Hazard Response Spectra*, Probabilistic Hazard 3.10 CD.

Fu, C. C., J. R. Burhouse, et al. (2004). "Overheight vehicle collisions with highway bridges." Transportation Research Record(1865): 80.

Fung, G. G., R. J. Lebeau, et al. (1971). Field investigation of bridge damage in the San Fernando earthquake. C. D. o. Transportation. Sacramento, California.

Georgia Department of Transportation, GDOT (2004). "Bridge Design Guide." from http://tomcat2.dot.state.ga.us/thesource/index.html.

Hanchey, C. M. and S. F. Exley (1990). "Overheight Vehicle Warning Systems in Mississippi." Institute of Transportation Engineers (ITE) **60**(6): 24-29.

Hartnagel, B. A. (2004). Structural Special Assignments Engineer. P. D. Reginald DesRoches**:** Missouri Department of Transportation.

Housner, G. W. (1971). General features of the San Fernando earthquake. P. C. Jennings. Pasadena, California, Earthquake Engineering Research Laboratory, California Institute of Technology.

Illinois Department of Transportation. "Structural Services Manual, Bearing Height Adjustment." from http://www.dot.il.gov/bridges/brdocuments.html.

Kim, S.-H., H.-S. Mha, et al. (2006). "Effects of bearing damage upon seismic behaviors of a multi-span girder bridge." Engineering Structures **28**(7): 1071.

Lam, T. T. (2000). Performance of Steel Laminated Elastomeric Bearings of a Full-Scale Bridge Subjected to Dynamic Loading. Civil Engineering. Atlanta, Georgia Institute of Technology. **Master of Science:** 131.

Mander, J. B., D.-K. Kim, et al. (1996). Response of Steel Bridge Bearings to Reversed Cyclic Loading. Buffalo, State University of New York at Buffalo.

Mang, F. and O. Bucak (1993). Damage to old bridge structures caused by collision by vehicles, Guildford, UK, Publ by Thomas Telford Services Ltd, London, Engl.

Mayes, R. L., I. G. Buckle, et al. (1990). "AASHTO Seismic Isolation Design Requirements for Highway Bridges." Journal of Structural Engineering **118**(No. 1): 284-303.

Mazroi, A., L. R.-l. Wang, et al. (1983). "Effective Coefficient of Friction of Steel Bridge Bearings." Transportation Research Record(903): 79.

McGuire, R. K., Silva, W. J., and Costantino, C. J. (2001). "Technical Basis for Revision of Regulatory Guidance on Design Ground Motions: Hazard- and Risk-Consistent Ground Motion Spectra Guidelines." *NUREG/CR-6728*, U.S. Nuclear Regulatory Commission, Washington, DC.

McIntyre, T. (1937). "Raising of Jhelum bridge." Punjab Engineering Congress -- Proceedings **25**: 41.

Mitchell, D., R. Sexsmith, et al. (1994). "Seismic retrofitting techniques for bridges - a state-of-the-art report." Canadian Journal of Civil Engineering **21**(5): 823.

Myers, Charlie (2005). Bellamy Brothers (Georgia), steel pedestal contractor for GDOT.

NCHRP Project 12-49 (2001). "Comprehensive Specification for the Seismic Design of Bridges," MCEER.

Nielson, B. G. (2005). Analytical Fragility Curves for Highway Bridges in Moderate Seismic Zones. School of Civil and Environmental Engineering. Atlanta, Georgia Institute of Technology. **Doctor of Philosophy**.

Pfeifer, T. (2002). Experimental tests of seismic retrofit components on a full-scale model of a typical steel bridge in Mid-America. School of Civil and Environmental Engineering. Atlanta, Georgia Institute of Technology. **Master of Science in Civil Engineering**.

Priestley, M. J. N. and F. Seible (1995). "Design of seismic retrofit measures for concrete and masonry structures." Construction and Building Materials **9**(6): 365.

Qiao, P., M. Yang, et al. (2004). "Impact analysis of I-Lam sandwich system for over-height collision protection of highway bridges." Engineering Structures **26**(7): 1003.

Rashidi, S. and M. Ala Saadeghvaziri (1997). "Seismic modeling of multi-span simply-supported bridges using ADINA." Computers and Structures **64**(5-6): 1025.

Roberts, J. E. (1990). Recent advances in seismic design and retrofit of bridges. Fourth U.S. National Conference on Earthquake Engineering, El Cerrito, California, Earthquake Engineering Research Institute.

Somerville, P., and Saikia, C. (2001). "Ground Motion Attenuation Relations for the Central and Eastern United States." *Report to the U.S. Geological Survey under award number 99HQGR0098*, URS Group, Inc.

Snyder, G., P.E., INDOT Bridge Rehabilitation Engineer Supervisor (2005). Increasing Bridge Clearance Heights. M. C. Hite. Indiana.

Toro, G. R., Abrahamson, N. A., and Schneider, J. F. (1997). "Model of Strong Ground Motions from Earthquakes in Central and Eastern North America: Best Estimates and Uncertainties." *Seismological Research Letters*, 68(1), 41 - 57.

UMKC (2002). "Seismic Hazard/Seismic Risk Analysis MBDSI," from http://www.cstp.umkc.edu, University of Missouri Kansas City.

USGS (2002). "National Seismic Hazard Maps," from http://earthquake.usgs.gov/research/hazmaps/products_data/index.php.

Yashinsky, M. (1991). Seismic retrofit of bridge foundations, Los Angeles, CA, USA, Publ by ASCE, New York, NY, USA.

Ye, A. J., S. D. Hu, et al. (2001). "Simulation of seismic behavior for bridge bearings." Tongji Daxue Xuebao/Journal of Tongji University **29**(1): 6.

VITA

MONIQUE C. HITE

Monique C. Hite was born in Newark, Delaware. She attended public schools in Newark, Delaware, received a B.S. and M.S. in Civil Engineering from the University of Delaware in 2000 and 2002, respectively. In the fall of 2002, she matriculated to the Georgia Institute of Technology to pursue a doctorate in Civil (Structural) Engineering. While at the Georgia Institute of Technology, her major concentration of study was structural and earthquake engineering with a minor in seismology. She was the recipient of several fellowships including the Office of Naval Research (ONR) Doctoral Fellowship, Georgia Tech's Facilitating Academic Careers in Engineering and Science (FACES) Fellowship sponsored by the National Science Foundation (NSF), and the GEM Fellowship. She interned during the summers of 2003 and 2005, respectively, with the National Academies Christine Mirzayan Science and Technology Policy Internship Program and the Naval Research Laboratory (NRL), both in Washington, D.C. She began a tenure-track faculty position in the Department of Civil Engineering at Texas A&M University in College Station, Texas in August 2007. When she is not conducting her research, she enjoys dancing, reading, playing tennis, and spending quality time with loved ones.